POLITECNICO DI MILANO

School of Industrial and Information Engineering

Master Degree in Mechanical Engineering

Experimental Assessment of an Actuator Line Simulation Tool for Vertical Axis Wind Turbines

Supervisor: Prof. Giacomo PERSICO

Co-Supervisor: Ing. Paolo SCHITO

Master Thesis of:

Pier Francesco MELANI
ID 852549

Academic Year 2017 - 2018

Pier Francesco Melani: *Experimental Assessment of an Actuator Line Simulation Tool for Vertical Axis Wind Turbines* | Master Thesis in Mechanical Engineering, Politecnico di Milano.

Politecnico di Milano:
www.polimi.it

School of Industrial and Information Engineering:
www.ingindinf.polimi.it

Ringraziamenti

Questa breve sezione è dedicata a tutte le persone che, in un modo o nell'altro, hanno contribuito in maniera determinante allo svolgimento di questo lavoro.

Innanzitutto vorrei ringraziare il Professor Giacomo Persico, non solo per avermi dato la possibilità di lavorare ad un progetto così interessante ed innovativo, ma anche per la grande premura con cui mi ha seguito durante l'intero corso del suo svolgimento. La mia gratitudine nei suoi confronti tuttavia non è limitata all'ambito di questo lavoro. É stato infatti il Prof. Persico, con la sua passione e competenza, a trasmettermi in questi anni quell'entusiasmo per la ricerca e la speculazione scientifica che io oggi considero inestimabile, e che mi ha portato alla scelta di indirizzare la mia carriera verso l'ambito accademico.

Vorrei inoltre ringraziare l'Ing. Paolo Schito, sia per la grande disponibilità e cortesia con cui mi ha seguito in questi mesi di lavoro, sia per avermi messo a disposizione le risorse computazionali necessarie per le simulazioni ed il codice utilizzato per questa tesi; in tale frangente, un ringraziamento particolare va all'Ing. Luca Bernini, il cui supporto è stato fondamentale per l'implementazione del modello di stallo dinamico nel solutore.

Un ringraziamento speciale va infine alla mia famiglia, che con grande dedizione e sacrificio mi ha sostenuto, economicamente e non, nel mio processo di formazione, lasciandomi libero di seguire le mie naturali inclinazioni. Per questo dono, sarò loro eternamente grato.

Milano, Luglio 2018 P.F. M.

Abstract

The thesis presents the detailed experimental assessment of a computational model for the resolution of the flow around Vertical Axis Wind Turbine (VAWT) rotors. This technique, which treats the blade aerodynamics using an actuator line (ACL) representation, allows to limit the computational cost normally associated to three-dimensional calculations, thus providing the ideal framework for simulating wind turbines immersed into the atmospheric boundary layer or operating in the urban environment. The highly unsteady and fully three-dimensional character of VAWT aerodynamics complicates however the model implementation and makes it prone to reliability issues; for this reason, experimental validation is decisive for evaluating the fidelity of the simulation tool, and for investigating the impact of the various corrective sub-models implemented. In the present work, such procedure is carried out by comparing the ACL prediction with the data coming from extensive wind tunnel testing of a real-scale model of a H-shaped VAWT for microgeneration, for which both performance and detailed wake measurements are available. The comparison is made for different tip-speed ratio conditions and combinations of sub-models in the ACL tool. Results show that the turbine performance and the main features of the rotor aerodynamics are well reproduced by the model, resulting in a very good prediction of the wake profile in the equatorial section of the turbine. The quantitative agreement between experiments and calculations locally drops close to the blade tip, where the flow field is fully dominated by 3D effects, even though the model is still able to reproduce qualitatively the most relevant wake features.

Keywords: VAWT, ACL-CFD, wake

Estratto

Il presente lavoro di tesi si occupa della validazione sperimentale di un modello numerico per l'analisi di turbine eoliche ad asse verticale (VAWT). Questo metodo è in grado, grazie ad una modellazione actuator line (ACL) delle pale rotoriche, di ridurre notevolmente il costo computazionale normalmente associato alla simulazione di queste macchine, aprendo così la strada allo sviluppo di modelli avanzati della loro interazione con ambienti complessi come quello urbano. A causa della marcata instazionarietà e tridimensionalità del campo di moto rotorico tuttavia, l'implementazione di tale tecnica è tutt'altro che banale e richiede un'adeguata validazione dal punto di vista sperimentale, volta non solo ad appurarne l'affidabilità, ma anche a valutarne la sensibilità rispetto ai vari sottomodelli utilizzati. A tal scopo, i risultati ottenuti con il metodo ACL sono stati confrontati con le misure effettuate in galleria del vento su un modello in scala reale di un rotore Darrieus ad H per microgenerazione, considerando diverse condizioni operative e combinazioni dei sottomodelli disponibili nel solutore ACL. Dai vari confronti è emersa una spiccata capacità del modello di prevedere in maniera accurata non solo le prestazioni della turbina, ma anche lo sviluppo spaziale e temporale della scia, soprattutto nella zona equatoriale della macchina. La corrispondenza quantitativa tra dati numerici e sperimentali diminuisce notevolmente avvicinandosi alla regione d'estremità delle pale, dove il campo di moto è completamente tridimensionale, nonostante il modello sia ancora in grado di riprodurre qualitativamente le principali caratteristiche della scia.

Parole chiave: VAWT, ACL-CFD, scia

Contents

List of Figures

List of Tables

Summary

In the urban environment, where highly complex flows result from the interaction between the buildings and the atmospheric boundary layer, vertical axis wind turbines (VAWTs) can be competitive with the more conventional horizontal axis technology, thanks not only to their insensitivity to yaw, but also to their reduced acoustic pollution, caused by the lower optimal tip-speed ratio (TSR). Among the several concepts proposed for VAWTs, the lift-driven Darrieus turbine is probably the most promising, as it might provide performance comparable to the ones of horizontal rotors.

To exploit properly the wind resource in such a complicated environment however, the installation of the rotors demands a dedicated optimization, which in turn requires advanced models, able to capture the interaction between the atmospheric boundary layer, the buildings, and the turbine. The ideal simulation tool for such complex configuration, or at least the unique that leads to a reasonable computational cost, is the so-called actuator line CFD model, proposed in [51] for VAWTs and further developed by [50].

The Actuator Line Method (ACL) combines a BEM-based modelling of the turbine with the Finite Volume (FV) discretisation of the flow domain; in particular, each blade is replaced by a dynamically equivalent actuator line, introducing aerodynamic forces into the computational grid basing on its current position and the instantaneous local flow conditions. This strategy allows to reduce the implementation effort and elaboration time associated to a fully resolved CFD simulation; being based on blade-element theory, it does not require in fact the resolution of the boundary layer encompassing the blade surfaces, with a corresponding strong decrease in the required computational resources [51]. Its main drawback, inherited from BEM, is the elevated sensitivity to input aerodynamic data and employed sub-models, which thus demand extreme care in their derivation and implementation.

Due to the significant modelling effort required by the method, its reliability must be assessed via proper experimental validation. For the purpose, a wide simulation campaign was carried out, basing on the research code *DarrieusSolver*; this tool, developed by the Department of Mechanical Engineering of Politecnico di Milano [7, 14, 49, 50], integrates the ACL method into the incompressible transient solver *pisoFoam*, available in the open-source framework OpenFOAM and based on the PISO solution scheme [26]. The results, in terms of turbine performance and wake representation, were compared with the data coming from extensive wind tunnel testing of a real-scale model of a H-shaped VAWT for microgeneration [17]. The comparison was performed for different operating conditions and combinations

of the sub-models available in the solver:

- *Flow curvature correction*: the alteration of exchanged aerodynamic forces due to the finite curvature of streamlines interacting with the turbine blade is modelled via the method proposed in [44]. Such effect is expressed as proper virtual camber and pitch angle to be added to the original profile and evaluated via conformal mapping technique.
- *Dynamic stall model*: the impact of dynamic stall on the aerodynamic forces is embedded in the solver via the run-time correction of tabulated lift and drag coefficients, basing on the model proposed in [6, 37].
- *Tip loss correction*: losses associated to tip aerodynamics are quantified according to Glauert theory (in the formulation proposed in [22]), which corrects the locally exchanged force depending on its position along the blade span.

This way, a better understanding of their qualitative and quantitative relevance could be achieved.

Thesis Outline

The thesis is structured as follows:

- *Chapter 1* provides a brief introduction to microgeneration and to the challenges it poses to the design and optimisation of wind turbines, especially in the urban environment. In this frame, the state of the art in terms of available machine architectures and methods of analysis is presented.
- *Chapter 2* reports a detailed description of the turbine under study and of the corresponding experimental investigation in the wind tunnel of Politecnico di Milano, with particular emphasis on the adopted measurement and post-processing techniques.
- In *Chapter 3* the ACL model of the turbine used for the simulation campaign is presented. The first part of the chapter provides a full documentation of the *DarrieusSolver* operation, the derivation of the input polar data and the implementation of applied sub-models (flow curvature, dynamic stall, tip loss). The second part focuses instead on the numerical set-up of the simulations, including the modelling of turbulence, the discretisation of the flow domain, the applied boundary conditions and differentiation schemes.
- *Chapter 4* provides a comparison between the results of the simulation campaign and the available experimental data, in terms of predicted turbine performance and wake representation.

Chapter 1

Introduction

1.1 Wind energy and microgeneration

1.1.1 Centralised vs distributed generation

From the second half of the XXI century, the worldwide scenario has been dominated by a *centralised* approach to energy production. Electricity is generated in a few large facilities, mostly exploiting steam or gas technology and powered by fossil (oil, gas, coal) or nuclear fuel; it is then supplied to the end user via a dedicated transmission network, which has also the task to convert it to the required voltage level.

So far, the success and diffusion of this approach have been related to the advantages offered by concentrated sources of energy such as fuels; their ease of transport and storage, combined to the elevated energy density, have favoured the construction of larger and larger power plants, capable to overcome their high investment costs, thanks to their enhanced efficiency and the economy of scale, and provide electricity to the end user in a reliable and constant way. The latter feature was also made possible by the adoption of an AC, high-voltage transmission network, which allowed to reduce the losses related to energy transport over long distances. Another fundamental advantage is given by the possibility of locating these structures away from urban centres, thus minimizing the direct effects of combustion-based pollutants on human health [36].

In the recent years however, the steep increase in worldwide population and energy consumption, together with the progressive depletion of fossil fuels, has evidenced the main issues of the centralised production system, which has started to show the first signs of crisis. From an environmental point of view, the growing concern for global warming and climate changes associated to the combustion of carbon-based fuels has driven the attention of governments and institutions towards renewable and cleaner sources of energy (solar, wind, hydroelectricity), which, stochastic in nature and characterised by a low energy density, are hardly matched by a centralised approach to power production. From the economical perspective instead, the increased fluctuations in fuel prices have considerably reduced the margin on the cost of energy of large power plants, increasing the risk for the investment in such infrastructures; this issue is amplified by the limited efficiency improvement available in the field of steam/gas technology, deriving from the current saturation of the thermal and mechanical resistance of employed materials. The increasing number of persons with access to electricity on the other hand enhances the inefficiency of the energy transport network, since a significant fraction of transmission losses occurs during the conversion of the plant high-voltage current to the end user low-voltage one.

A third critical aspect of the centralised strategy, which is often overlooked or underestimated, are its social ripercussions, assuming different characteristics basing on the scale considered: at a local level, a large energetic gap arises between urban and rural areas, due to the difficulty and costs of extending the transmission network over long distances, while at a global one, the unequal distribution of fossil fuels leads to a form of primary energy poverty in those countries that lack any form of indigenous reservoir as well as geopolitical stability. These issues are particularly severe in regions under development, where the growing access to electricity is not matched by adequate infrastructures [36].

Given this whole set of difficulties, the need has arisen in the international community to integrate the old centralised paradigm with a *distributed* approach to power generation, with a particular emphasis on the adoption of renewable sources; instead of few plants supplying the whole electricity network, a large number of small, compact and clean generating units are employed, located near the final consumer. Besides powering the end user, these also introduce energy into the grid at different levels, so that a constant and stable supply is globally ensured.

1.1.2 The role of wind energy in microgeneration

A further development of the distributed approach, which is acquiring more and more relevance in many economies, is represented by small scale embedded generation (SSEG) or *microgeneration*, i.e. the electricity or heat generation around individual buildings or households. This form of energy production involves small businesses and communities to meet their own needs while having the potential to combat fuel poverty, enriches the diversity of energy supply and offsets shortfalls in centralised generating capacity [54]. According to [27], microgeneration can also promote, when combined to renewable sources, a reduction in buildings environmental footprint and even in the personal energy usage through behaviour change.

In such context, an increasingly relevant role is played by small scale wind turbines (SWT), which, according to the definition given by the IEC in standard IEC-61400-2, consist in machines with a rotor swept area A lower than 200 m^2 and a rated power of 50 kW. Due to discrepancies in the adopted definition between different countries however, the current power upper limit leans towards 100kW. Basing on the most recent data of the World Wind Energy Association (WWEA) [61], the worldwide installed capacity has experienced an increase of more than the 200% in the period 2010-2015 (from 443.260 to 948.873 MW), and according to current forecasts, will raise up to 1.9 GW in 2020. As reported in figure 1.1, the global production is essentially distributed between 3 countries: China (44%), USA (25%) and UK (15%). Looking at the number of units installed, it can be seen how the average machine size strongly varies basing on the considered market, ranging from 0.56 kW in China to 5.1 kW in the UK. A particular case is represented by

Italy, which sports an average machine rating of 37.1 kW; as a matter of fact, it is the forth country for installed capacity, in spite of only 1725 machines available. Such distribution is strictly related to the field of application of these machines, which nowadays are for the major part employed in an off-grid context; it is no coincidence in fact that the lowest machine rating as well as the highest number of units are found in China and USA, where the the fraction of the population living in rural areas is extremely relevant. In China for instance, the percentage of off-grid units reaches the 97% of the total.

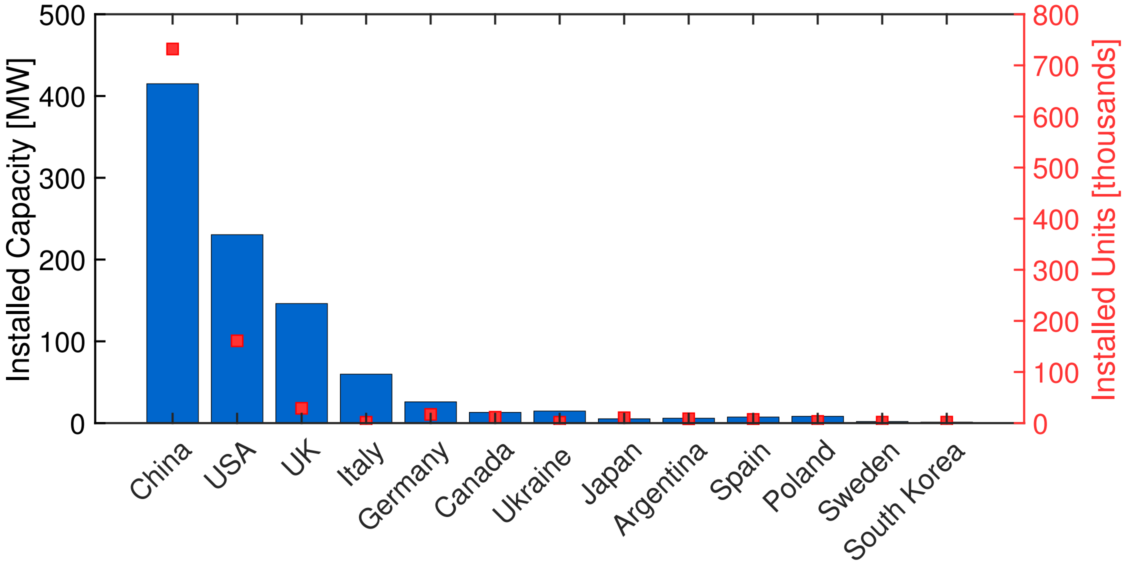

Figure 1.1: Worldwide SWT number of installations and corresponding capacity, subdivided by country [61].

In the recent years however, due to the increase in cities population and of the corresponding energy consumption (around 30% of the total in the only EU) [54], a renewed interest has arisen towards the exploitation of the wind resource in the urban environment. As it will be described in section 1.1.3 however, the design and optimisation of SWT in such context is extremely more difficult than in its rural counterpart.

1.1.3 The wind resource in the urban environment

In the urban environment, the interaction of wind with anthropic structures results in an highly complex flow pattern, making the proper exploitation of its energy an extremely challenging task.

The first and most important effect of the presence of high-density built areas is the formation of quasi stagnant flow layer in proximity of the ground, namely *roughness layer*, whose extension ranges from 2 to 4 times the average building height [54]. As clearly visible in figure 1.2, such phenomenon is responsible for the stratification of the atmospheric boundary layer, which divides in an external region, associated to the freestream wind configuration, and an internal one, directly influenced by the characteristics of the urban site.

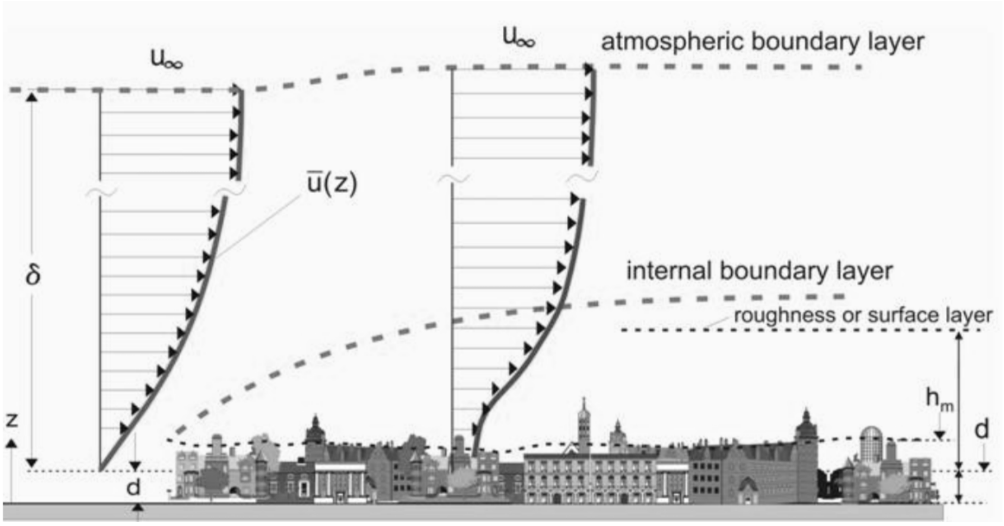

Figure 1.2: Stratification of the atmospheric boundary layer due to the interaction with the urban environment [5].

The internal boundary layer in particular does not start developing from ground level, but it is displaced in the vertical direction of a quantity d, according to the average velocity profile ū(z) reported in equation 1.1:

$$\bar{u}(z) = \frac{u_*}{k} \ln\left(\frac{z-d}{z_0}\right) \tag{1.1}$$

where $u_* = \sqrt{\tau/\rho}$ is the frictional velocity, defined as the ratio between the shear stress at ground level and the flow density, k is the Von Karman constant, usually assumed equal to 0.4, and z_0, namely roughness length, is a measure of the overall resistance offered by the urban substrate and depends on its configuration, as reported in table 1.1; this quantity also determines directly the displacement height d, which can estimated as $0.75z_0$ [43].

In such a complicated environment, the correct positioning of the machine becomes crucial for an optimal harnessing of the wind resource. On one hand, the low velocity found below the displacement height makes the exploitation of the wind in that region infeasible. On the other hand, the maximum positioning height is limited by the buildings vertical extension. As a consequence, the SWT rotor must be placed in the buffer zone between the roughness and the internal layers, which is nonetheless characterised, as evident in figure 1.2, by a severe average velocity gradient; a small error in the position estimation may result therefore in a strong penalty in turbine performance. The estimation process represents itself a challenging task, since, as previously described, the average velocity profile in the roughness layer is strictly related to the detailed morphology of the urban substrate, thus requiring ad hoc analyses with high-accuracy methods.

At the local level, the situation is further complicated by the flow features developing around buildings. Figure 1.3 shows an overview of the most common flow patterns found at the average building height, according to the classification proposed by Grimmond and Oke [24]; although strongly simplified with respect to the real case, which is fully three-dimensional, these illustrations are still able to

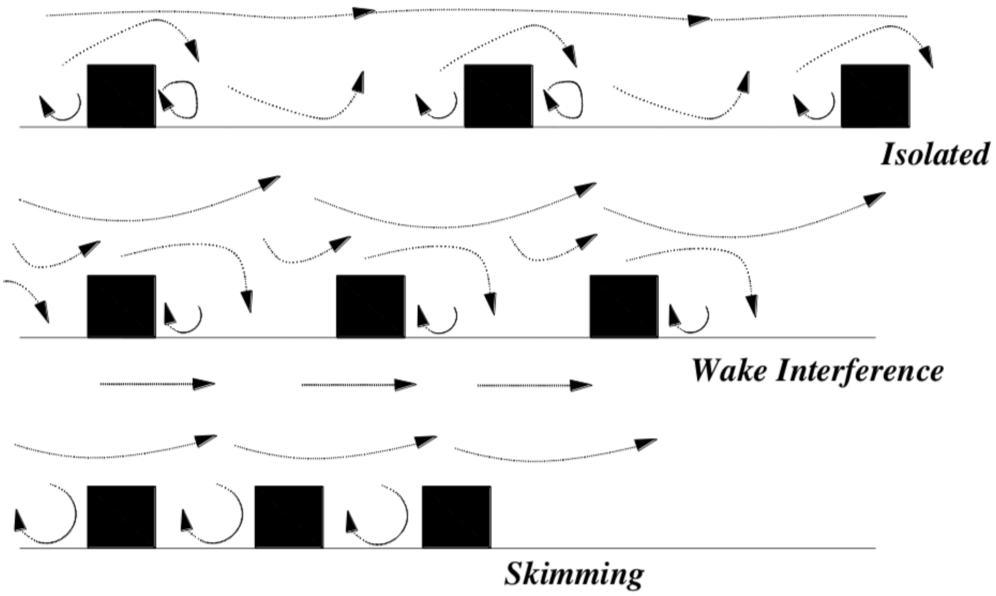

Figure 1.3: Various types of wind-building interaction [54].

give a rough idea of the complexity and variety of the flows encountered by SWTs operating in the urban environment. Three main configurations are presented:

- **Isolated:** for sufficiently low structural density, each building can be considered to be isolated from the others, presenting the aerodynamic characteristics of a bluff body; the flow on the roof is characterised by a large recirculation zone, developing from the building leading edge, and a region of skewed, accelerating flow, direct consequence of the blockage effect caused by separation. In such context, as highlighted by Mertens [43], the horizontal positioning of the turbine is fundamental. When placed in the separated region in fact, the machine will not only produce no power, but also be subjected to a severe unsteady aerodynamic forcing, due to the elevated levels of turbulence intensity. Its positioning in the skewed stream instead may even result, when the correct turbine is chosen, in an enhancement of performance with respect to the straight flow case. Another possibility given by this flow regime is the installation of the machine on the ground, where the building wake is fully recovered and the beneficial effect of urban tunnel acceleration can be exploited when the wind blows parallel to the streets [5].

- **Wake interference:** for medium construction density, wind progressively loses the possibility to recover its undisturbed status between the roughness elements, so that the wake shed by one building can interact with the neighbouring ones; although the main features of the isolated regime are still recognizable, the whole flow pattern is severely distorted, making turbine optimisation even more difficult.

- **Skimming:** for very high construction density, the urban flow configuration changes dramatically. The wind-turbine interaction zone is shifted above the averaged building height, while the flow at ground level is essentially stagnant and recirculating. In these conditions, both roughness length z_0 and displacement height d are maximised.

In general, being the actual city morphology far more intricate than the ones shown in figure 1.3, the flow pattern characterising real applications will be a mixture of the three base cases presented, as clearly visible in figure 1.4. It can be noted how, in such configuration, also the roofs of the shortest buildings may be fully immersed in a recirculation zone, thus being excluded from the available installation sites.

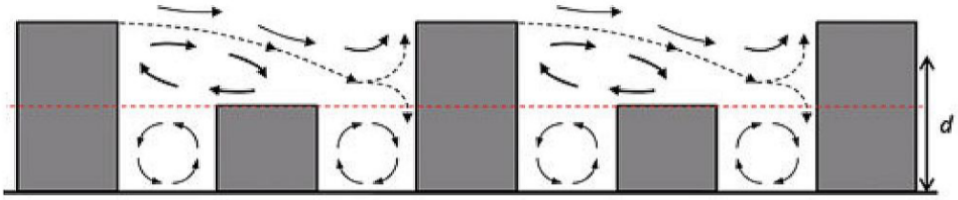

Figure 1.4: Schematic of the flow pattern developing in the urban environment due to the interaction with buildings of different heights [54].

Table 1.1: Davenport classification of the various landscapes morphologies and corresponding roughness level [16].

Roughness class	Roughness length z_0 [m]	Landscape morphology
Approx. open	0.1	Moderately open country with occasional obstacles (e.g. isolated low buildings or trees) at relative horizontal separation of at least 20 obstacle heights.
Rough	0.25	Scattered obstacles at relative distance of 8 to 12 obstacle heights.
Very rough	0.5	Area moderately covered by short buildings at a relative separation of 3 to 7 obstacle heights and no high trees.
Skimming	1	Densely built-up area without much building height variation.
Chaotic	2	City centres with mix of low and high-rise buildings (analysis by wind tunnel advised).

1.2 Small wind turbines architectures

In the context of microgeneration, the choice of the correct turbine architecture is pivotal for the proper harnessing of the wind resource, especially in complex environments such as the urban one (see section 1.1.3). Basing on the most recent data furnished by WWEA [61], the market of small wind turbines is currently dominated by the horizontal axis configuration (HAWT), which holds a share of 74% of the total; the elevated maturity and efficiency of such technology in fact, developed over the years in the frame of large wind farms, makes it the standard choice for off-grid and standalone applications, which represent the majority of the current demand (see section 1.1.2). The vertical axis concept (VAWT) accounts only for the 18% of the market, since the interest for these machines has been renewed only recently and it is hindered by the extreme complexity of their rotor aerodynamics, which, as it will described in section 1.3, requires advanced modelling and computational effort. Thanks to their robustness with respect to incoming flow conditions however, in the future they will give a relevant contribute to energy production in harsh environments such as cities. The remaining 6% is occupied by hybrid or alternative concepts. A third category, which is still in the embryonic stages, is given by Building Augmented Wind Turbines (BAWT), i.e. common wind turbines exploiting the installation building as concentrator of the wind resource. Such solution, if promising from a performances point of view, requires however the complete redesign of both machines and buildings, so it will not be implemented in the near future [42].

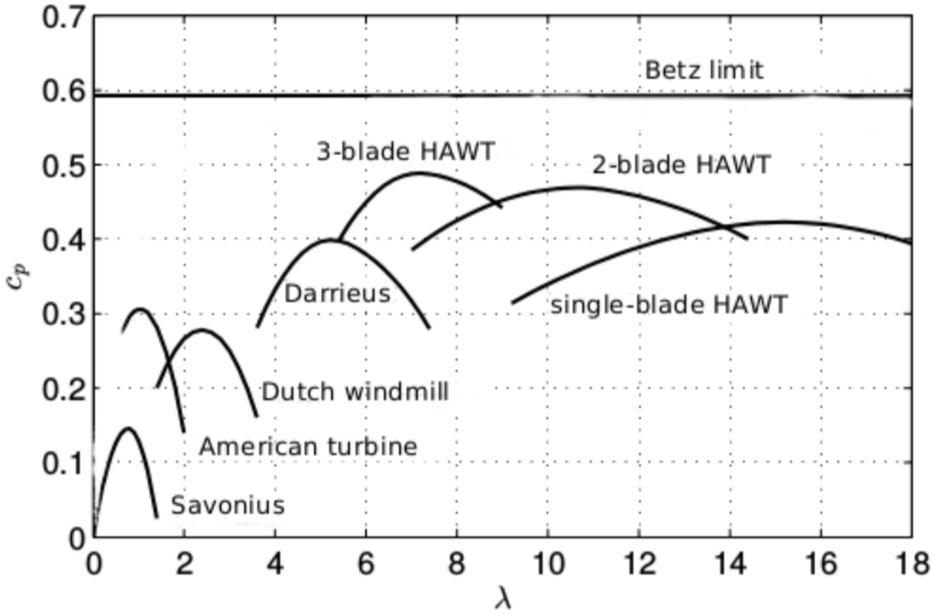

Figure 1.5: Power coefficient vs tip-speed ratio for different turbine architectures.

1.2.1 Horizontal Axis Wind Turbines (HAWT)

Nowadays, horizontal axis wind turbines represent the benchmark architecture in the field of wind energy. The arrangement of the axis of rotation in parallel direction with respect to the wind in fact guarantees a steady and efficient operation, improved over years of aerodynamic and structural optimisation in the frame of large wind farms.

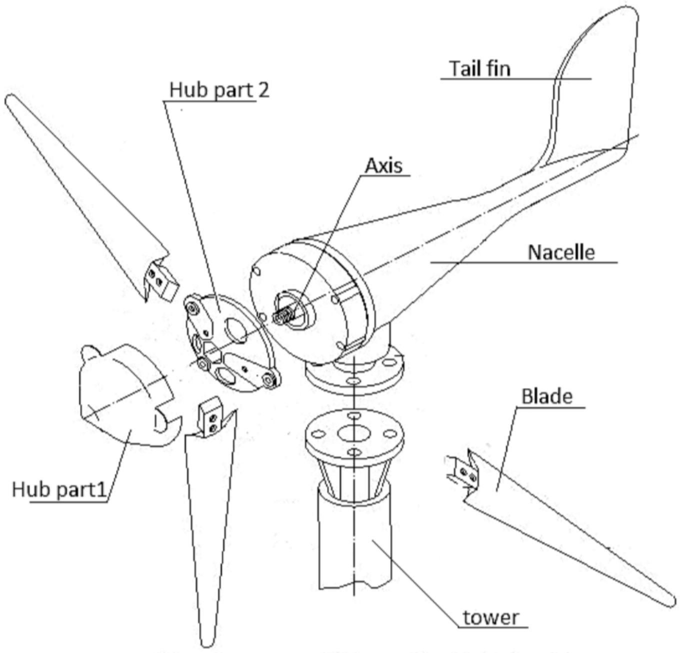

Figure 1.6: Exploded view of a HAWT for microgeneration [25].

In the recent years, this technology has been progressively transferred to small scale applications, with the necessary modifications and adaptations; the three blade configuration of the rotor has been preserved, however its connection with the generation unit has been strongly simplified, in order to reduce investment costs, by removing the gearbox and employing a mechanical braking system. This innovation has been made possible by the adoption of direct drive, brushless, permanent magnet electric generators. Following the same strategy, the active pitching and yawing mechanisms present on large HAWTs, required to control respectively the turbine power output and its orientation with respect to the wind, have been substituted by their passive counterparts. The yaw system in particular is implemented in most cases as a vaned tail mounted on the rear part of the turbine nacelle, as shown in figure 1.6, or, in case of downwind rotors, directly on the nacelle itself [5].

As it will be described in section 1.2.2, however this downsizing operation has not been completely successful in contexts, such as the urban one, characterised by complex and frequently variable flow conditions, due to issues intrinsically related to the horizontal axis configuration.

1.2.2 Vertical Axis Wind Turbines (VAWT)

Vertical axis wind turbines[1]are distinguished by an axis of rotation oriented in orthogonal direction with respect to the wind. Each blade is therefore subjected along its path to a periodic variation of the incident flow characteristics (angle of attack, relative velocity magnitude, Reynolds number), whose amplitude is directly related to the ratio between the peripheral speed of the blade ΩR and the freestream

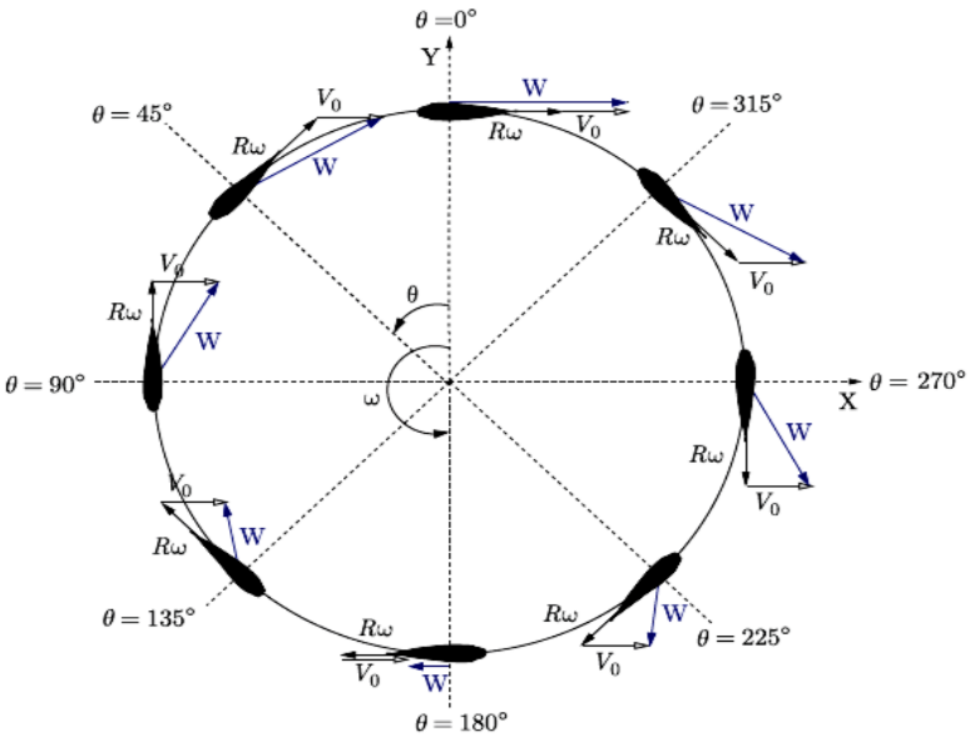

Figure 1.7: Variation of VAWT blade relative flow velocity and angle of attack over a revolution [18].

velocity of the wind U_0, or tip-speed ratio (TSR):

$$TSR = \frac{\Omega R}{U_0} \tag{1.2}$$

The maximum angle of attack fluctuations are observed at the lowest tip-speed ratios, where they bring the turbine profiles to work in stalled conditions for a relevant portion of their revolution; such phenomenon is associated not only to an enhanced irregularity of the overall torque production, but also to the presence of vortex-like structures which, shed from the blades in the front part of the machine (upwind), interact with them in the rear part (downwind), lowering their aerodynamic performance and increasing the mechanical and vibrational load. Going towards higher tip-speed ratios, such oscillations are progressively damped out, with a consequent stabilisation of the rotor operation and an improvement in the global efficiency. The corresponding increase in the blade loading is nonetheless sided by an enhancement of the blockage exerted by the front part of the turbine on the incoming flow, which is both decelerated and deflected in the transversal direction; the final result is a penalisation of performance in the downwind region, which beyond a certain TSR leads to an overall efficiency drop. In the whole operating

---

[1] In the current work, this nomenclature refers to lift-driven machines, i.e. exploiting the lifting effect deriving from wind-blade interaction to produce positive torque. Drag-driven architectures, such as the Savonius rotor, which instead are based on the exchange of momentum with the incident flow, are just mentioned here for completeness. Their low efficiency and high production cost in fact make them currently not of interest for grid-based generation.

range and especially at the higher TSRs, the flow field is further complicated by the presence of the rotor support system, i.e. the shaft and the struts connecting it to the blades, which represent a source of both parasitic drag torque and vortexes disturbing once again the downwind blade operation [2].

As it can be inferred from previous considerations, the vertical axis architecture is characterised by an extremely unsteady and complex rotor operation, which generally results in a maximum efficiency lower than the one achievable by HAWTs, as shown in figure 1.5, and in a more difficult aerodynamic and mechanical optimisation of the machine. Nonetheless, it presents multiple advantages with respect to the horizontal axis configuration, especially in problematic environments such as the urban one:

- **Omni-directionality of the rotor operation:** thanks to the rotational symmetry of the rotor with respect to its axis, the operation of a VAWT is virtually independent from the direction assumed by the wind; the consequent lack of a yaw system, either active or passive, makes these machines not only more simple and robust from the design perspective, but also more responsive to the frequent flow fluctuations found in the urban environment. Small HAWTs on the contrary, being not self-orienting, show a certain delay in their response to variable wind conditions, with a marked inability to capture random gusts, due to the inertia associated to their vane-based yaw system (see figure 1.6); this device may also be responsible for enhanced vibration and fatigue loading, in case its eigenfrequency corresponds to the one of the large turbulent fluctuations characterising the incoming flow [42].

- **Robustness with respect to skewed flow conditions:** as described in section 1.1.3, turbines positioned on top or next to buildings are normally subjected to a skewed flow configuration, i.e. tilted of a certain angle γ with respect to the horizontal direction. As reported by Mertens et al. [43], while HAWTs performance is progressively penalised with increasing γ, VAWTs are able to achieve a constant or even higher efficiency with respect to the straight flow case, at least for $\gamma < 40°$.

- **Lower noise emissions:** vertical axis machines tend to work at lower tip-speed ratios than their horizontal counterparts, thus operating with lower noise emissions; the aerodynamic noise level of the rotor is in fact proportional to the fifth power of the blade peripheral speed [43].

- **Lower manufacturing cost:** small VAWTs are characterised by an extreme structural simplicity, especially the H-Shaped Darrieus configuration; their blades feature only one type of aerodynamic profile over their whole span, usually symmetric and unstaggered, in neat contrast with HAWT ones, that presents a variation of both airfoil cross-section and chord from root to tip. Another simplification is given by the possibility of placing the generation unit (generator + gearbox) on the ground and by the absence of the yaw system. The set of these characteristics results in an overall lower manufacturing cost for the large-scale production of these machines.

- **Lower sun flickering effect:** when used in the built environment, HAWTs can cause sun flickering problems to a nearby observer, due to the low frequency passage (lower than 20 Hz) of the blades in front of the sunrays path. This issue is strongly dampened in VAWTs, thanks to their higher blade passing frequency (the rotor blades pass twice in front of the sunrays during a revolution).

At the current status of the technology nonetheless, this configuration still presents considerable disadvantages, that so far have penalised it with respect to the horizontal axis one. The large unsteadiness in torque generation results on one side in a discontinuous electricity output, making the connection of the machine to the grid more difficult, on the other side in a severe fatigue loading on the blades, possibly enhanced by vibrational issues; this phenomenon is particularly dangerous in the urban context, where the rip-off of a blade may result in the injury of the end user [42]. A similar problem is associated to the presence of the tower, which is usually required to position the turbine at the correct height; according to [2] in fact, the dynamic coupling between the modes of vibration of the support structure and those of the rotor may lead to resonance of the whole machine, with disastrous effects on its structural integrity. The dominant issue associated to VAWTs is however their inability to self-start, due to the extremely low aerodynamic efficiency of the blades at the lowest tip-speed ratios; many workarounds have been proposed to overcome the problem, such as hybrid drag/lift-driven concepts, but they are still under study and for now they do not represent a concrete solution.

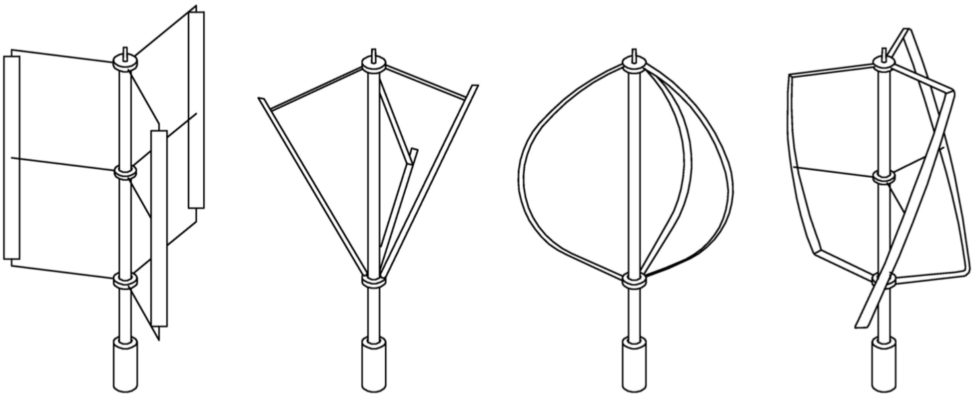

Figure 1.8: Various Darrieus rotor architectures. From left to right: H-Shaped, V-Shaped, Troposkien and Gorlov [2].

In the context of microgeneration, the vertical axis architecture is distinguished by a large variety of designs, most of them based on the work of the french inventor Jean Marie Georges Darrieus, in the years from 1920 to 1940. As a consequence, they commonly take the name of "Darrieus turbines". These machines were in the following years further developed and engineered by various research laboratories in the UK (University of Reading) and USA (Sandia National Laboratory, DOE) [2].

The original concept proposed by Darrieus is the *Troposkien* or *Eggbeater*, which consists of 2 or 3 curved blades directly attached to the machine support shaft, as shown in figure 1.8. From a structural point of view, the extreme simplicity of this configuration results in a lower weight and polar inertia. Furthermore, the particular shape of its blades, which approximates the one assumed by a spinning rope hung at its extremities, allows to minimize the overall radial bending stress associated to centrifugal loading; this solution not only allows to reach higher rotational speeds, but also to maximise the turbine structural efficiency, via the adoption of high-strength composite materials; these in fact perform best under pure tension. At given rotor swept area, this rotor geometry also results in an higher aerodynamic efficiency with respect to other models, such as the H-Darrieus; the equatorial region in fact, where a considerable fraction of the incoming wind is elaborated, benefits from an higher average Reynolds number (the larger diameter corresponds to a higher peripheral speed) and a lower influence of the tip large-scale flow structures, thanks to the absence of free blade extremities. A relevant contribute is also given by the lack of support struts, with the associated drag losses [48].

The major disadvantage of the Troposkien rotor is its relatively high production effort, essentially related to the manufacturing of the blades. In such perspective, a noteworthy improvement, although at the cost of a lower aerodynamic and structural efficiency, is represented by the *H-Shaped Darrieus* turbine, as the one analysed in the present work. The standard configuration is made up of three straight blades, connected to the central shaft in a cantilever fashion via a set of support arms. Their constant spanwise development makes them particularly suited to large-scale production techniques, such as direct one piece extrusion, thus lowering their individual cost [48].

In order to overcome some of the limits associated to this design, many variants have been proposed over the years. One the most promising is the *Gorlov* turbine, patented by Prof. Alexander Gorlov in 2001, shown in figure 1.8. Its twisted blades are able to strongly reduce the torque ripple usually associated to VAWT operation, achieving a more uniform power output, lower noise emissions and higher structural reliability [2].

1.3 Aerodynamic models for VAWTs

As anticipated in section 1.2.2, the complexity of the Darrieus rotor aerodynamic and structural behaviour makes its proper design and optimisation an extremely challenging task, especially for problematic environments such as the urban one (see section 1.1.3). For the purpose, high-fidelity advanced numerical models must be employed, capable to capture the interaction between the atmospheric boundary layer, the buildings and the turbine, together with its effect on the overall power extraction and mechanical loading; in such perspective, it is particularly relevant the accuracy of the method in the prediction of the wake, which plays a fundamental role in determining the correct positioning of the machine with respect to the other elements of the landscape, other turbines above all.

Among the several models proposed over the years, it is possible to distinguish three main categories, characterised by different theoretical foundations, accuracy and computational effort: the *streamtube models*, based on the integral conservation of mass and momentum across the rotor, the *vortex models*, which evaluate the wind-turbine interaction by enforcing the conservation of vorticity between the rotating blades and the wake, and the *CFD models*, able to achieve a complete description of the flow field developing around the machine from the resolution of the discretised Navier-Stokes equations over the problem domain.

1.3.1 Double Multiple Stream Tube (DMST)

The Double Multiple Stream Tube is currently the most advanced approach of the streamtube family of methods, which derives directly from the Blade Element Method (BEM) originally developed for HAWTs. It was proposed by Prof. Paraschivoiu in 1983 [47] to overcome the limits of the Multiple Stream Tube (MST) approach, not capable of modelling the deceleration induced by the upwind section of the turbine on the flow interacting with the downwind one (blockage effect).

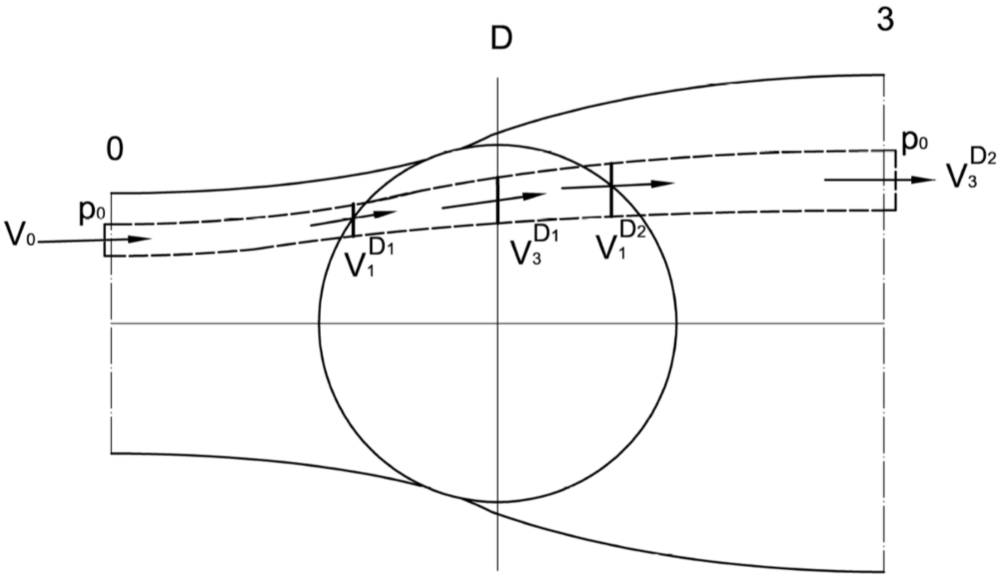

Figure 1.9: Discretisation of the rotor swept area into multiple streamtubes, on a plane orthogonal to the turbine axis.

In its basic formulation, the portion of wind running through the turbine swept area is discretised into several streamtubes in both spanwise and transversal directions, as shown in figure 1.9. The interaction of each streamtube, which is assumed to be independent from the others, with the turbine blades is modelled following the actuator disk approach typical of BEM. The aerodynamic forces exchanged with the profile result in average terms in a flow deceleration, quantified by the induction factor α^{Di}:

$$\alpha^{Di} = \frac{V_1^{Di}}{V_0} \tag{1.3}$$

where $\mathrm{V}_1^{\mathrm{Di}}$ is the local flow velocity at the actuator surface, V_0 the freestream one. Combining this information with the kinematic and geometric parameters of the turbine, it is possible to evaluate the local flow conditions (blade relative velocity magnitude, angle of attack), serving then as input for the available tabulated polar data and so for the computation of exchanged aerodynamic forces. Since the induction factor depends in turn from the loads on the blade via the conservation of mass and momentum across the considered streamtube, the solution process has an iterative character. The whole procedure is applied first to the upwind region and then repeated in the downwind one, using as undisturbed velocity $\mathrm{V}_3^{\mathrm{D1}}$ the one assumed by the flow after its interaction with the front part of the machine, i.e. $\mathrm{V}_1^{\mathrm{D1}}$. In this way, a more accurate description of the flow field across the rotor is achieved, possibly accounting for asymmetries introduced by phenomena such as dynamic stall or flow curvature [2]. The assembling of the information coming from all streamtubes allows eventually to derive the angular profiles of the quantities of interest (extracted power, torque, transversal and streamwise thrusts, etc...) over a rotor revolution.

Generally speaking, the DMST model has proven to be quite reliable in the prediction of the turbine global performances, i.e. power and thrust coefficients, when integrated by the proper set of sub-models (flow curvature, dynamic stall, streamtube expansion, struts losses, etc ...). Its accuracy nonetheless drops significantly at the local level, in terms of both instantaneous flow conditions and loads on the blades; such deficiency can be mainly attributed to the intrinsically low resolution of the method, which is not able to capture neither the flow pattern in the wake nor the vortical structures shed during rotor operation. In such perspective, a relevant contribution is given by the assumption of considering the streamwise induction factor only, not accounting for flow deflection in transversal direction [8]. Furthermore, the method is not able to cope, due to its own formulation, with not uniform flow inlet conditions, resulting unsuitable for the simulation of complex and turbulent environments.

As a consequence of the combination of these characteristics and its very low computational effort, the DMST finds its natural field of application in the preliminary design of VAWTs.

1.3.2 Vortex methods

Vortex methods represent a special category in the frame of aerodynamic models. They exploit the conservation of vorticity, rather than that of mass and momentum, to evaluate the mutual interaction between the flow field developing around the turbine blades and in the wake and the exchanged aerodynamic forces. Depending on how this concept is implemented, it is possible to distinguish two main approaches: the Lifting Line Theory (LLT) and Vortex Panel Method (PM).

Lifting Line Theory (LLT)

In Lifting Line Theory, the bound vorticity field around the blade is discretised as a spanwise array of single vortex filaments, concentrated in the center of pressure of the respective blade sections. The strength of each vortex source is expressed in terms of circulation Γ, defined as the line integral of the velocity **U** along the profile or, in an equivalent way, as the surface integral of the vorticity field $\boldsymbol{\omega}$:

$$\Gamma = \oint_C \boldsymbol{U} \cdot d\boldsymbol{l} = \iint_S \boldsymbol{\omega} \cdot d\boldsymbol{S} \tag{1.4}$$

and related to the lift and drag components of the exchanged aerodynamic force via the Kutta-Joukowsky theorem. In order to evaluate the effect of wind-blade interaction on the global flow field, the conservation of circulation stated by the Kelvin theorem is exploited:

$$\frac{d\Gamma}{dt} = \frac{d\Gamma_{airfoil}}{dt} + \frac{d\Gamma_{wake}}{dt} = 0 \tag{1.5}$$

According to equation 1.5, a variation over time of the aerodynamic load on the profile and so of the bound vorticity Γ_{airfoil} results in the shedding of a free-floating vortex filament in the wake, as shown in figure 1.10a; the simultaneous action of the two vortex systems results in a deformation of the undisturbed velocity field, quantified by the Biot-Savart law. Combining this information with the kinematic and geometric parameters of the turbine, it is possible to compute the average profile relative flow velocity and angle of attack; these two quantities are used in turn to evaluate the exchanged aerodynamic forces via available tabulated C_L, C_D coefficients. As a consequence, the whole process has an iterative character.

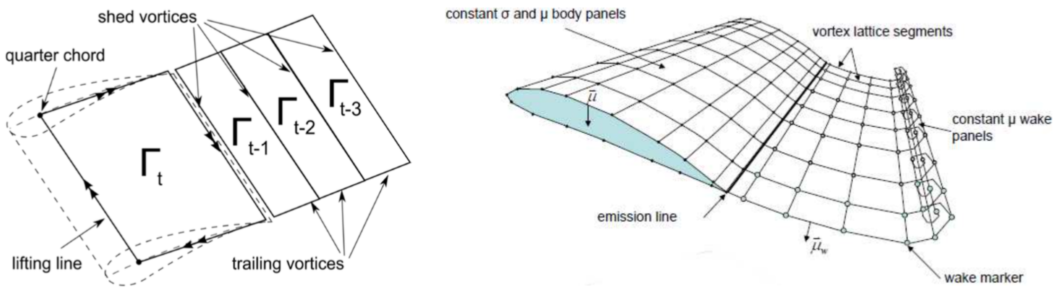

(a) LLT [35] **(b)** PM

Figure 1.10: Comparison between the discretisation strategies adopted in LLT and PM vortex methods.

The method formulation is intrinsically unsteady, since the progressive build-up of concentrated vorticity filaments in the wake modifies the predicted velocity field over time. If on one side this implies an increase in the overall computational time, dictated by the necessity of reaching a periodic solution, on the other side it determines a relevant improvement in temporal accuracy with respect to BEM models, making LLT suitable for the simulation of the turbine transient behaviour, e.g. start-up, or for aeroelastic applications. In contrast with DMST, this approach is also able to fully resolve the flow field developing around the machine, including the wake, with a relatively low modelling effort; many of the phenomena for which the DMST requires an ad hoc sub-model, such as tip losses, are in fact already embedded in LLT base formulation [35].

Vortex Panel Method (PM)

In contrast with LLT, the Panel Method (PM) adopts a local approach, focused on evaluating the vorticity field developing around the airfoil and in the wake. For the purpose, the turbine blade is discretised into multiple panels, each one characterised by its own value of flow velocity and bound vorticity, as shown in figure 1.10b. The solution procedure follows the same principles adopted in LLT, even if with an important difference; the assessment of lift and drag forces in fact does not rely any more on tabulated coefficients given in input to the solver, but is carried out by integrating directly the computed pressure field over the airfoil surface. More information about the governing equations and the solution algorithm can be found in appendix A.

In the frame of VAWTs simulation, the PM method presents a relatively high computational effort, considering its resolution capability; in order to accommodate the development of the flow field around the rotor in fact, the number of panels progressively increases over time. Therefore, it has been partially overshadowed by the other approaches. Nonetheless, its reliability and efficiency in the computation of aerodynamic coefficients in the attached flow region has made it one of the standard tools for the derivation of polar data.

1.3.3 Computational Fluid Dynamics (CFD)

Computational Fluid Dynamics (CFD) is an extremely powerful simulation technique, capable to reproduce a wide variety of flows with a relatively high accuracy. Thanks to these characteristics, this technique has become a standard research and verification tool in many sectors of the industry, such as the aerospace or the automotive one, where it has replaced in many aspects the experimental analysis; as a matter of fact, it allows not only a significant reduction of the time and costs associated to a new testing campaign, but also to study systems in which measurements are very hard or impossible, for instance the combustor of a jet engine or the tip of a large HAWT blade. Its main drawbacks are the elevated difficulty of implementation, which requires expertise in both fluid mechanics, numerical analysis and informatics, and its large computational effort, which in many cases represents a strong limit on the accuracy of the method. In the recent years however, the latter issue has been partially resolved by the availability of affordable high-performance hardware and computer clusters, further promoting the diffusion of this technique.

Governing equations

The main aim of CFD is the resolution of a specific flow pattern via the application of the conservation laws regulating the mechanics of fluids, here reported in differential form, i.e. for an infinitesimal control volume. It is possible in particular to distinguish three main governing equations, one for mass, one for momentum and one for energy.

The *mass conservation* equation imposes the variation over time of the mass contained in one fluid volume to be equal to the net mass flow across its faces, thus ensuring the continuity of the global flow motion, i.e. the absence of separation or compenetration between its constitutive elements:

$$\frac{\partial \rho}{\partial t} + \nabla \cdot (\rho \boldsymbol{U}) = 0 \tag{1.6}$$

The *momentum conservation* equation enforces the congruence, derived from Newton's second law of dynamics, between the rate of change of momentum $\rho\mathbf{U}$ of the considered control volume, the momentum fluxes across its faces and the whole set of external forces applied on it, which includes both volume and surface contributions.

$$\frac{\partial(\rho \boldsymbol{U})}{\partial t}+\nabla\cdot(\rho\boldsymbol{U}\otimes\boldsymbol{U})=\rho\mathbf{f}-\underbrace{\nabla P+\nabla\cdot[\mu(\nabla\boldsymbol{U}+\nabla\boldsymbol{U}^T)]-\nabla\cdot\left(\frac{2}{3}\mu\nabla\cdot\boldsymbol{U}\right)}_{\text{surface stresses}} \tag{1.7}$$

From the corresponding term in equation 1.7, it is possible to distinguish two types of surface stresses: an inviscid normal stress component, associated to the pressure gradient ∇P, and a viscous one. The latter can be further divided into a shear contribution, proportional to the deviatoric component of the velocity gradient tensor ($\nabla\mathbf{U} + \nabla\mathbf{U}^{\mathrm{T}}$) via the dynamic viscosity μ (newtonian fluid), and a normal one, representing the effects of volumetric expansion on the flow and related to the divergence of the velocity vector $\nabla\cdot\mathbf{U}$. Volume forces instead, such as gravitational or electromagnetic fields, are embedded in the source term $\rho\mathbf{f}$.

Finally, the *energy conservation* equation, or first law of thermodynamics, regulates the variation of the control volume total energy ρe, defined as the sum of internal and kinetic energy, with respect to the exchanged fluxes, heat and external forces work across its boundaries:

$$\begin{aligned}\frac{\partial(\rho e)}{\partial t}&+\nabla\cdot(\rho e\boldsymbol{U})=\rho\mathbf{f}\cdot\boldsymbol{U}-\nabla\cdot(P\boldsymbol{U})+\nabla\cdot[\mu(\nabla\boldsymbol{U}+\nabla\boldsymbol{U}^T)\cdot\boldsymbol{U}]\\&-\nabla\cdot\left(\frac{2}{3}\mu(\nabla\cdot\boldsymbol{U})\cdot\boldsymbol{U}\right)+\rho Q+\nabla\cdot(\lambda\nabla T)\end{aligned} \tag{1.8}$$

It must be noted the presence of two additional terms with respect to equation 1.7, given by heat volumetric generation ρQ and diffusion across the cell faces, related to temperature gradient ∇T via the material thermal conductivity λ.

The set of equations 1.6, 1.7 and 1.8 takes the name of compressible Navier-Stokes (NS) equations, a non-linear, partial differential system which regulates the behaviour of most fluid flows. Its resolution is extremely difficult due the presence of many non-linear coupling terms, in particular the momentum convective flux $\nabla\cdot(\rho\boldsymbol{U}\otimes\boldsymbol{U})$ from equation 1.7, responsible for the elevated complexity characterising the CFD technique.

Solution algorithm

Most CFD codes, such as the OpenFOAM framework used for the current work, rely for the resolution of the NS equations on the Finite Volume Method (FV), consisting in the discretisation of the domain into a series of control volumes, or *cells*, which can assume different shapes according to the geometry and the characteristics of the problem to be solved. The resulting computational grid is called *mesh*. As shown in figure 1.11a, each cell is identified by its centroid $\mathbf{x}_{\mathrm{P}}$, where the local values of the fields of interest (velocity, pressure, etc...) are defined, and by an arbitrary number of faces, each one with its own centroid $\mathbf{x}_f$, where the interaction with neighbouring cells occurs. Definition of these two quantities can be found in equations 1.9 and 1.10:

$$\boldsymbol{x}_P : \int_V (\boldsymbol{x} - \boldsymbol{x}_P) dV = 0 \tag{1.9}$$

$$\boldsymbol{x}_f : \int_S (\boldsymbol{x} - \boldsymbol{x}_f) dS = 0 \tag{1.10}$$

where V is the cell volume, S the surface of the considered cell face and **x** the position of the generic point in space.

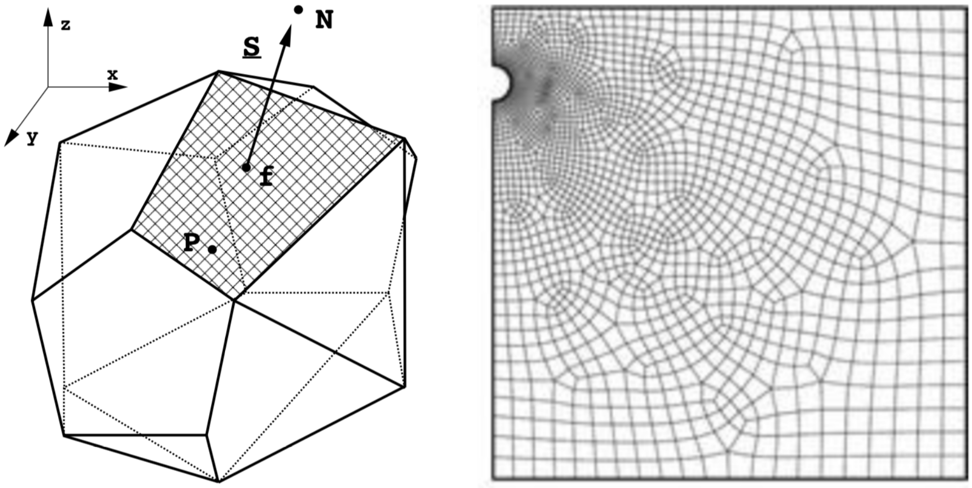

(a) Generic control volume [28] (b) Unstructured mesh

Figure 1.11: Overview of the discretisation strategy used in the finite volume method.

This fundamental unit serves as support for the application and subsequent resolution of the integral conservation laws deriving from the physical modelling of the system. Such process can be illustrated starting from the generic unsteady convection-diffusion equation in integral form, commonly found in most fluid-dynamic applications:

$$\underbrace{\int_V \frac{\partial(\rho\varphi)}{\partial t} dV}_{\text{time derivative}} + \underbrace{\int_V \nabla \cdot (\rho \boldsymbol{U} \varphi) dV}_{\text{convection term}} - \underbrace{\int_V \nabla \cdot (\rho \Gamma_\varphi \nabla \varphi) dV}_{\text{diffusion term}} = \underbrace{\int_V q_\varphi dV}_{\text{source term}} \tag{1.11}$$

Depending on the term of equation 1.11 considered, different discretisation strategies are adopted:

- **Time derivative term:** the time derivative term accounts for the variation over time of the generic quantity φ in the cell volume. There are many approaches to its discretisation, however in this context it has been decided to present only the simplest and more robust one, i.e. the Euler scheme; considering only the temporal evolution of the centroid value φ_P and assuming its linear variation over the cell volume, it is possible to write the time derivative term as:

$$\int_{V_P} \frac{\partial(\rho\varphi)}{\partial t} dV = \frac{\rho_P \varphi_P^n - \rho_P \varphi_P^o}{\Delta t} V_P \tag{1.12}$$

where the superscripts n and o refer respectively to the current and previous timesteps, while Δt is the adopted temporal discretisation. Depending on which temporal field the spatial terms are evaluated from, the method is defined as explicit or implicit; due to the intrinsic instability of the former, the latter represents the standard in most CFD codes.

- **Convection term:** the convection term models the bulk mass transport of the generic quantity φ between two regions of the flow domain, in this case represented by two neighbouring cells. Exploiting the Gauss divergence theorem, it is possible to transform the volume integral contained in equation 1.11 in a surface one, which is then distributed among the different faces of the considered cell. Evaluation of these surface integrals occurs in most cases via the *midpoint rule* (linear variation of φ over the face), even though more advanced methods are available:

  $$\begin{aligned}\int_{V_P} \nabla \cdot (\rho \boldsymbol{U} \varphi) dV &= \sum_f \int_{S_f} (\rho \boldsymbol{U} \varphi) \cdot d\boldsymbol{S} = \sum_f \boldsymbol{S}_f \cdot (\rho \boldsymbol{U})_f \varphi_f \\ &= \sum_f F_f \varphi_f \end{aligned} \tag{1.13}$$

  where F_f is the face mass flux, while the subscript f refers to quantities evaluated at the face centroid $\mathbf{x}_f$. In such perspective, the differentiation scheme used to extrapolate φ_f from the corresponding cell centroid values plays a fundamental role in determining the overall accuracy and stability of the method.

- **Diffusion term:** the diffusion term models the transport of the generic quantity φ from an high- to a low-concentration region in the flow domain. Its discretisation procedure is similar to the one used for convection, leading to the following expression:

  $$\int_{V_P} \nabla \cdot (\rho \Gamma_\varphi \nabla \varphi) dV = \sum_f \int_{S_f} (\rho \Gamma_\varphi \nabla \varphi) \cdot d\boldsymbol{S} = \sum_f (\rho \Gamma)_f \boldsymbol{S}_f \cdot (\nabla \varphi)_f \tag{1.14}$$

  where Γ_f is a characteristic diffusion constant, while $(\nabla \varphi)_f$ is the φ face gradient, whose value is extrapolated from the information available at the centroids of neighbouring cells via an ad hoc differentiation scheme.

- **Source term:** the source term includes the contributions of all the phenomena which cannot be modelled as convective or diffusive and is in the most general case an arbitrary function of φ. Its discretisation procedure is similar to the one used for the time derivative term, leading, after its proper linearisation, to the following expression:

  $$q_\varphi = C_{q1} + C_{q2} \varphi \quad \rightarrow \quad \int_{V_P} q_\varphi dV = C_{q1} V_P + C_{q2} V_P \varphi_P \tag{1.15}$$

  where C_{q1}, C_{q2} are two constants deriving from the linearisation process.

The final result of the discretisation process is the conversion of the initial partial differential equation 1.11 to its algebraic equivalent, being for the single cell:

$$a_P \varphi_P^n + \sum_N a_N \varphi_N^n = R_P \tag{1.16}$$

while for the entire system it becomes:

$$[A][\varphi] = [R] \tag{1.17}$$

where [A] is a sparse matrix, with coefficients a_P on the diagonal and a_N off the diagonal, $[\varphi]$ is a vector containing the centroid values of φ for all control volumes, while [R] is the source term vector. Resolution of equation 1.17 occurs via ad hoc algorithms, such as the PISO described in section 3.1.2 and used in the current work, after the proper boundary and initial conditions have been applied. For a detailed description of the Finite Volume method, please refer to [28].

CFD models for VAWTs

In the frame of VAWTs analysis, the great flexibility of the CFD technique has given birth over the years to a wide variety of methods, aimed at finding the best trade-off between accuracy, implementation effort and computational time.

As a matter of fact, the direct application of CFD to VAWTs, which implies the full solution of the incompressible NS equations (see section 3.2) and the complete discretisation of the rotor geometry, as shown in figure 1.12a, have proved to be too cumbersome to be used for design and optimisation, thus remaining restricted to the research context; the elevated mesh density and reduced timestep required to resolve the complex aerodynamics of Darrieus rotors make the simulation of these machines extremely heavy, if not infeasible for the currently available computational power, even with a full turbulence modelling (RANS).

Among the different approaches that have been proposed, two in particular stand out: the actuator swept-surface (ASSM) and the actuator line method (ACL). Both methods combines a BEM-based modelling of the turbine with the Finite Volume (FV) discretisation of the flow domain; each blade is divided into N elements, assumed to behave aerodynamically as a two-dimensional airfoil. The forces exchanged with the wind are determined from the local flow conditions, via the available tabulated polar data; they are then plugged into the computational grid, so that the flow field around the machine can be accurately resolved by means of CFD. In the ASSM, the wind-blade interaction is modelled in a steady way, by distributing the time-averaged actuator forces over the turbine swept area (see fig. 1.12b). For the H-Shaped Darrieus rotor for instance, this surface takes the form of an actuator cylinder. In the ACL instead, each blade is replaced by a dynamically equivalent actuator line, introducing aerodynamic forces at each timestep into the computational grid basing on its current position and the instantaneous local flow conditions (see fig. 1.12c); this approach allows a more accurate resolution of the interaction between the turbine blades and time-variant structures such as vortexes or their own wakes [51]. A detailed description of the method can be found in section 3.1.

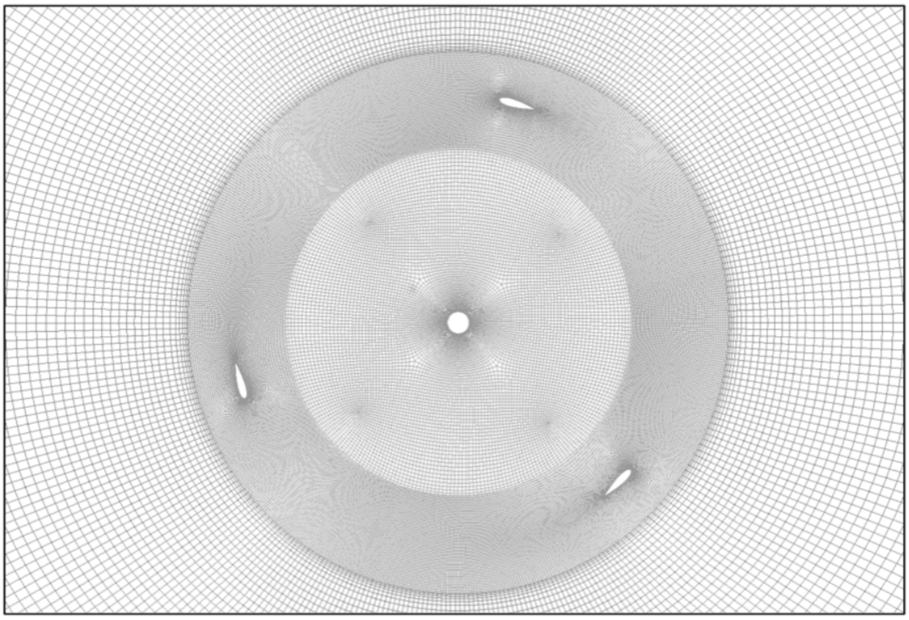

(a) CFD (fully resolved) [1]

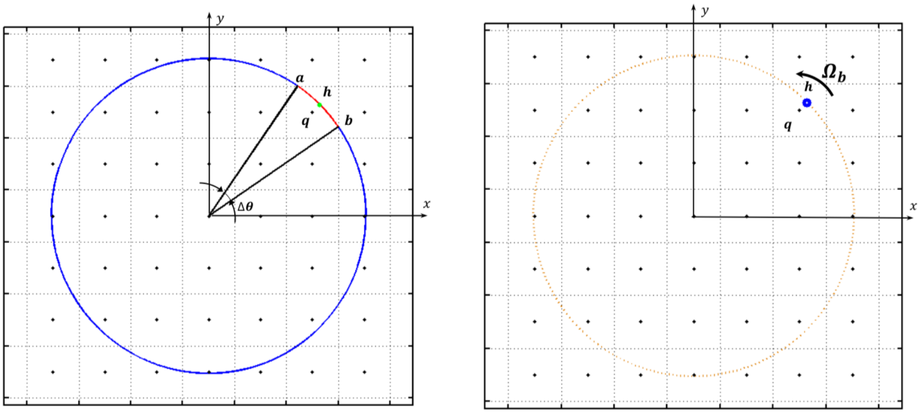

(b) ASSM [51] **(c)** ACL [51]

Figure 1.12: Comparison between the different rotor discretisation strategies adopted in the CFD (fully resolved), ASSM and ACL methods.

The main advantage of ASSM and ACL is a strong reduction of the implementation effort and elaboration time associated to a fully resolved CFD simulation; being based on blade-element theory, they do not require in fact the resolution of the boundary layer encompassing the blade surfaces, with a corresponding strong decrease in the required computational resources [51]. Such feature, combined with the virtually unlimited variety of flows manageable by CFD, makes them the most promising tool for the simulation of VAWTs in complex and turbulent environments, the urban one above all. Their main drawback, inherited from BEM, is the elevated sensitivity to input aerodynamic data and employed sub-models, which thus demand extreme care in their derivation and implementation. For the same reason, this class of models usually requires a large experimental and numerical validation effort, before they can be used in a reliable way.

Chapter 2

Wind Tunnel Tests

In this chapter, a detailed overview of the experimental campaign, which served as validation benchmark for the ACL simulation tool employed in the current work, is presented. In particular, the H-shaped rotor used for the tests is thoroughly described in section 2.1, while the characteristics of the testing facility and the set-up of the measurement apparatus are reported in section 2.2. The chapter is completed by the illustration of the post-processing techniques adopted to derive the benchmark data from the raw experimental ones (see section 2.3).

2.1 Test turbine

Object of both the experimental and numerical test campaigns presented in the current work is a real-scale H-Shaped Darrieus turbine for microgeneration (see figure 2.1a), whose main specifics are reported in table 2.1.

The rotor, designed by the company Tozzi-Nord Wind Turbines, features three straight blades, arranged at an angular distance of 120° one from the other and connected to the central shaft by means of a set of aerodynamically shaped aluminium spokes. Each blade was manufactured by covering a wood core with a carbon fiber reinforced polymer (CFRP) shell, obtained with the technique of infusion molding.

In occasion of the experimental campaign, such component was mounted on an ad hoc test bench, illustrated in figure 2.1b, which hosted on hand the power unit, properly controlled by means of an inverter to achieve a constant turbine rotational speed, on the other hand the performance measurement system. The latter was equipped by the staff of University of Trento with the following set of calibrated sensors:

- two *axial accelerometers*, installed on the upper part of the supporting mast to monitor the streamwise and transversal vibrations of the structure.

- two *strain gauge bridges*, mounted on the rotor shaft in order to measure both streamwise and transversal aerodynamic thrusts.

- an *absolute encoder*, required to measure the turbine rotational speed and the azimuthal position of the rotor.

- a *torque meter*, inserted between the elastic joints connecting the rotor to the test bench, to measure the mechanical torque at the shaft.

A complete description of both turbine and test bench, including quoted dimensions, can be found in [4].

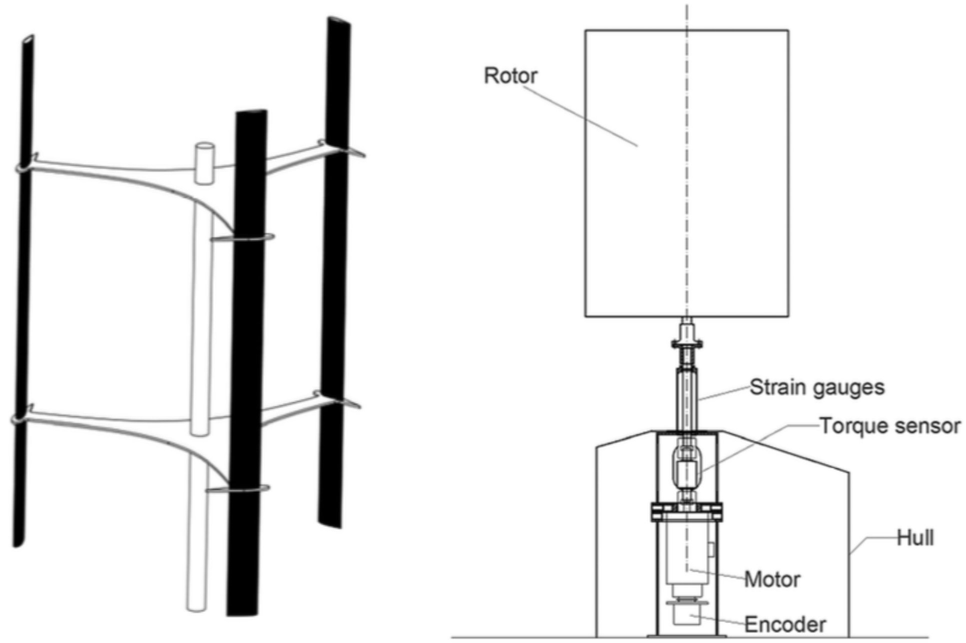

(a) Turbine rotor **(b)** Sketch of the test bench

Figure 2.1: Test H-Shaped Darrieus turbine [17].

Table 2.1: Characteristics of the H-Shaped Darrieus turbine used in wind tunnel tests.

Blade height (2H) [m]	1.457
Rotor diameter D [m]	1.030
Blade profile	NACA0021 (unstaggered)
Number of blades N_b [-]	3
Solidity σ=$N_b c/D$ [-]	0.25

2.2 Experimental set-up

The tests were carried out in the large-scale wind tunnel of the Politecnico di Milano (Italy), in particular in the high-speed, low-turbulence section of the facility; this closed-loop test chamber (4 m wide, 3.84 m high and 6 m long) features two rows of seven electric driven fans, with an overall installed capacity of 1.4 MW, allowing to reach wind velocities up to 55 m/s. The presence of an anti-turbulence system, consisting in a combination of honeycombs and special screens, ensures a steady and spatially uniform flow, with a measured turbulence intensity at the chamber inlet lower than 1%; this controlled conditions, although different from those experienced by the machine during its actual operation, are ideal for the successive validation of simulation tools, which may suffer from the uncertainty in the input data [4].

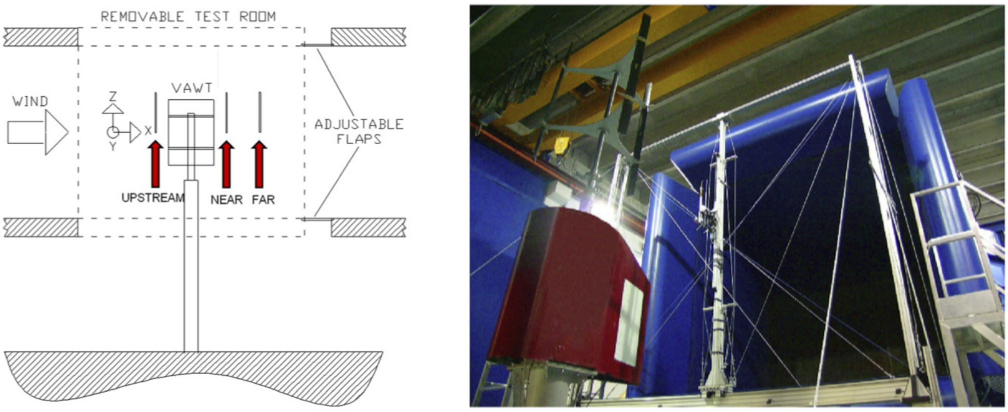

(a) Measurement section [17] **(b)** Bottom view of the open chamber set-up [4]

Figure 2.2: Overview of the set-up used for the open-jet tests.

In order to minimize the interference (blockage) exerted by the wind tunnel, the full cross-section of the chamber was exploited, removing the mobile test room and placing the machine in the centre of the jet, as shown in figure 2.2; the presence of physical walls limits in fact the expansion of the flow around the turbine, leading to an acceleration of the corresponding streamtube and so in an overestimation of the global machine performance with respect to the real case. According to [17], this open-jet configuration allowed to mimic almost perfectly the open-field operation of the turbine, with a blockage correction limited to the 1.5%.

Depending on the considered quantity, different measurement systems were implemented; as anticipated in section 2.1, an ad hoc test bench, directly connected to the rotor, was employed for the monitoring of torque and rotational speed, while the investigation of the flow development in the wake was carried out via two instrumented traverses, positioned respectively 0.75D and 1.5D downstream of the shaft. Each traverse consisted of 21 sampling points and extended 3 turbine diameters in transversal direction and 1.25 blade half-heights in the spanwise one, so that a full coverage of the wake could be ensured also at the highest TSRs, where it notably expands with respect to the machine cross-section [17]. Measurements of the velocity field were performed by means of two 5 μm diameter *hot wire probes*, operating in constant temperature mode and with a sampling frequency of 40 kHz; the first was installed in streamwise direction, exposing the wire in the transversal one in order to record the velocity magnitude, while the second was aligned with the rotor axis and rotated of $\pm 45°$ with respect to the transversal direction, so that it could monitor the local flow angle. For both sensors, uncertainty in the velocity measurements resulted about 2% after calibration in a low-speed jet. The pressure field was sampled instead via a *directional pneumatic five hole probe*, which also served as support for the reconstruction of the three-dimensional velocity field. For the purpose, the instrument was calibrated over an angular range of ±24° in all main directions, yielding an uncertainty of 10 Pa for pressure and ±0.2° for flow angles. Full documentation of the measurement system can be found in [4, 17, 48].

Table 2.2: Summary of the different test conditions investigated during the experimental campaign. Each quantity is reported together with the corresponding uncertainty u [4].

U_0 [m/s]	$u_{U_0[95\%]}$ [m/s]	T [°C]	$u_{T[95\%]}$ [°C]	ρ [kg/m^3]	$u_{\rho[95\%]}$ [kg/m^3]	Ω [rpm]	$u_{\Omega[95\%]}$ [rpm]
6.09	0.12	24.95	0.12	1.160	0.0018	398.47	0.05
6.53	0.12	25.90	0.12	1.155	0.0018	400.21	0.05
7.99	0.12	25.03	0.12	1.157	0.0018	400.31	0.06
9.02	0.12	25.76	0.12	1.155	0.0018	400.97	0.05
10.01	0.12	25.03	0.12	1.157	0.0018	401.09	0.06
12.00	0.12	25.03	0.12	1.154	0.0018	400.75	0.05
14.13	0.12	25.03	0.12	1.154	0.0018	400.52	0.05
14.36	0.12	26.90	0.12	1.153	0.0018	401.20	0.05
16.18	0.12	25.03	0.12	1.153	0.0018	400.08	0.09

2.3 Experimental data post-processing

In order to extract synthetic information about turbine performance and wake development, necessary for the characterisation of the machine behaviour and for the successive validation process, the raw data coming from wind tunnel tests was subjected to a dedicated post-processing.

A preliminary step consisted in the estimation of the blockage correction U'_0/U_0, to be applied to the measured freestream velocity U_0. In such perspective, the model proposed by [41] for bluff bodies in open-jet flow was employed:

$$\frac{U'_0}{U_0} = 1 + \varepsilon_S + \varepsilon_N + \varepsilon_C \tag{2.1}$$

where the term ε_S is associated to jet expansion, ε_N to the perturbation induced by the nozzle and ε_C to the presence of the collector downstream of the turbine. The final result is an overall blockage correction of 1.5%, which, being of the same order of magnitude of the uncertainty in the measured freestream velocity, was considered to be negligible [17].

Mechanical torque, shaft bending moment and rotational speed records, with a duration of 3 min. for each operating condition, were ensemble averaged over the rotor azimuthal position, obtaining the corresponding profiles over a revolution; associated measurement errors were computed as category A uncertainties, considering a confidence interval of 95%. This data served then as starting point for the derivation of other quantities of interest, such as aerodynamic torque T, rotor thrust F_X, and extracted power, together with their normalised coefficients:

- Torque coefficient C_T:

$$C_T = \frac{T}{0.5\rho A D U_0^2} \tag{2.2}$$

- Thrust coefficient C_X:

$$C_X = \frac{\bar{F}_X}{0.5\rho A U_0^2} \tag{2.3}$$

- Power coefficient C_P:

$$C_P = \frac{\bar{T}\Omega}{0.5\rho A U_0^3} \tag{2.4}$$

where symbols with the overbar represent quantities arithmetically averaged over the turbine revolution period. The correspond uncertainty was evaluated via error propagation and shows a relevant sensitivity to the tip-speed ratio.

Velocity measurements were instead subjected to a triple decomposition procedure, aimed at separating the time-mean velocity component U_{TM} from the deterministic and unresolved unsteady ones, respectively U_{PER} and U_{TU}:

$$U(t, X, Y, Z) = U_{TM}(X, Y, Z) + U_{PER}(t, X, Y, Z) + U_{TU}(t, X, Y, Z) \tag{2.5}$$

For the purpose, each experimental record was fractioned using as fundamental unit the blade passing period ($BPP=1/(\Omega N_b)$), in turn divided into a certain number of samples N_{PER} basing on the adopted temporal resolution Δt. In such context, the time-mean velocity component U_{TM} was computed as standard arithmetic average over the whole sampling time:

$$U_{TM}(X, Y, Z) = \frac{1}{N_{BPP} \cdot N_{PER}} \sum_{i=1}^{N_{BPP}} \sum_{j=1}^{N_{PER}} U(i, j, X, Y, Z) \tag{2.6}$$

The phase-resolved component U_{PER} on the other hand, related to the periodic unsteadiness promoted by the motion of the blades, was evaluated by ensemble averaging among values acquired at the same phase j, i.e. azimuthal position of the rotor, for all the different BPPs available and then subtracting the time-mean component:

$$U_{PER}(j, X, Y, Z) = \frac{1}{N_{BPP}} \sum_{i=1}^{N_{BPP}} [U(i, j, X, Y, Z) - U_{TM}(X, Y, Z)] \tag{2.7}$$

Fundamental for such operation was the synchronisation of velocity measurements with the blade motion (phase-locking), carried out exploiting the absolute encoder mounted on the rotor as key-phasor. The information about periodic unsteadiness was further synthesised by evaluating the RMS average of U_{PER} and normalising it over the freestream velocity:

$$I_{PER}(X, Y, Z) = \frac{1}{U_0} \sqrt{\frac{\sum_{j=1}^{N_{PER}} [U_{PER}(j, X, Y, Z)]^2}{N_{PER}}} \tag{2.8}$$

The decomposition process was eventually completed by the assessment of the unresolved/turbulent unsteady velocity component $\mathrm{U_{TU}}$, obtained by subtracting the other two components from the original signal:

$$U_{TU}(t,X,Y,Z) = U(t,X,Y,Z) - U_{TM}(X,Y,Z) - U_{PER}(t,X,Y,Z) \tag{2.9}$$

The latter served then as starting point for the derivation of the periodic phase-resolved streamwise turbulent intensity $\mathrm{I_{TU,PER}}$:

$$I_{TU,PER}(j,X,Y,Z) = \frac{1}{U_0}\sqrt{\frac{\sum_{i=1}^{N_{BPP}} \left[U_{TU}(i,j,X,Y,Z)\right]^2}{N_{BPP}}} \tag{2.10}$$

which was further reduced to the streamwise turbulence intensity $\mathrm{I_{TU}}$ by RMS averaging it over the blade passing period, so that a global index of the turbulence strength in a determined location of the wake could be achieved:

$$I_{TU}(X,Y,Z) = \sqrt{\frac{\sum_{j=1}^{N_{PER}} \left[I_{TU,PER}(j,X,Y,Z)\right]^2}{N_{PER}}} \tag{2.11}$$

Full documentation of the adopted post-processing techniques can be found in [48].

Chapter 3

CFD Model

In this chapter, the methodology followed for the construction of the numerical model of the turbine is presented. More in detail, the ACL method and its integration in OpenFOAM, together with the applied sub-models, are described in section 3.1, while the implementation of the FV discretisation of the flow domain is thoroughly reported in sections 3.2, 3.3, 3.4 and 3.5.

3.1 Actuator Line Method (ACL)

The Actuactor Line Method (ACL) is a hybrid approach developed by Shen and Sørensen [53], which combines a BEM-based modelling of the turbine with the FV discretisation of the flow domain (see section 1.3); in particular, each blade is replaced by a dynamically equivalent actuator line, introducing aerodynamic forces into the computational grid basing on its current position and local flow conditions.

This method is able to provide a relatively accurate and complete description of the unsteady, three-dimensional flow field developing around Darrieus rotors, in particular of the wake shed by the machine, at reduced implementation effort and elaboration time with respect to a fully resolved CFD simulation; in fact, being based on blade-element theory, it does not require the resolution of the boundary layer encompassing the blade surfaces, with a corresponding strong decrease in the required computational cost [51]. The absence of the boundary layer also represents a major advantage in the implementation of LES turbulence models, that notoriously suffer from issues in the treatment of the near-wall region [58]. These characteristics, combined with the virtually unlimited variety of flows manageable by CFD, make it the most promising tool for the simulation of VAWTs in complex and turbulent environments, such as high-density built areas.

Its main drawback, inherited from BEM, is the elevated sensitivity of the solution to input aerodynamic data and employed sub-models, which thus demand extreme care in their derivation and implementation. For the same reason, the ACL usually requires a large experimental and numerical validation effort, before it can be used in a reliable way.

3.1.1 Algorithm

In the general ACL formulation, each blade is replaced by an rotating actuator line, whose law of motion is defined in equation 3.1:

$$\vartheta = \Omega t + \frac{2\pi}{3}(i-1) \quad \text{for i=1:3} \tag{3.1}$$

where ϑ is the blade angular position, Ω is the turbine rotational speed, i the blade number. At the generic timestep, the grid cells encompassing the blade line are identified basing on its current position and used to discretise the blade into N independent elements, assumed to behave aerodynamically as a two-dimensional airfoil. For each of these elements, the undisturbed flow velocity $\mathbf{v}_\mathrm{l}$ is extracted from local flow field by means of an ad hoc algorithm (EVM), which will be described in section 3.1.2, and combined with the blade peripheral velocity $\mathbf{v}_\mathrm{tr} = \boldsymbol{\Omega} R$ to obtain the relative velocity vector $\mathbf{v}_\mathrm{r}$, according to equation 3.2. For the purpose, directions normal $\mathbf{n}$ and tangential $\mathbf{t}$ with respect to the vector connecting the turbine axis with the blade-support arm attachment point are considered:

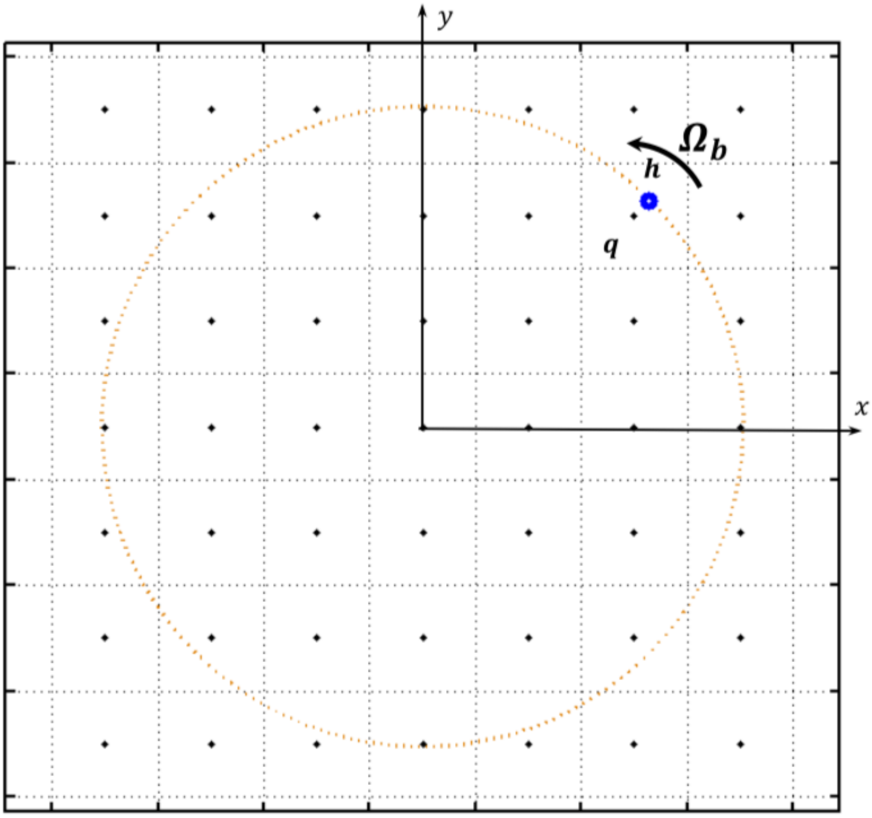

Figure 3.1: Cross-sectional view of the actuator line, identified by the blue dot, in the computational mesh. The cell size is here exaggerated for illustration reasons [51].

$$\boldsymbol{v_r} = \boldsymbol{v_l} - \boldsymbol{v_{tr}} = (v_{l,t} - \Omega R)\boldsymbol{t} + v_{l,n}\boldsymbol{n} \tag{3.2}$$

The magnitude $\mathrm{v_r}$ and angle φ of the relative velocity vector with respect to tangential direction can be then easily derived and used to evaluate the blade angle

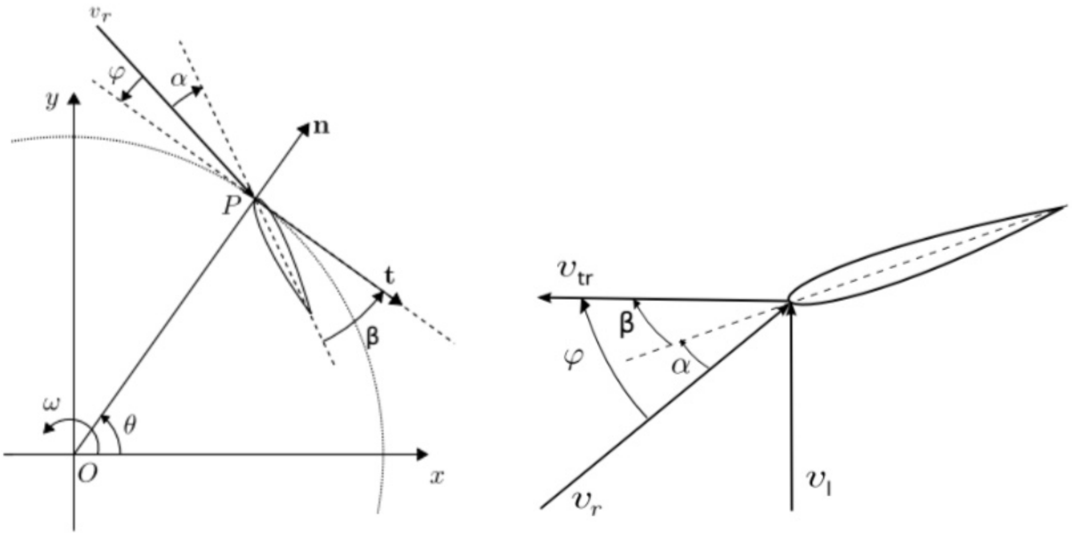

(a) Absolute frame of reference **(b)** Relative frame of reference

Figure 3.2: Frames of reference adopted for the description of the interaction bewteen the wind and the rotating blade [14].

of attack α and the chord-based Reynolds Number Re, required to extract the corresponding lift and drag coefficients $\mathrm{C_L}$, $\mathrm{C_D}$ from available tabulated data:

$$v_r = |\boldsymbol{v_r}| \quad \rightarrow \quad \alpha = \varphi - \beta \tag{3.3}$$

$$\varphi = \angle \boldsymbol{v_r} \quad \rightarrow \quad Re = \frac{v_r c}{\nu} \tag{3.4}$$

where β, c are respectively the blade pitch angle and chord, while $\nu = \mu/\rho$ is the air kinematic viscosity. Eventually, aerodynamic forces associated to each blade element/intersected grid cell are calculated according to their standard definition:

$$\mathbf{L} = \frac{1}{2}\rho v_r^2 C_L(\alpha, Re) c h_{cell} \cdot \boldsymbol{l} \tag{3.5}$$

$$\mathbf{D} = \frac{1}{2}\rho v_r^2 C_D(\alpha, Re) c h_{cell} \cdot \boldsymbol{d} \tag{3.6}$$

with **l**, **d** unit vectors indicating the lift and drag directions, while $\mathrm{h_{cell}}$ is the extension of considered cell along the actuator line. As final step, the effect of wind-turbine interaction on the flow is modelled by inserting new-found integral forces into the selected cell as volume source terms, directly modifying the discretised incompressible NS momentum equation (see section 1.3.3) with a corresponding body force **f**:

$$\mathbf{f} = \frac{\mathbf{L} + \mathbf{D}}{V_{cell}} \quad \rightarrow \quad \frac{\partial(\rho \boldsymbol{U})}{\partial t} + \nabla \cdot (\rho \boldsymbol{U} \otimes \boldsymbol{U}) - \nabla \cdot (\mu \nabla \boldsymbol{U}) + \mathbf{f} = -\nabla P \tag{3.7}$$

From there, the velocity field is resolved via a proper FV solution algorithm, e.g. PISO, and then used as input for the following timestep.

3.1.2 Numerical implementation - DarrieusSolver

The actuator line method was implemented in OpenFOAM 2.3.x by M. Caglioni in its master thesis [14], by integrating the transient incompressible solver *pisoFoam* with the algorithm described in section 3.1.1 and various auxiliary subroutines, e.g. EVM and RK. The final result is the *DarrieusSolver* solver employed for this thesis.

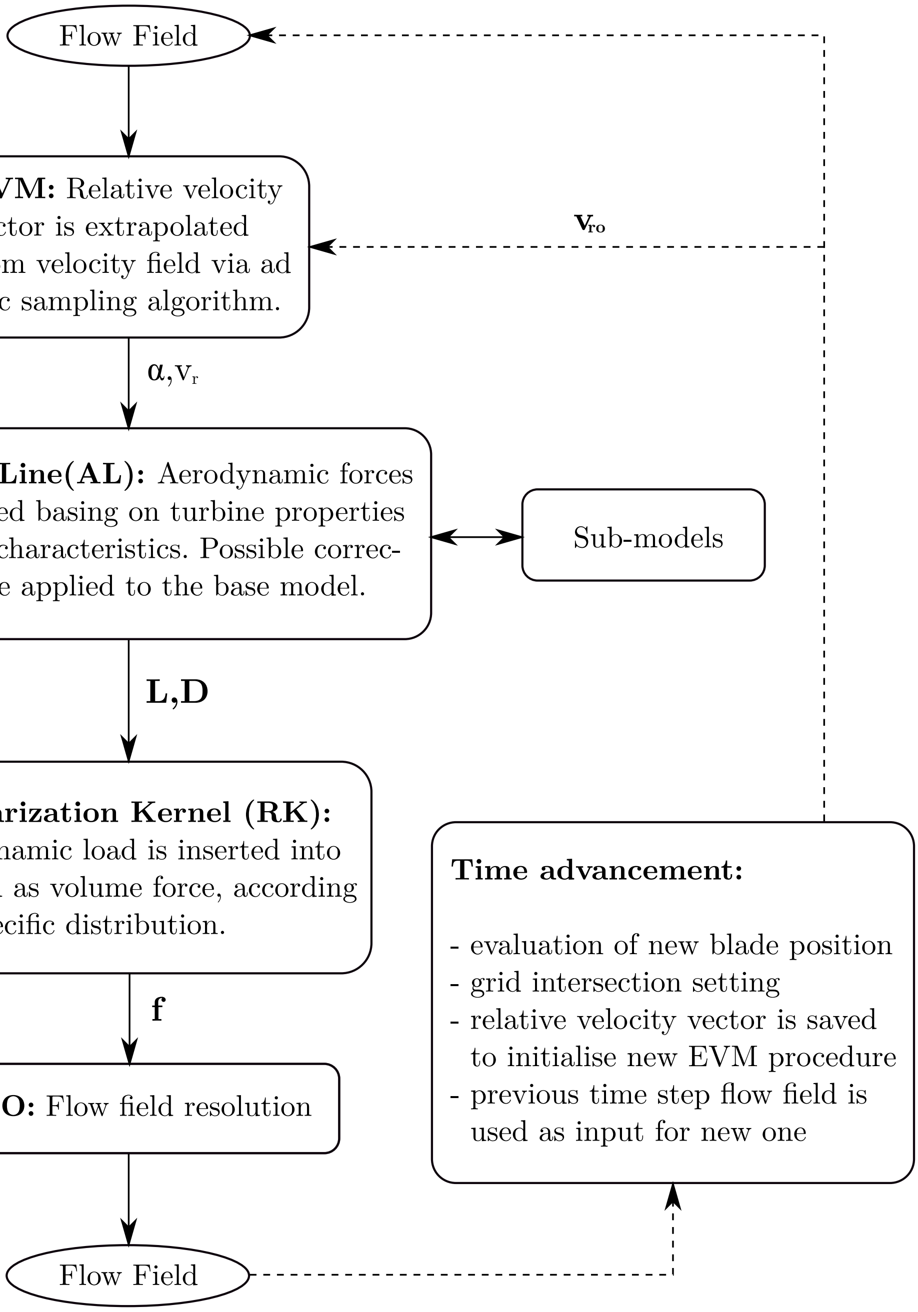

Figure 3.3: Series of operations performed by the solver on the single blade element.

The code takes as input the tabulated polar data required for the computation of aerodynamic forces, and two dictionaries, *turbineProperties* and *actuactorForceParam*:

- *turbineProperties* gathers the structural and operative characteristics of the machine (number of blades, hub position, rotational speed, etc . . .). It also contains detailed information about the blade geometry, defined by spanwise distributions of selected parameters, e.g. chord length, pitch angle, airfoil type, etc . . . ; this allows elevated modularity and flexibility of the code in the simulation of various turbine configurations, possibly including arbitrary pitch histories.
- *actuactorForceParam* contains instead all the information required to set-up solver operation. The latter includes the settings of the EVM, the RK and the various sub-models available.

Once all the required data has been gathered, the resolution process occurs for each of the blade-elements/grid cells in which turbine blades have been discretised, according to the diagram in figure 3.3. It can be noted how there is also the possibility to implement user-defined sub-models directly into the ACL algorithm, in order to raise the overall prediction capability; such feature was used extensively in the development of the present work, as thoroughly described in sections 3.1.4, 3.1.5 and 3.1.6. Eventually, integral blade forces are assembled together from single contributions, and used to evaluate the global performances parameters of the turbine (streamwise thrust, torque, power); these are yielded as output in the *thrustTorquePower* file, together with extensive report of single blade loading history ("blade*" files).

As anticipated, different sub-algorithms are used in the code:

EVM In the frame of ACL methods, one of the core issues is the extraction of the undisturbed velocity vector $\mathbf{v}_1$ from the resolved flow field, to be used for the computation of aerodynamic forces. Among the many approaches which have been proposed, two in particular have found application in research or commercial codes: the *undisturbed* and *local* velocity evaluation methods [7].

The first, commonly employed in structural solvers, assumes the undisturbed velocity to be equal to the freestream wind one at the rotor plane under consideration; as a consequence, both implementation effort and accuracy are strongly reduced, not accounting for local wind-blade interaction phenomena (induction, turbulent fluctuations, aeroelastic forcing, etc. . .).

A noteworthy improvement is introduced by the second one, whose formulation is based on the hypothesis that the velocity vector sampled in the force application point is equal to the undisturbed one; in fact, according to both Kutta-Joukowsky and Biot-Savart theories, in that particular location the effect of bound-vortex induction is null. In spite of its higher accuracy in the local interaction description, this method presents relevant flaws from both a theoretical and numerical point of view: on one hand, underlying assumptions derive from potential flow theory, hardly extendable to the viscid, unsteady flow characterising the turbine blade operation. On the other hand, the upwash/downwash phenomena related to the airfoil bound vorticity are responsible for strong velocity angle gradients at the local level, making the simulation results extremely sensitive to the position of the sampling point and so jeopardizing the code robustness [7].

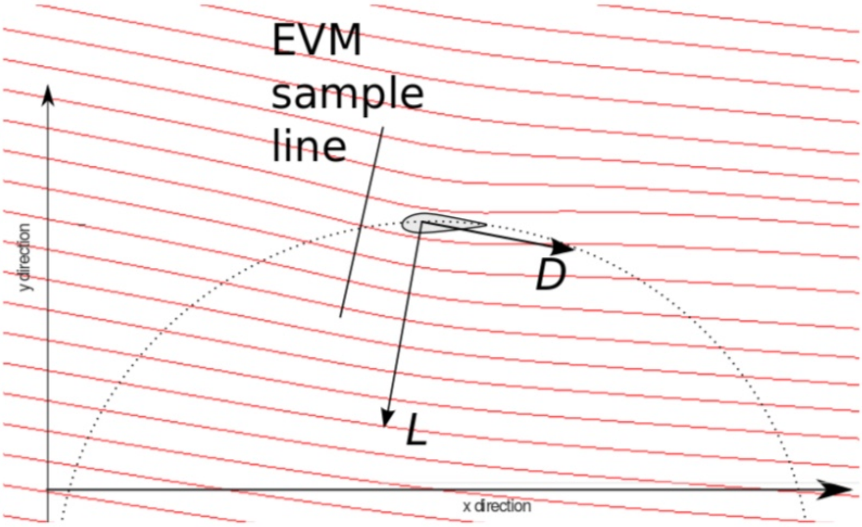

Figure 3.4: Schematic of the positioning of the EVM sampling line with respect to the airfoil and the incoming flow [14].

In order to combine the robustness of the *undisturbed* and the accuracy of the *local* approaches, Schito [49] introduced the Effective Velocity Model (EVM), which exploits a sampling line to probe the velocity field at an arbitrary distance upstream of the airfoil under consideration; this velocity profile is then spatially averaged to obtain the mean $\mathbf{v}_l$ magnitude and direction. As it can be easily inferred, overall performance is strongly dependent on the sampling system configuration, which has to be carefully tuned for the method to provide reliable results. This work was done in their master thesis by Bernini and Caccialanza [7], who identified, after an extensive simulation campaign, the three main parameters affecting the sampling system efficiency and their optimum values:

- **Position:** the sampling line optimal distance from the airfoil, i.e. the actuator line, was derived from a comparison between ACL and fully resolved CFD simulations of a test airfoil, at fixed freestream conditions. Basing on obtained results, a value of 1.5 h_{cell}, with h_{cell} characteristic cell dimension, was chosen as the one minimizing the evaluation error on both velocity magnitude and direction, still allowing the sampling line to be sufficiently close to the profile for local effects to be taken into account.

- **Length:** the sampling line length was optimized following the same approach adopted for its positioning, focusing this time on the angular deviation of the probed flow from the imposed undisturbed one; as a matter of fact, the lift-related bound vorticity around the airfoil deflects the incoming flow from its original direction, introducing an error in the velocity data acquisition phase. Optimal length was found to be 5 h_{cell}.

- **Direction:** the sampling line direction was chosen to be orthogonal to the relative velocity one, so that spurious contributions from blade translational motion could be avoided. If this strategy was not problematic in the study of

> Bernini and Caccialanza, since HAWTs have a relatively steady operation, it became a serious issue in the adaptation of the code to VAWTs operated by Caglioni [14]; for those machines in fact, the blade relative velocity direction changes continuously over time, especially in the downwind section, where it is enhanced by the blade-wake interaction phenomenon. Solution to the problem was the initialisation, under the hypothesis of sufficient temporal resolution of the simulation, of the EVM procedure with the relative velocity direction $\mathbf{v}_{\mathrm{r,o}}$ coming from the previous timestep, as shown in figure 3.3.

Although minimised in the optimisation phase, the error introduced by the EVM in the reference velocity evaluation was still too high for the method to be considered accurate. Consequently, the calibration process was completed with the construction of a semi-empirical model, quantifying the effect of distortion induced by the wind-blade interaction on the undisturbed flow at the selected sampling position, i.e. 1.5 $\mathrm{h_{cell}}$. Testing strategy was the same adopted for the algorithm optimisation. From the tests, the following set of corrections was derived:

$$\begin{cases} v_l = v_{EVM}; \\ \Delta\alpha = \alpha_{EVM} - \alpha = \frac{c}{h_{cell}} \cdot (1.2553 - 0.0552 C_D) C_L; \end{cases} \tag{3.8}$$

As evident from equation 3.8, while the undisturbed velocity module $\mathrm{v_l}$ remains essentially unaffected, the angle of attack α is subjected to a certain deflection $\Delta\alpha$, increasing with the intensity of the bound vorticity around the airfoil and so with the lift coefficient. Final result of development and calibration process is the EVM subroutine employed in the *DarrieusSolver*.

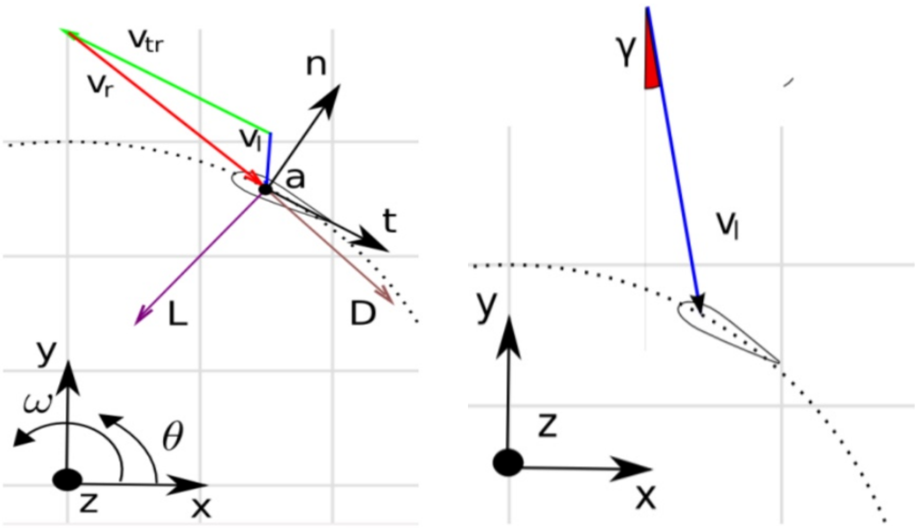

(a) Absolute and blade-relative reference systems

(b) Absolute reference system

Figure 3.5: Frames of reference employed by the solver for blade relative velocity and aerodynamic force evaluation [14].

The coded version of the algorithm in particular exploits two reference systems (see figure 3.5), an absolute Cartesian one, in which $\mathbf{v}_\mathrm{l}$ is evaluated, and a mobile blade-related one, in which $\mathbf{v}_\mathrm{l}$ is expressed in normal and tangential components to be later combined with $\mathbf{v}_\mathrm{tr}$, obtaining $\mathbf{v}_\mathrm{r}$ (see equation 3.2). The two are linked by an ad hoc transformation matrix.

Regularization Kernel A issue, which has characterized the ACL method from the start [53], is the proper way of introducing the aerodynamic forces into the computational domain; as a matter of fact, when directly applied as concentrated volume sources into the corresponding grid cell (see section 3.1.1), they induce strong velocity gradients in the interacting flow, provoking relevant numerical oscillations and undermining the stability of the simulation.

One of the main strategies against this problem is the employment of a specific smearing function, which redistributes the aerodynamic load of the cell under consideration over the neighbouring ones. This way, the robustness of the code is strongly enhanced at the cost of a reasonably small accuracy reduction. In the present work, basing on the study of Bernini and Caccialanza [7], who implemented and optimized it, a two-dimensional Regularization Kernel (RK) was adopted, spreading the computed volume forces over the domain according to the following Gaussian distribution:

$$\eta_{RK}^{2D}(d) = \frac{1}{\sqrt{\varepsilon^4 (2\pi)^2}} \exp\left[-\left(\frac{1}{2}\frac{d^2}{\varepsilon^2}\right)\right] \tag{3.9}$$

where d is the distance from force application point and ε is the RK width parameter, which was set to 1 $\mathrm{h_{cell}}$ to minimize the spurious spatial oscillations described so far. The volume force field is derived from actuator line force convolution with equation 3.9, as shown in figure 3.6b:

$$\mathbf{f}(\mathbf{x}) = \sum_i \mathbf{f}_i \cdot \eta_{RK}^{2D}(|\mathbf{x} - \mathbf{x}^i|) \tag{3.10}$$

with i index of actuator line cell.

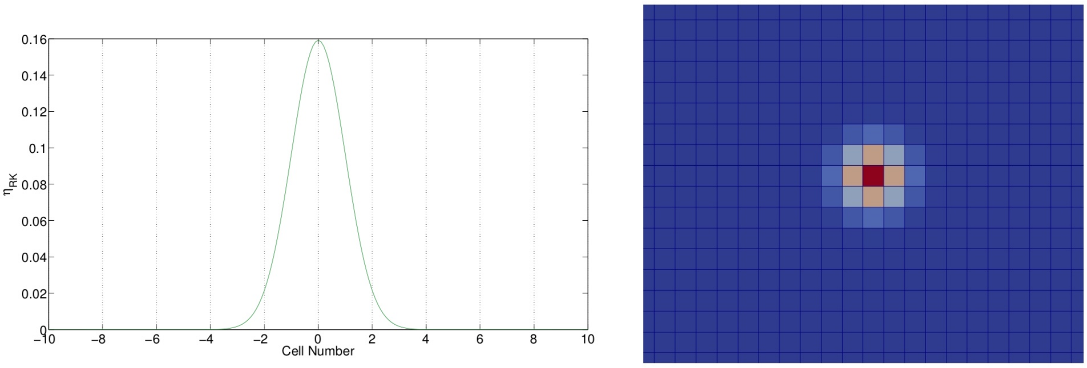

(a) (b)

Figure 3.6: Regularization Kernel function and the corresponding volume force field in the computational grid [7].

PISO The PISO (Pressure-Implicit with Splitting of Operators) algorithm was proposed by Issa in 1986 [26], initially developed for unsteady compressible flows and then adapted to other problem configurations. The PISO sequence of operations is built on the hypothesis that, for a sufficiently small timestep (Co ≤ 1), the non-linear coupling given by the momentum convection term becomes negligible with respect to the pressure-velocity one, allowing to linearise the momentum equation; consequently, the structural coefficients of the latter are assumed to be constant over a single timestep [28]. Such strategy provides a fast and efficient solution scheme for highly unsteady cases (LES, VAWT, etc..), where high temporal resolution is required.

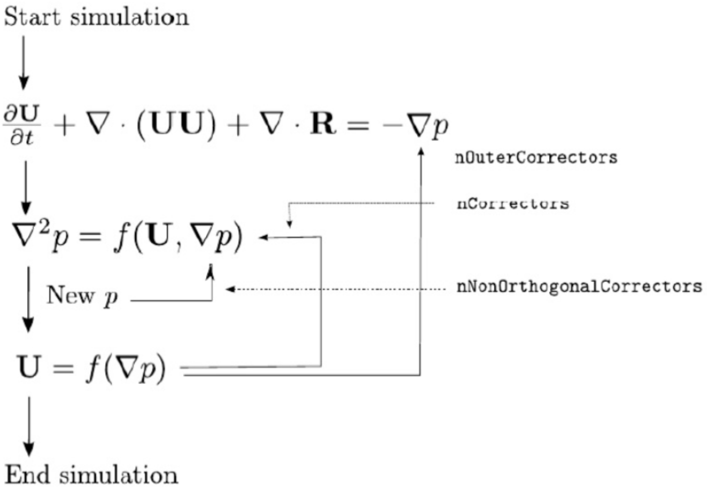

Figure 3.7: Schematic of the PISO algorithm.

According to figure 3.7, the solution loop consists substantially of three steps:

1. An implicit *momentum predictor*, which, starting from previous time step fields $\mathbf{U}_\mathrm{o}$, P_o, evaluates the velocity field required to initialise the pressure-velocity coupling, according to the discretised momentum equation in matrix form (see section 1.3.3):

$$a_P(\boldsymbol{U_o})\boldsymbol{U_P} = \boldsymbol{H}(\boldsymbol{U_o}) - \nabla P_o \tag{3.11}$$

where a_P contains the coefficients of the momentum equation with respect to the velocity field $\mathbf{U}_\mathrm{P}$, while $\boldsymbol{H}(\boldsymbol{U}) = -\sum a_N(\boldsymbol{U_o})\boldsymbol{U_N} + \boldsymbol{U_o}/\Delta t$ is a structural matrix gathering the contributes of neighbouring cells convective transport and temporal source term (other sources are here neglected).

2. An implicit *pressure solution*, which corrects the pressure field basing on the combination of discretised momentum and continuity equations, after $\mathbf{H}(\mathbf{U})$ has been updated with the new velocity field:

$$\nabla \cdot [a_P^{-1}\nabla P] = \nabla \cdot [a_P^{-1}\boldsymbol{H}(\boldsymbol{U})] \tag{3.12}$$

3. An explicit *velocity correction* with the pressure field coming from step 2:

$$\boldsymbol{U_P} = a_P^{-1}\boldsymbol{H}(\boldsymbol{U}) - a_p^{-1}\nabla P \tag{3.13}$$

> It must be noted how in this phase, the velocity correction is based only on pressure, since $\mathbf{H}(\mathbf{U})$ is not updated.

Due to the explicit nature of the velocity correction, an error is introduced in the U-P system, so that *nCorrectors* loops, in which steps 2-3 are repeated with $\mathbf{H}(\mathbf{U})$ update at each iteration, are used. Typically, three loops are employed; the first two are run with a relatively high tolerance to quickly achieve a conservative velocity and pressure fields, which are then exploited to initialise the final one. It is worth noticing that, due to the PISO linearised formulation and the presence of the $\mathbf{H}(\mathbf{U})$ correction, under-relaxation is not required.

3.1.3 Polar data

As in every BEM-based method, ACL overall accuracy is extremely sensitive to input aerodynamic data, whose collection and validation thus represents a fundamental step for the implementation of such approach. In the frame of VAWTs, this task becomes extremely challenging due to their working principle. As a matter of fact, during a revolution the single turbine blade experiences large oscillations of the angle of attack, with increasing amplitude going towards the lower TSRs; at start-up such range can extend up to [-180°,180°]. As a consequence, polar data must cover not only the attached flow region, as in most aerodynamic problems, but also the post- and deep stall ones, where it is notoriously difficult to obtain accurate results, both experimentally and numerically. The situation is made even more complex by the simultaneous fluctuation of the blade relative velocity magnitude $\mathrm{v_r}$, and so of the local Reynolds number:

$$Re = \frac{v_r c}{\nu} \tag{3.14}$$

where c is the blade chord and $\nu = \mu/\rho$ the kinematic viscosity of air; correspondingly, a great variety of characteristic curves is encountered. This issue is particularly severe for small VAWTs as the one under study, where the variation of curve parameters (static stall angle, linear region slope, etc . . .) is enhanced by the oscillation of the flow regime in the laminar-to-turbulent transition region.

Owing to these difficulties, combined to the fact that the interest for these machines has been renewed only recently, data available in literature is restricted to a few papers, among which the one of Sheldahl and Klimas [52] stands out; in this study, polar data for the seven symmetrical airfoils commonly mounted on VAWTs (NACA0009 - 0021) was derived from an extensive experimental campaign, considering $\alpha \in [-180°, 180°]$ and Re $\in [10^4, 10^7]$. According to various authors [10] however, data for thicker profiles (NACA0018 - 0025) and for low Re are not reliable, being extrapolated via ad hoc synthesizer code from experimental data for thinner profiles (NACA0009 - 0015) in the high Re region. Discrepancy with more recent studies is particularly evident in the attached flow region, where the influence of airfoil maximum thickness is the highest.

For this reason, it was chosen to build the necessary aerodynamic curves from scratch, by combining various numerical and semi-empirical methods. Formulation of adopted approach strongly varies from one flow region to another, according to the different regulating phenomena involved:

Attached flow region In the pre-stall region, the flow remains attached to the profile up to its trailing edge, resulting in high aerodynamic efficiency $E = C_L/C_D$ and a quasi-linear trend of the lift coefficient with the angle of attack (see fig. 3.8). As non-linear phenomena remain confined in the boundary layer, whose extension, except for very low Re, is limited to a thin region in proximity of the airfoil surface, it is possible to obtain a reliable estimation of the lift and drag coefficients with a linear method, possibly embedding ad hoc sub-models for the prediction of the viscous region development.

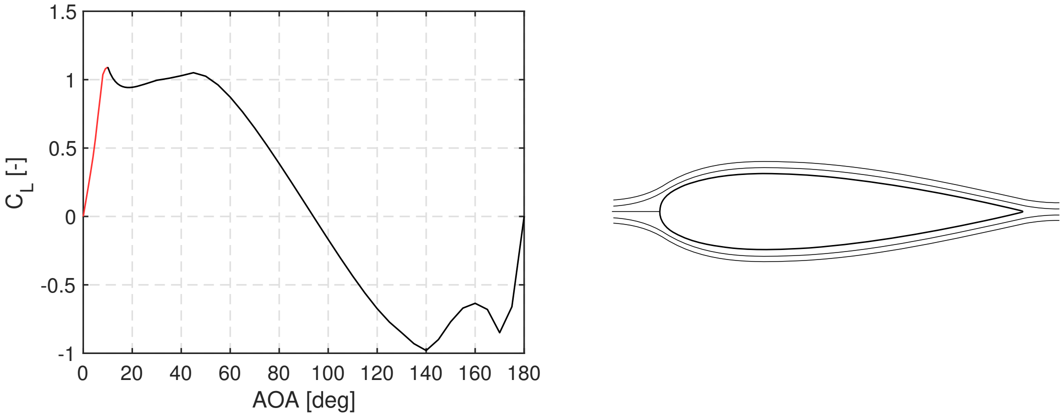

(a) Branch of the lift characteristic curve (red) **(b)** Schematic of the flow around the airfoil

Figure 3.8: Overview of main flow features in the pre-stall region.

In the present work, the XFlr5 application, based on the popular XFoil code [19, 20], was employed. This algorithm is based on a two-zones schematization of the main flow, which is divided in a freestream region, essentially inviscid, and a near-wall one, or boundary layer, dominated by viscous effects; the former is modelled by means of a linear vorticity panel method with a Karman-Tsien compressibility correction, while a two-equations lagged dissipation integral approach is used for the latter. The two are coupled by proper source terms, and discretised via subdivision of the airfoil and its wake in N panels, so that the whole problem can be handled in an algebraic way. A e^9-type free transition model is also available in the code, in order to properly capture the effects of turbulent transition and separation bubbles. Further details can be found in appendix A.

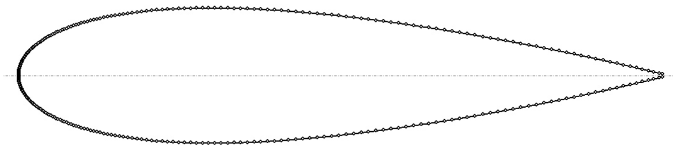

Simulation Set-Up	
N	300
N_{crit}	9
Re range [-]	[40e3, 5e6]
α range [deg]	[-20°,20°]

Figure 3.9: Settings of NACA0021 simulation. From left to right: discretisation of the test airfoil, input data to the code.

Discretisation of the adopted NACA0021 profile, together with simulation set-up, is reported in figure 3.9. 300 panels were distributed along the airfoil surface in a non-homogeneous way, increasing resolution in the critical regions such as the leading and trailing edge, in order to raise the overall computational efficiency. For the N_{crit} threshold parameter required by the e^9-type transition model instead, a value of 9 was chosen, according to the surface roughness and turbulence intensity levels commonly found in wind tunnel tests.

Post-stall region In the post-stall region, thicker airfoils as the NACA0021 are characterised by a progressive transition of the separation point from the trailing to the leading edge of the profile, as illustrated in figure 3.10b.

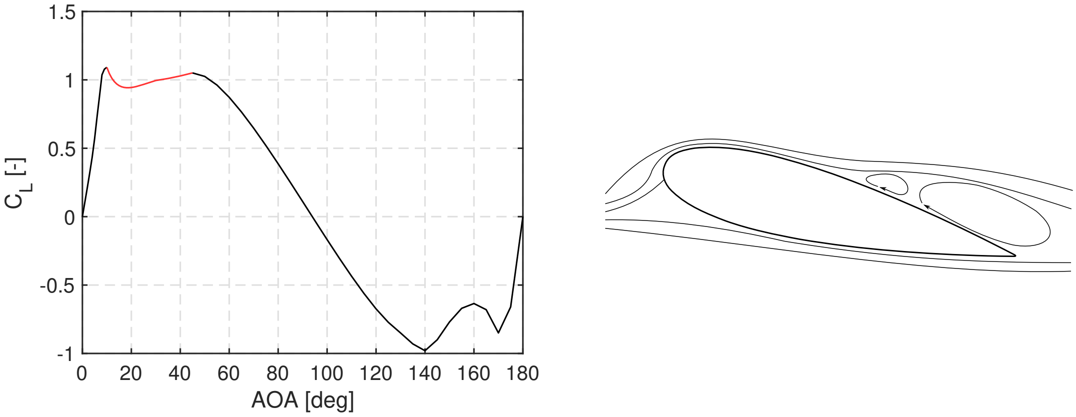

(a) Branch of the lift characteristic curve (red) **(b)** Schematic of the flow around the airfoil

Figure 3.10: Overview of main flow features in the post-stall region.

In static conditions, the full development of the separated zone leads to a sharp reduction in lift and a corresponding increase in drag, as observed in most wind tunnel test data. In dynamic conditions as the ones experienced by VAWT blades however, the continuous variation of angle of attack does not give flow separation enough time to complete, preventing the corresponding discontinuity in the aerodynamic curves to occur [34]; in order to account for this phenomenon, the ubiquitous Viterna-Corrigan extrapolation method [59] was employed to obtain a smooth transition in the aerodynamic data from the attached to the deep stall flow regions. As demonstrated by Bianchini et al. [34], this approach increases not only the robustness of the simulation, but also the accuracy of the results both with and without the presence of a dynamic stall model.

The Viterna-Corrigan method is a semi-empirical approach, which exploits a corrected flat-plate model of the airfoil behaviour to extrapolate aerodynamic data beyond the static stall point α_{SS}. In its basic formulation, the lift and drag coefficients are computed as:

$$C_L = A_1 \sin(2\alpha) + A_2 \frac{\cos^2(\alpha)}{\sin(\alpha)} \qquad (15^\circ \leq \alpha \leq 90^\circ) \tag{3.15}$$

$$C_D = B_1 \sin^2(\alpha) + B_2 \cos(\alpha) \qquad (15^\circ \leq \alpha \leq 90^\circ) \tag{3.16}$$

where A_1, B_1, A_2 and B_2 are semi-empirical coefficients depending on the properties of the static stall point α_{SS} and the maximum drag coefficient $C_{D_{max}}$, i.e. $C_{D_{90}}$:

$$A_1 = B_1/2 \tag{3.17}$$

$$B_1 = C_{D_{max}} \tag{3.18}$$

$$A_2 = (C_L(\alpha_{SS}) - C_{D_{max}} \sin(\alpha_{SS}) \cos(\alpha_{SS})) \frac{\sin(\alpha_{SS})}{\cos^2(\alpha_{SS})} \tag{3.19}$$

$$B_2 = \frac{C_D(\alpha_{SS}) - C_{D_{max}} \sin^2(\alpha_{SS})}{\cos(\alpha_{SS})} \tag{3.20}$$

For details about $C_{D_{max}}$ evaluation, see equation 3.27. It must be noted how the adoption of this method represents nonetheless an approximation, not only because the employed profile is too thick to fall under the flat plate assumption, but also due to the elevated degree of uncertainty associated to α_{SS} evaluation; in absence of experimental data in fact, a correct assessment of such parameter would require the analysis via proper criteria of the boundary layer development over time, which depends on multiple characteristics of the airfoil (geometry, surface roughness, aspect ratio, etc ...) and of the flow, e.g Re [15].

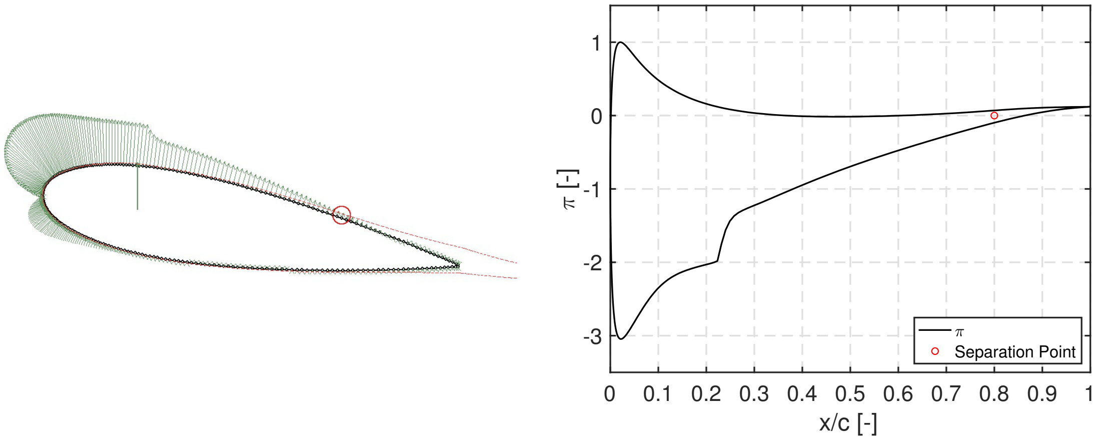

(a) Pressure and boundary layer thickness **(b)** Pressure coefficient

Figure 3.11: Identification of the flow separation point (red dot) via the boundary layer thickness and pressure coefficient π chordwise distributions given in output by XFoil.

In this case instead, the separation point was identified basing on the chordwise pressure coefficient π distribution (see eq. 3.21) and boundary layer thickness profile given in output by XFoil; in that specific location, the former shows a transition to a nearly flat profile, while the latter experiences a steep increase, diverging from the airfoil surface. An example of such procedure is shown in figure 3.11.

$$\pi = \frac{P - P_0}{0.5\rho U_0^2} \tag{3.21}$$

Deep stall region As the separation point reaches the leading edge, the flow becomes fully separated, completing the transition from a lift- to a drag-based wind-blade interaction, as clearly visible in figure 3.12b. In such condition, the Pressure Side (PS) of the airfoil is characterized by a fully laminar flow, while the Suction Side (SS) by a large recirculation zone; due to this flow configuration, exchanged forces become substantially independent from both flow regime and blade geometry, allowing the formulation of universal semi-empirical laws.

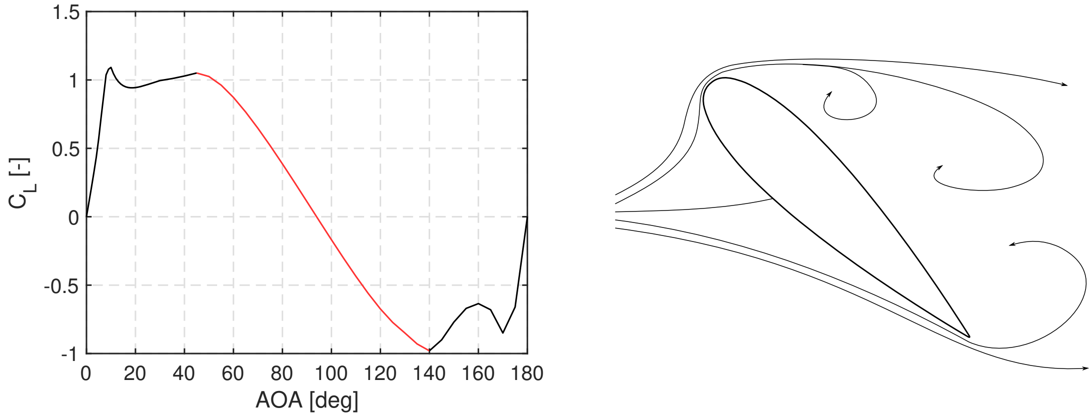

(a) Branch of the lift characteristic curve (red) **(b)** Schematic of the flow around the airfoil

Figure 3.12: Overview of main flow features in the deep stall region.

In this context, the main governing parameter is the airfoil leading edge thickness, which regulates the divergence of separated streamlines from the profile and so the lift and drag forces magnitude. In order to account for this feature in the aerodynamic data extrapolation, the semi-empirical correlation from Battisti [2] was employed; starting from flat plate theory and the work of Lindeburg [33], they proposed and experimentally validated a new set of equations, which could embed the effects of airfoil maximum thickness t/c and Re on the blade deep stall behaviour:

$$C_N = C_{D_{90}} \frac{\sin(\alpha^*) + 0.019\sin(2\alpha^*)}{0.382 + 0.618|\sin(\alpha^*)| + 3.82\frac{t}{c}\cos^8(\alpha^*)} \tag{3.22}$$

$$C_T = 0.29 C_{D_{90}} \frac{t}{c} |\sin(\alpha^*)| (1 - 1.9\cos(\alpha^*)) - C_{D_f}\cos(\alpha^*) \tag{3.23}$$

$$C_L = C_N \cos(\alpha) + C_T \sin(\alpha) \tag{3.24}$$

$$C_D = C_N \sin(\alpha) - C_T \cos(\alpha) \tag{3.25}$$

where $\alpha^* = \alpha - \alpha_0 \cos(\alpha)$ is a modified angle of attack accounting for possible airfoil camber ($\alpha_0 : \mathrm{C_L}(\alpha_0) = 0$), while $\mathrm{C_{D_f}}$ is a friction coefficient which depends on the blade Reynolds number Re:

$$C_{D_f} = \frac{0.43}{\log^{2.56}(Re) - 1742/Re} \tag{3.26}$$

The maximum drag coefficient $\mathrm{C_{D_{max}}}$, i.e. $\mathrm{C_{D_{90}}}$, required by equations 3.22 and 3.23 was computed via the empirical law from Timmer [56]:

$$C_{D_{max}} = 1.994 - 5.4375\frac{y}{c} \tag{3.27}$$

where y/c is the leading edge upwind thickness, evaluated from airfoil profile coordinates (y/c at x/c=0.0125).

Reversed flow region Approaching α=180°, the flow progressively reattaches to the airfoil, but the positions of leading and trailing edges are now reversed, as clearly visible in figure 3.13b, resulting in lower aerodynamic performances with respect to normal pre-stall operation.

This condition occurs in VAWTs only during the start-up phase, so that it is not of interest for the current analysis; for this reason, data from Sheldahl and Klimas [52] were employed in this region.

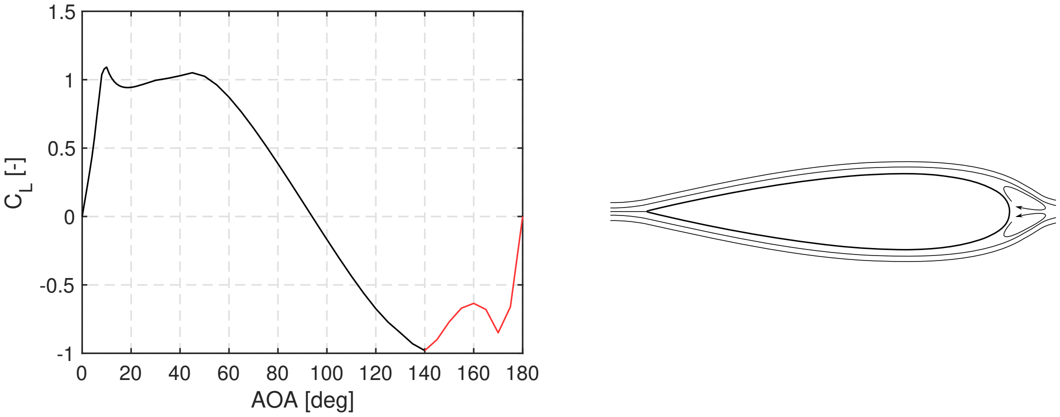

(a) Branch of the lift characteristic curve (red) **(b)** Schematic of the flow around the airfoil

Figure 3.13: Overview of main flow features in the reverse flow region.

3.1.4 Flow curvature correction

One of the core assumptions at the base of BEM-based methods such as the ACL, is that blade average relative velocity and angle of attack, necessary for aerodynamic force evaluation, can be defined from the local values at a reference location on the blade itself, usually identified with the blade-support arm attachment point.

Such hypothesis represents nonetheless an approximation, since, from a physical point of view, the finite extension of the blade implies a variation of the translation velocity along its chord and as a consequence, a non-homogeneous distribution of both relative velocity and angle of attack. In particular, while variation of the former remains fairly limited, the latter experiences a strong gradient between the leading and the trailing edge, as shown in figure 3.14 introducing a relevant distortion in the aerodynamic forces exchange with respect to the non-rotating case [44]. Such deviation is maximum as the static stall limit is exceeded in one of the blade points, boosting the lack of symmetry of the process and enhancing its non-linearity.

A first description of the phenomenon was proposed by Migliore [44], who approached the issue from a theoretical point of view by means of non-dimensional analysis of the blade kinematics. Although simplified with respect to real VAWT operation, this model not only furnishes an exhaustive qualitative description of the flow curvature effect, allowing to identify its main governing parameters, but also offers an effective methodology for embedding it in most simulation algorithms.

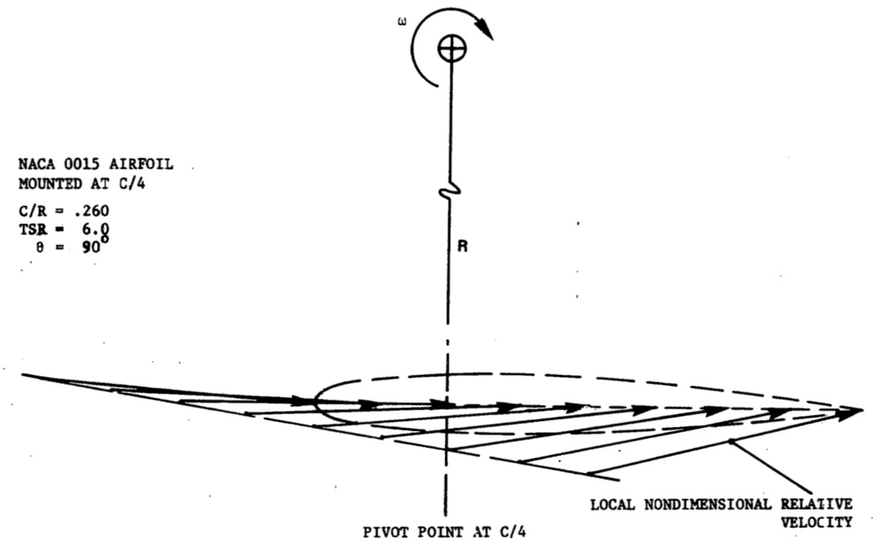

Figure 3.14: Example of the instantaneous local relative velocity distribution along the chord of a rotating profile [44].

Starting point of the theory is the derivation of the relative velocity and angle of attack distributions along the chord, assuming an undisturbed flow velocity equal to the freestream one (no blockage):

$$v_r(x/c) = \Omega R'(1+\varepsilon'^2 - 2\varepsilon' \sin(\vartheta'))^{\frac{1}{2}} \tag{3.28}$$

$$\alpha(x/c) = \arctan\left(\frac{\varepsilon' \cos(\vartheta')}{1-\varepsilon' \sin(\vartheta')}\right) + \Delta\vartheta \tag{3.29}$$

where the accented variables account for local values of considered quantities:

$$\Delta\vartheta = \arctan\left(\frac{x}{c} \cdot \frac{c}{R}\right) \tag{3.30}$$

$$R' = \frac{R}{\cos(\Delta\vartheta)} \tag{3.31}$$

$$\vartheta' = \vartheta - \Delta\vartheta \tag{3.32}$$

$$\varepsilon' = \frac{U_0}{\Omega R'} = \varepsilon \cos(\Delta\vartheta) \tag{3.33}$$

From equations 3.28 and 3.29, it can be inferred how, in terms of exchanged forces, $\mathrm{v_r}$, α chord-wise variations have the same effect of a virtual camber $\mathrm{y_c/c}$ and a pitch angle α_i added to the geometric airfoil, thus introducing a relevant source of asymmetry in its original symmetrical behaviour. Quantitative estimation of these two parameters derives from proper conformal mapping, which allows to preserve local velocities and incidence angles, basing on various geometric and operative characteristics of the rotating blade (see appendix B):

- **Blade angular position $\boldsymbol{\vartheta}$:** the vectorial composition of $\mathbf{v}_\mathrm{r}$ and $\mathbf{v}_\mathrm{l}$ depends on the blade orientation, so that both virtual camber and pitch vary along one blade revolution, as shown in figure 3.15b.

- **Blade-support arm attachment point position $\mathbf{x}_0$/c:** the blade mounting point influences the degree of asymmetry in $\mathbf{v}_\mathrm{r}$ distribution, i.e. the level of deviation between the kinematic conditions at the leading and trailing edges of the profile. As a consequence, both position of maximum camber and virtual pitch magnitude are strictly related to it.

- **Inverse tip-speed ratio ε:** the tip-speed ratio influences the shape of local velocity triangles, modifying the $\mathbf{v}_\mathrm{r}$ distribution along the chord. In particular, an increase in the TSR implies on one hand an increase in the oscillation amplitude of α around the reference point $\mathbf{x}_0$, thus enhancing the virtual camber effect, on the other a reduction of the offset induced by asymmetric blade mounting, i.e. not at half-chord, thus lowering the weight of virtual pitch.

- **Chord-to-radius ratio c/R:** as evident from figure 3.15a, the weight of flow curvature over global turbine behaviour increases linearly with the chord-to-radius ratio c/R. As a consequence, this effect becomes extremely relevant (given a certain number of blades $\mathrm{N_b}$) for small VAWTs such as the one under analysis, where rotor solidity (σ=$\mathrm{N_b}$c/(2R)) is raised as much as possible to maximize the blade Re.

Basing on methodology described so far, a transformed airfoil was derived from the original NACA0021 mounted on the turbine (see fig. 3.17), although with a few simplifying assumptions with respect to the original theory of Migliore. Due to the impossibility for the employed code of run-time polar data generation, dependence on the angular position ϑ was neglected, averaging instead the values of virtual camber and pitch over a rotor revolution; such operation is performed by evaluating these quantities for $\vartheta = 0°$ [44], i.e. when $\mathbf{v}_\mathrm{l}$ and $\mathbf{v}_\mathrm{tr}$ are orthogonal.

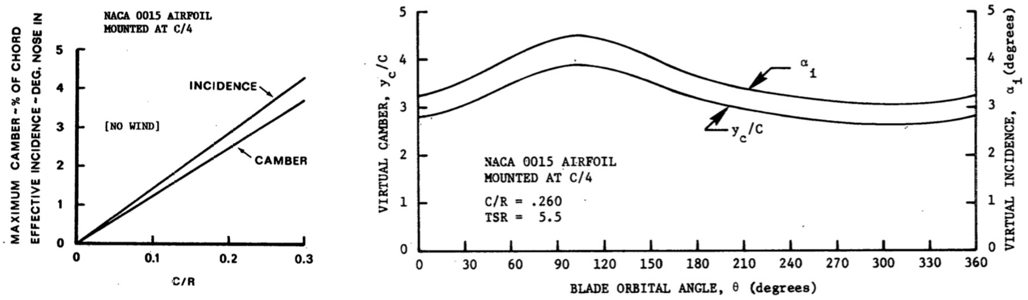

(a) Variation of $\mathrm{y_c}$/c, α_i with chord-to-radius ratio c/R

(b) Variation of $\mathrm{y_c}$/c, α_i with blade angular position ϑ

Figure 3.15: Examples of variation of virtual airfoil characteristics with respect to main flow and geometric parameters [44].

On the other hand, influence of the TSR on the virtual airfoil configuration was accounted only in part; the transformation was carried out for the maximum tip-speed ratio available in the experimental data (TSR=3.53), and then extended to the other operating conditions, instead of generating a new profile for each one for them. Such strategy allows to strongly reduce the overall computational effort, introducing a relatively small error, as highlighted by Bianchini et al. [13]; due to the absence of flow deflection associated to wind-blade interaction(blockage effect) in fact, Migliore's theory tends to overestimate sensitivity of virtual parameters with respect to TSR.

The corresponding polar data, reported in figure 3.18, was then derived with the procedure depicted in section 3.1.3 and inverted before plugging it into the solver; the original airfoil behaviour in curved flow is in fact equivalent to the transformed one in straight flow, with its camber line curving towards the center of rotation of the turbine [9], as shown in figure 3.16.

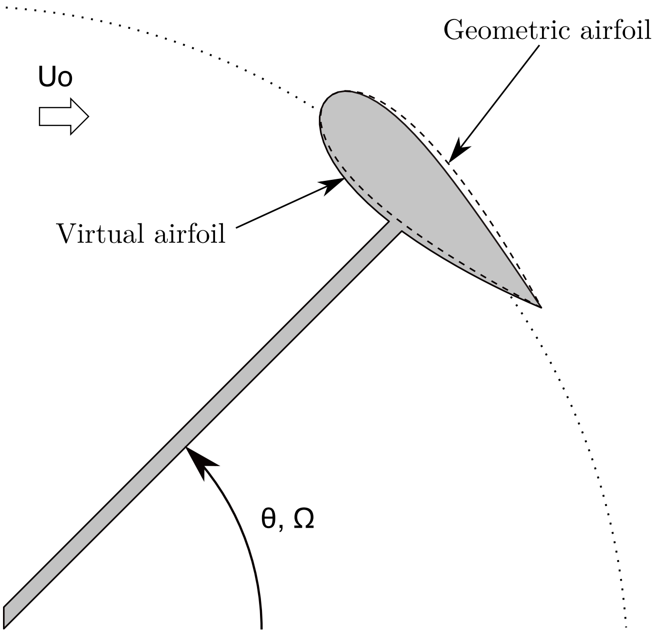

Figure 3.16: Comparison between the virtual and geometric airfoil configuration during turbine operation.

Table 3.1: Settings of the transformed NACA0021 airfoil simulation in XFoil.

(a) Virtual airfoil characteristics

c/R	0.167
x_0/c	0.5
y_c/c @ x/c=0.5	1.68
α_i [deg]	0°

(b) Simulation set-up

N	300
N_{crit}	9
Re range [-]	[50e3, 2e6]
α range [deg]	[-20°,20°]

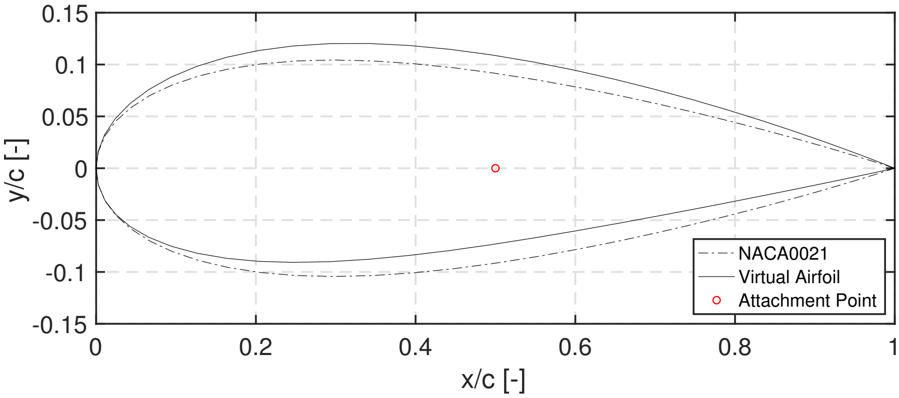

Figure 3.17: Comparison between original NACA0021 profile mounted on the turbine and the virtual one derived from Migliore conformal mapping technique, for TSR=3.53 and ϑ=0.

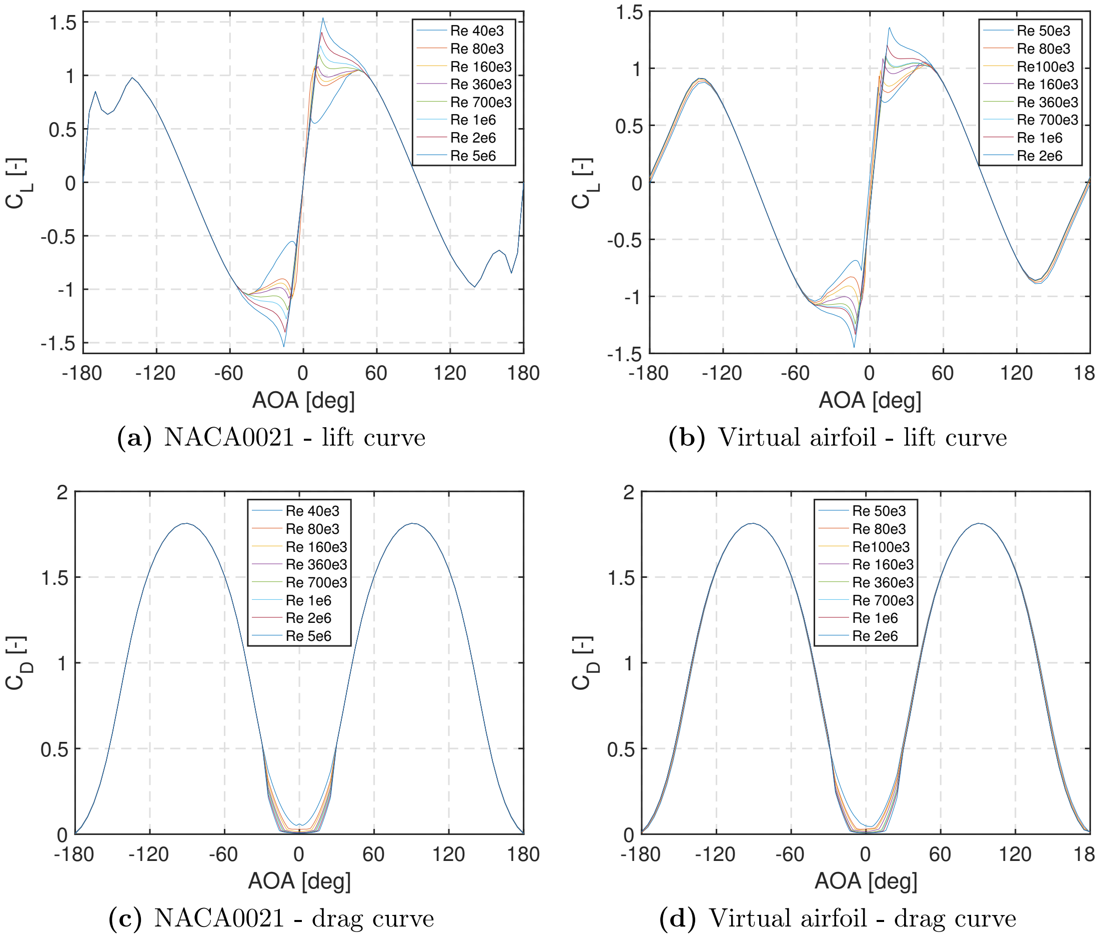

(a) NACA0021 - lift curve **(b)** Virtual airfoil - lift curve

(c) NACA0021 - drag curve **(d)** Virtual airfoil - drag curve

Figure 3.18: Comparison between the polar curves of the original NACA0021 profile mounted on the turbine and the virtual one derived from Migliore's conformal mapping technique.

3.1.5 Dynamic stall model

For large and rapid oscillations of the angle of attack as those experienced by VAWT blades, the nature of wind-blade interaction changes dramatically with respect to the static case, both in the attached and separated flow regions.

In the attached flow regime, dynamic loading introduces on one hand an amplitude oscillation of both lift and drag, whose characteristics depends on the forcing configuration, on the other hand a phase lag between the angle of attack experienced by the profile and its response in terms of exchanged aerodynamic forces; such effects, although not negligible, have nonetheless a minor impact on the global turbine behaviour [32].

As, in the same conditions, the angle of attack exceeds instead the static stall limit, triggering flow separation, airfoil behavior is severely altered due to the detachment of coherent vortex-like structures from its leading and trailing edges. This process, which commonly takes the name of *dynamic stall*, can be further distinguished in two sub-phases, according to the configuration assumed by the shed vortexes [39].

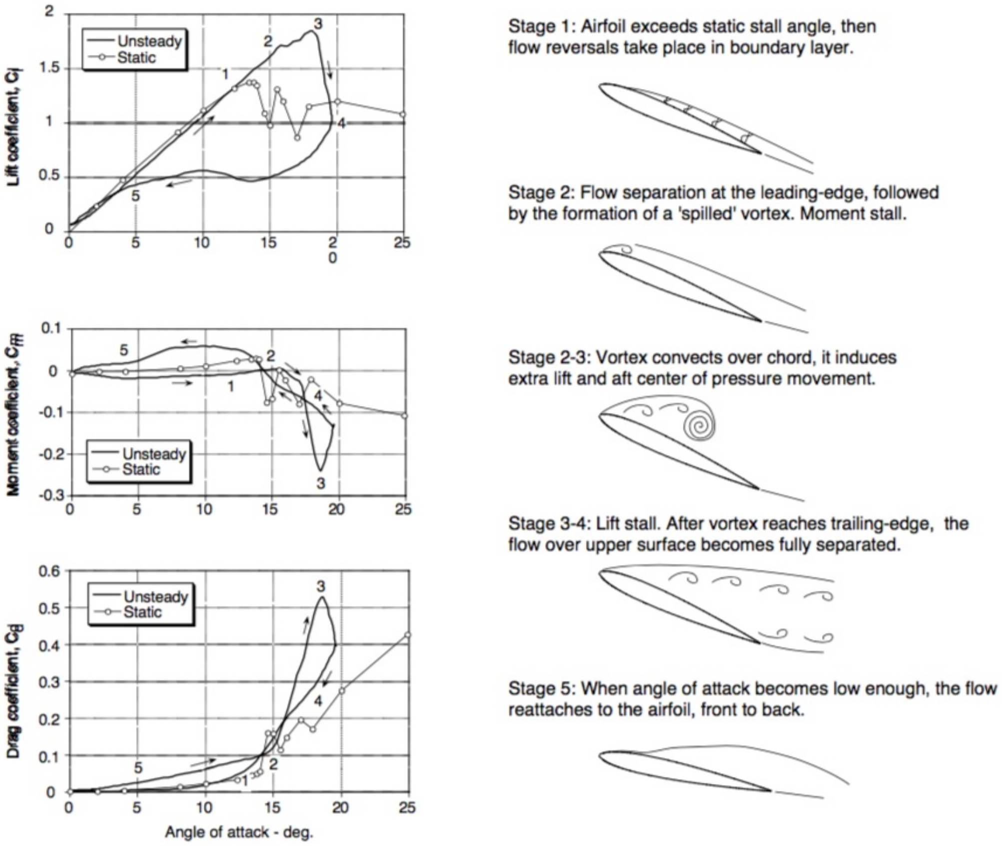

Stage 1: Airfoil exceeds static stall angle, then flow reversals take place in boundary layer.

Stage 2: Flow separation at the leading-edge, followed by the formation of a 'spilled' vortex. Moment stall.

Stage 2-3: Vortex convects over chord, it induces extra lift and aft center of pressure movement.

Stage 3-4: Lift stall. After vortex reaches trailing-edge, the flow over upper surface becomes fully separated.

Stage 5: When angle of attack becomes low enough, the flow reattaches to the airfoil, front to back.

Figure 3.19: Schematic of the various phases characterising dynamic stall development [32].

Light stall Increasing angle of attack beyond the static stall limit implies a progressive transition of the separation point from the trailing to the leading edge of the profile, as already described in section 3.1.3. In dynamic conditions, such phenomenon is related to the generation of an unsteady shear layer over the suction side of the airfoil, with consequent formation of roller-type structures (Kelvin-Helmhotz instability) following the separation point itself; together with the damping of LE pressure gradient associated to pitching motion [32], this flow pattern causes a delay in the stall onset, with enhanced lift and drag coefficients with respect to the static case (points 1-2, figure 3.19).

As it will be discussed more in detail later, the characteristics of the airfoil behaviour in this phase are dependent on multiple flow and geometric parameters, the most relevant being the LE non-dimensional radius $\mathrm{r_{LE}/c}$, which determines the type of transition from the attached to the separated regime; thinner airfoils tend to have more severe pressure gradients at the leading edge, with consequent LE separation and abrupt lift drop, in contrast with thicker ones, which present a progressive separation from the trailing to the leading edges, resulting in a more stable stall behaviour [39].

Deep stall As the angle of attack is further increased beyond the deep stall limit, the separation point reaches the airfoil leading edge, setting up the conditions for the clustering of corresponding roller vortexes and the consequent formation of a large, coherent LE vortex. Such structure is conveyed across the blade chord, increasing both lift and drag beyond their static maxima and shifting the center of pressure towards the rear part of the airfoil (points 2-3, figure 3.19), until it reaches the trailing edge; there, it detaches due to the simultaneous formation of a TE vortex. In the reattachment phase, i.e. for decreasing angle of attack, airfoil lifting capability is decreased instead below the static one, due to massive separation following the LE vortex shedding event (points 3-4, figure 3.19).

The final results of the phenomena described so far are a strong hysteresis in airfoil behaviour, with different aerodynamic coefficients in the detachment and reattachment phase, and a phase lag between the profile motion and the exchanged force; being the dynamics of the shed vortexes fairly decoupled from the one of the blade, the characteristics of such hysteresis cycle present a weak sensitivity to the main flow (Re, M) and geometric parameters, while retaining a strong dependence on the variables regulating the LE vortex shedding event, especially reduced frequency and angle of attack history [39].

Dynamic stall presents an elevated degree of complexity, depending, in contrast with its static counterpart, on both geometric, kinematic and dynamic parameters of the flow and the blade, with different sensitivity according to the considered stall regime. In order to gain a better comprehension of its behaviour, the main governing parameters are here described, following the guidelines given by [39]:

- **Airfoil geometry:** airfoil geometry, in particular the LE relative radius $\mathrm{r_{LE}/c}$, plays a paramount role in defining the profile behaviour in the light stall region, where it determines the type of boundary layer separation and so the dynamics of roller vortexes. As $\mathrm{r_{LE}/c}$ increases, causing a shift from abrupt LE to progressive TE stall, the separation process tends to become more stable, increasing the stall delay and reducing the amplitude of the hysteresis cycle associated to the reattachment phase. In the deep stall region instead, the difference between the two tends to disappear, due to the full development of the vortex shedding phenomenon.

- **Reduced frequency $\mathbf{k_s}$:** reduced frequency is probably the most important parameter regulating dynamic stall, since it determines the overall weight of unsteady phenomena over the mean flow behaviour. In its most general expression, it is defined as the ratio between the characteristic frequencies of unsteady forcing and steady mass transport over the profile chord:

$$k_s = \frac{f_{unsteady}}{f_{steady}} = \frac{\omega c}{2v_r} \tag{3.34}$$

  where ω is a characteristic pulsation of unsteady forcing. Its effect varies according to the type of airfoil and the stall regime considered. In the light stall phase, an increase in $\mathrm{k_s}$ tends to enhance stall delay and reduce hysteresis cycle amplitude for thicker airfoils, while the opposite trend is encountered for thinner ones. In deep stall conditions instead, reduced frequency acts as a threshold value for the detachment of the LE vortex; for $\mathrm{k_s} < 0.05$ in fact, there are no relevant differences between light and deep stall behaviour.

- **Angle of attack history $\boldsymbol{\alpha}\mathbf{(t)}$:** angle of attack history governs together with reduced frequency the LE vortex shedding event and so the amplitude and shape of the corresponding hysteresis cycle. A relevant role is played in particular by the maximum and minimum angle of attack values, $\alpha_{\max}$, $\alpha_{\min}$, respectively involved in the flow detachment and reattachment phases.

- **Mach number M:** even at the low freestream Mach number interesting applications in which dynamic stall is usually encountered, transonic/supersonic flow can develop near the airfoil LE under high incidence conditions, influencing the vortex shedding phenomenon. In general, increasing M tends to damp out the dynamic stall effects on the mean flow, up to the point where the formation of vortexes is inhibited by the one of shock waves.

As it can be inferred from previous considerations, dynamic stall can have a major impact on VAWTs performances, not only from the performance perspective, since the overall power extraction is altered by the lift and drag hysteresis cycle, but also from a structural one, due to the higher oscillation in exchanged aerodynamic forces and the negative damping introduced by the LE vortex shedding event (see figure 3.19), which in some cases may lead to flutter instability; an additional source of disturbance may also derive from the interaction of vortexes shed from one blade with neighbouring ones, as shown in figure 3.20. For this reason, the development and implementation of an accurate model is pivotal for the correct design of these machines, especially when their transient operation, e.g. start-up and brake-down, are considered; these conditions are in fact interested by the highest degree of oscillation, due to the corresponding low TSR.

In the current work, it was chosen to implement the dynamic stall model proposed by Massé [37] and improved by Berg [6], since, according to various authors [11, 38],

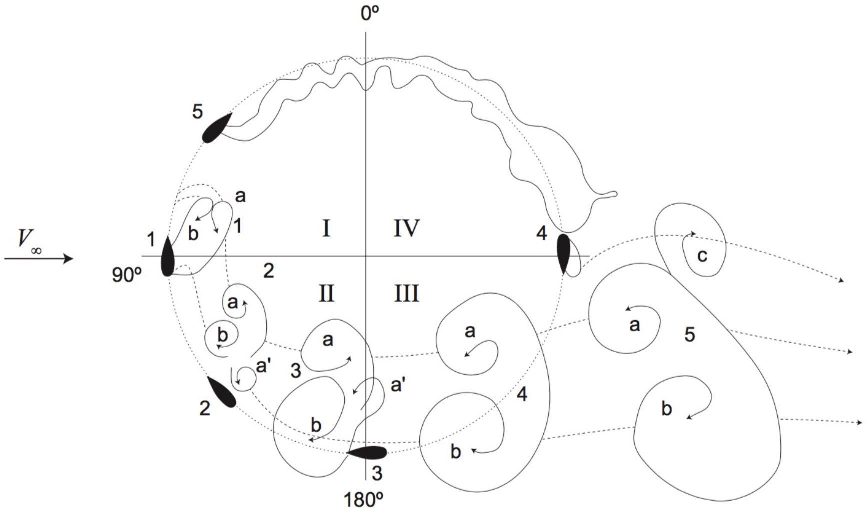

Figure 3.20: Schematic of the flow developing across a VAWT rotor in dynamic stall conditions, highlighting the LE vortex-blade interaction [21].

it represents the optimal trade-off between accuracy and implementation effort. In its most general form, it represents an adaptation to VAWTs of the semi-empirical Gormont model [23], originally developed for helicopters. Dynamic effects are embedded in the solution by entering the available polar data with a modified angle of attack α_{ref}:

$$\alpha_{ref} = \alpha - K_1 \Delta\alpha \tag{3.35}$$

where K_1 is an empirical constant, accounting for the direction of the angle of attack variation, i.e. whether the flow is detaching or reattaching, while $\Delta\alpha$ is a dynamic correction to the static angle of attack α. The latter varies linearly with an index of unsteady forcing S, derived from reduced frequency, via a set of sensitivity parameters γ_{i}, that depend on the airfoil maximum thickness t/c and on M:

$$\Delta\alpha = \begin{cases} \gamma_1 S & \text{for} \quad S \leq S_C \\ \gamma_1 S_C + \gamma_2 (S - S_C) & \text{for} \quad S > S_C \end{cases} \tag{3.36}$$

where S_C is a threshold parameter depending on t/c. It must be noted how γ_{i} assumes different values whether lift or drag are considered, leading to different correction for the the two curves. The reduced frequency index S takes the form:

$$S = \sqrt{\left| \frac{c\dot{\alpha}}{2v_r} \right|} \tag{3.37}$$

with $\dot{\alpha}$ derivative over time of the angle of attack. Eventually, dynamic lift and drag coefficients are evaluated by plugging α_{ref} in the available static tabulated polars. In order to distinguish between the attached and separated flow regions, an ad hoc extrapolation procedure is used for the lift coefficient:

$$\begin{cases} C_L^{dyn} = C_L(\alpha_0) + m(\alpha - \alpha_0) \\ C_D^{dyn} = C_D(\alpha_{ref}) \end{cases} \tag{3.38}$$

where the slope m is determined from the following equation:

$$\mathrm{m} = \min\left[\frac{C_L(\alpha_{ref}) - C_L(\alpha_0)}{\alpha_{ref} - \alpha_0}, \frac{C_L(\alpha_{SS}) - C_L(\alpha_0)}{\alpha_{SS} - \alpha_0}\right] \tag{3.39}$$

where α_0 is an arbitrary reference angle of attack, usually the zero-lift one.

According to Massé [37], the Gormont model, being originally developed for helicopter blades, for which the maximum angle of attack is much lower than for VAWT ones, tends to overestimate dynamic stall effects in the deep stall region; as a consequence, the author proposed to compute the dynamic lift and drag coefficients as linear interpolation between the static and the Gormont ones:

$$C_L^{mod} = \begin{cases} C_L + \left[\frac{A_M\alpha_{SS}-\alpha}{A_M\alpha_{SS}-\alpha_{SS}}\right](C_L^{dyn} - C_L) & \text{for} \quad \alpha \leq A_M\alpha_{SS} \\ C_L & \text{for} \quad \alpha > A_M\alpha_{SS} \end{cases} \tag{3.40}$$

$$C_D^{mod} = \begin{cases} C_D + \left[\frac{A_M\alpha_{SS}-\alpha}{A_M\alpha_{SS}-\alpha_{SS}}\right](C_D^{dyn} - C_D) & \text{for} \quad \alpha \leq A_M\alpha_{SS} \\ C_D & \text{for} \quad \alpha > A_M\alpha_{SS} \end{cases} \tag{3.41}$$

where $\mathrm{A_M}$ is a semi-empirical constant. Starting from Massé formulation, Berg [6] introduced further modifications, leading to the model adopted for this thesis; on one hand, it was proposed to define α_{SS} as the angle at which the lift characteristic curve starts departing from the linear behaviour, on the other hand to use $\mathrm{A_M}$=6, which is the value best fitting the experimental performances of the VAWT Sandia 17-m. For a complete description of the Berg model and its implementation into the code, see appendix C.

In the present work, it was chosen to use, beside the value recommended by Berg, $\mathrm{A_M}$=20, which in a recent work of Bianchini et al. [11] was found to be particularly predictive for small VAWTs; in this way, a better understanding of the effects of this constant over the model performance is achieved.

3.1.6 Tip loss correction

Due to their finite extension in the spanwise direction, the flow developing around VAWT blades is fully three-dimensional, with vortex-like structures shedding from the blade trailing edge along its full length and gathering at its extremities to form the so-called tip vortexes. In the tip region in fact, the discontinuity in pressure between the lower and upper surfaces of the blade, caused by its sudden interruption, is compensated by the onset of a spanwise flux, going from the pressure to the suction side; its influence is then extended to the whole blade length, severely distorting the flow configuration with respect to the two-dimensional case. On the pressure side, a spanwise velocity component arises, directed to the blade extremities; as a consequence, a progressively lower pressure is encountered approaching the tip, while the flow streamlines are deviated towards the outer regions. On the suction side instead, the opposite trend is observed. As the distorted streamlines coming from the two sides of the airfoil meet at the trailing edge, they form a continuous vortex sheet, which, according to Helmhotz theory, rolls up downstream into a more coherent structure, i.e. the tip vortex [2].

From an aerodynamic point of view, the effects of these phenomena are various and hard to decouple. Spanwise flow deviation, whose tip vortexes are the most evident manifestation, reduces the blades efficiency, penalising lift and enhancing drag (induced drag). For the same reason, blade loading decreases approaching the tip region, with a significant drop in performances at blade ends [2]; in that region furthermore, according to [3], wind-turbine interaction and corresponding wake shape is severely distorted by the presence of tip vortexes, so that the entire flow field is markedly altered.

The final consequence of these phenomena is a considerable loss in the turbine efficiency; therefore, their proper evaluation and integration in the solution procedure is necessary for a correct performance prediction. In such perspective the ACL, thanks to its fully three-dimensional formulation, should be capable to resolve all the features described so far without additional modelling effort; as pointed out by [22] however, the tip vortex shedding event and corresponding blade loading spanwise gradient, although present, may be underestimated. Thus, in order to improve the code prediction capabilities, the tip loss correction developed by Glauert was implemented into the solver, after having adapted it to work with VAWTs:

$$F = \frac{2}{\pi}\cos^{-1}\left[\exp\left(-\frac{N_b(H-h)}{2h\sin(\varphi)}\right)\right] \tag{3.42}$$

where h is the local distance of the considered section from blade midspan, and φ the local incidence angle. Such correction is directly applied to the computed volume force, before plugging it into the computational grid.

3.2 Flow model

The description of the wind-turbine interaction is completed by combining the ACL model of the turbine with the FV treatment of the flow field, consisting, as thoroughly described in section 1.3.3, in the discretisation over a proper computational domain of the Navier-Stokes set of equations, in this case in their incompressible form:

$$\begin{cases} \nabla\cdot\boldsymbol{U} = 0 \\ \frac{\partial \boldsymbol{U}}{\partial t} + \nabla\cdot(\boldsymbol{U}\otimes\boldsymbol{U}) = \mathbf{f} - \frac{\nabla P}{\rho} + \nabla\cdot(\nu\nabla\boldsymbol{U}) \end{cases} \tag{3.43}$$

The resolution of equations 3.43 is however extremely cumbersome due to the presence of *turbulence*, which strongly raises the level of complexity of the flow. In general, turbulence can be defined as *a dissipative flow state characterised by non-linear fluctutating three-dimensional vorticity* [30], which results macroscopically in an enhanced mass, momentum and energy transfer. According to [30], main features of such phenomenon can be resumed as follows:

- **Fluctuations:** all flow quantities (velocity, pressure, etc. . .) experience irregular, chaotic fluctuations in both time and space. This occurs independently from the nature of boundary conditions.

- **Non-linearity:** turbulence is a strongly non-linear phenomenon, resulting from the unstable propagation and amplification of spontaneous flow disturbances. Necessary condition for this to happen is a sufficiently high value of a relevant non-linearity parameter, e.g. the Reynolds number. The same non-linearity also reflects on the main mechanism allowing the turbulent state to maintain its coherence over time, i.e. vortex stretching.
- **Vorticity:** the turbulent flow pattern is characterised by a multitude of vortexes, or eddies, of different shapes and sizes, mutually interacting and distorting each other; the corresponding range of scales can be very wide, with a difference of several orders of magnitude between the smaller and the larger structures, and increases with Re.
- **Dissipation:** vortex stretching implies the non-linear transfer of energy from larger scale eddies to smaller ones, where it is dissipated in form of heat due to viscous interaction; such mechanism takes the name of *energy cascade* and it is the main process regulating the turbulent regime, as it will be discussed in section 3.2.1.
- **Diffusivity:** macroscopic fluctuations enhance the transfer of mass,momentum and energy with respect to the laminar case.

The direct simulation of all the features described so far (DNS) would require an extremely high temporal and spatial resolution, which, combined to the lack of stability deriving from the elevated degree of non-linearity of the turbulent phenomenon, raises the overall computational effort to non-feasible levels.

For this reason, it was chosen to average over time the set of equations 3.43, so that the generic flow variable φ could be expressed as the sum of a mean (first-order statistics) $\bar{\varphi}$ and a fluctuating component φ':

$$\varphi(x,t) = \bar{\varphi}(x) + \varphi'(x,t) = \frac{1}{T}\int_T \varphi(x,t)dt + \varphi'(x,t) \tag{3.44}$$

Result of such procedure is the Unsteady Reynolds-Averaged Navier Stokes (URANS) set of equations:

$$\begin{cases} \nabla \cdot \bar{\boldsymbol{U}} = 0 \\ \frac{\partial \bar{\boldsymbol{U}}}{\partial t} + \nabla \cdot (\bar{\boldsymbol{U}} \otimes \bar{\boldsymbol{U}}) = \mathbf{f} - \frac{\nabla \bar{P}}{\rho} + \nabla \cdot (\nu \nabla \bar{\boldsymbol{U}}) - \nabla \cdot \frac{\bar{\bar{r}}}{\rho} \end{cases} \tag{3.45}$$

The term $\bar{\bar{\mathrm{r}}}$, which takes the name of Reynold stress tensor, represents the contribution of turbulent fluctuations to mean flow development, and is responsible for energy dissipation and enhanced mixing:

$$\bar{\bar{r}} = -\rho\overline{\boldsymbol{u} \otimes \boldsymbol{u}} = -\rho \begin{bmatrix} \overline{u^2} & \overline{uv} & \overline{uw} \\ \overline{vu} & \overline{v^2} & \overline{vw} \\ \overline{wu} & \overline{wv} & \overline{w^2} \end{bmatrix} \tag{3.46}$$

where u,v,w are the cartesian components of the fluctuating velocity vector. By relating $\bar{\bar{\mathrm{r}}}$ to the mean flow characteristics via an ad hoc model, which commonly takes the name of *turbulence model*, it is possible to avoid the numerical resolution of the turbulent fluctuations, thus achieving a noteworthy improvement in the computational efficiency of the simulation.

3.2.1 Turbulence model

Since in the URANS formulation the turbulent fluctuating component of the flow is fully modelled, the choice of the proper turbulence model is pivotal for the reliability of the simulation; in the frame of engineering applications in particular, the main requirement to the chosen scheme is its capability to mimic the transfer of energy between the larger and smaller eddies scales, which regulates the rate of dissipation in the whole turbulent region.

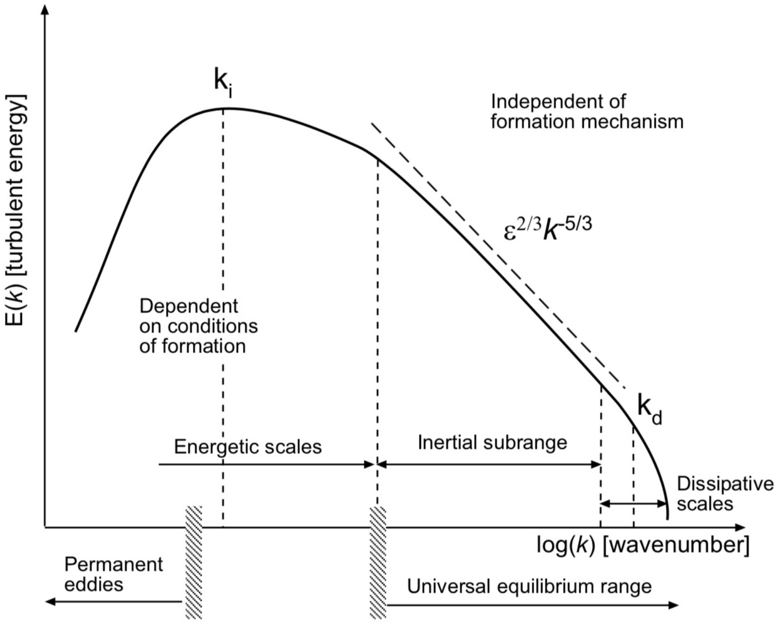

Figure 3.21: Schematic representation of the Kolmogorov energy cascade [58].

Most models currently adopted in industrial and scientific environments are build on the theory of the energy cascade proposed by Kolmogorov [29], which is fundamentally based on the assumption of *isotropic turbulence*; the behaviour of the turbulent region tends to become more isotropic and independent from applied boundary conditions as the smaller scales of interaction are approached, so that, below a certain scale, a common structure can be found for all turbulent flows, as reported in figure 3.21:

- **Integral scale:** having a characteristic dimension which is of the same order of magnitude of the one of the problem, integral scale eddies interact directly with the mean flow, extracting energy and transferring it to the smaller scales. Thus, this scale contains most of the global turbulent kinetic energy and is also the most sensitive to external boundary conditions, as reported in figure 3.21. For the same reason, it is the most difficult to model in a general way.
- **Taylor scale or inertial sub-range:** the inertial sub-range is a buffer layer transferring energy from the integral to the viscous scale, whose eddies are too small to perceive the influence of boundary conditions, but large enough not be affected by viscosity. Its configuration is therefore regulated only by the energy dissipation rate ε imposed by the larger scales, and can be regarded as universal.

- **Kolmogorov scale:** vortex structures smaller than the Kolmogorov length $l_k \propto (\nu^3/\varepsilon)^{0.25}$ are damped out by the predominant role of viscosity, resulting in the conversion into heat of the turbulent kinetic energy coming from the larger scales. Together with the inertial sub-range, this scale constitutes what is known as the universal equilibrium range, where turbulence is considered to be fully developed and free from the disruptive influence of boundaries and other forcing effects. For these characteristics, it is the most suited to be described with semi-empirical models.

Basing on previous considerations, the turbulent interaction can be interpreted as an unidirectional energy flow from the larger to the smaller scales, converting the mean flow kinetic energy into heat. The dissipation rate ε is constant along the turbulent spectrum and imposed by the larger scales, i.e. the characteristics of the mean flow itself. It becomes natural then to relate the turbulent stress tensor $\bar{\bar{\mathrm{r}}}$ to the mean flow velocity field via a proper diffusion constant μ_{T}, that takes the name of eddy viscosity (Boussinesq hypothesis), leading to the following form of equations 3.45:

$$\begin{cases} \nabla \cdot \bar{\boldsymbol{U}} = 0 \\ \frac{\partial \bar{\boldsymbol{U}}}{\partial t} + \nabla \cdot (\bar{\boldsymbol{U}} \otimes \bar{\boldsymbol{U}}) = \boldsymbol{f} - \frac{\nabla \bar{P}}{\rho} + \nabla \cdot ((\nu + \nu_T)\nabla \bar{\boldsymbol{U}}) \end{cases} \tag{3.47}$$

Equations 3.47, when combined with a proper modelling of μ_{T}, bring to the closure of the problem, allowing the full resolution of the turbulent flow.

For the purpose, in the current work it was chosen to implement the k-ω Shear Stress Transport (SST)[1]model developed by Menter [40]. In its basic formulation, two transport equations, one for turbulent kinetic energy k and one for turbulent frequency ω, are built combining the characteristics of the standard k-ε [31] and k-ω [60] models via an ad hoc blending function F:

$$\mathbf{k}: \quad \rho \frac{\partial k}{\partial t} + \rho \bar{\mathbf{U}} \cdot \nabla k = \bar{\bar{r}} : \nabla \bar{\mathbf{U}} - \rho C_D \frac{k^{1.5}}{l_T} + \nabla \cdot \left(\left(\mu + \frac{\mu_T}{\sigma_k} \right) \nabla k \right) \tag{3.48}$$

$$\begin{aligned} \boldsymbol{\omega}: \quad & \frac{\partial \omega}{\partial t} + \bar{\mathbf{U}} \cdot \nabla \omega = C_{\omega 1} \frac{\omega}{k} \bar{\bar{r}} : \nabla \bar{\mathbf{U}} - C_{\omega 2} \omega^2 + \nabla \cdot \left(\left(\frac{\mu}{\rho} + \frac{\mu_T}{\rho \sigma_{\omega 3}} \right) \nabla \omega \right) \\ & + (1 - F) \frac{2 \nabla \omega \nabla k}{\sigma_{\omega 2} \omega} \end{aligned} \tag{3.49}$$

where $\mathrm{C_D}$, $\mathrm{C_{\omega i}}$ and $\sigma_{\omega \mathrm{i}}$ are semi-empirical constants. Near the wall, the k-ω model is adopted, allowing an accurate and robust wall treatment in both high- and low-Re conditions. As a matter of fact, wall damping functions are not required. In the freestream instead, the k-ε formulation is used, improving the resolution of shear layer turbulence and strongly reducing the sensitivity to initial conditions shown by k-ω. Eventually, μ_{T} field is computed from k and ω, according to equation 3.50:

$$\mu_T = \rho C_\mu \frac{k}{\omega} \tag{3.50}$$

where C_μ is a semi-empirical constant. It must be noted how the model described so far, as well as all approaches based on the Boussinesq hypothesis, is founded on

---

[1] Thanks to the absence of physical walls, also the standard k-ε turbulence model would have been a viable option. In virtue of the SST formulation nonetheless, its effects are present anyway in the current work.

the assumptions of *local equilibrium* and *isotropy* of the turbulent configuration at the smaller scales, which are usually not met in flow singularities such as high shear regions. In the boundary layer for instance, not only there is a lag in energy dissipation, undermining the hypothesis of local equilibrium, but the presence of the wall also limits the three-dimensional development of neighbouring eddies, introducing an elevated degree of anisotropy at the smaller scales which results in an inverse energy cascade [58]. If the former issue is partially compensated by the SST thanks to the transport equation for k, the latter is intrinsically related to the model formulation and should be taken on with more advanced approaches; in the frame of the ACL method however, its relevance is strongly diminished by the absence of the blades.

3.3 Computational domain

A open-field configuration was chosen for the employed numerical domain, so that the flow conditions of the open-jet wind tunnel tests taken as benchmark for the current analysis (see section 2.2) could be properly reproduced with a relatively high accuracy; in the open-jet configuration in fact, as reported in [17], the blockage effect associated to the presence of the wind tunnel is estimated to be sufficiently small to be neglected without compromising the quality of the results.

The computational domain was divided into an *internal* region, where the interaction between the wind and the turbine blades could be resolved via ad hoc refinement, and an *external* one, necessary to correctly propagate the effects of such interaction to the far field and impose the proper boundary conditions.

3.3.1 External domain

The external region dimensions were evaluated in such a way, that the typical far field external flow boundary conditions could be applied with the minimum computational effort, i.e. number of elements. For the purpose, the sensitivity analysis carried out by Ferlini [22] was taken into consideration, leading to the set of dimensions reported in table 3.2a.

For the discretisation of the domain, a structured hexahedral mesh was employed, built via the OpenFOAM utility *blockMesh*. As reported in [22], the number of the cells in this region doesn't affect in a relevant way the outcome of the simulation, so that their dimension was chosen according to the required mesh refinement level in the internal zone.

3.3.2 Internal domain

The internal domain was built following the flow structures developing around the turbine, as it can be seen in figure 3.22. For the proper discretisation of the wind-turbine interaction region, a cylindrical refinement zone was defined, where the actuator line forces coming from the ACL algorithm are inserted. It must be noted how the axis of such region was shifted towards the inlet with respect to the one of the turbine, so that the its blockage effect on the wind could be captured; as a matter

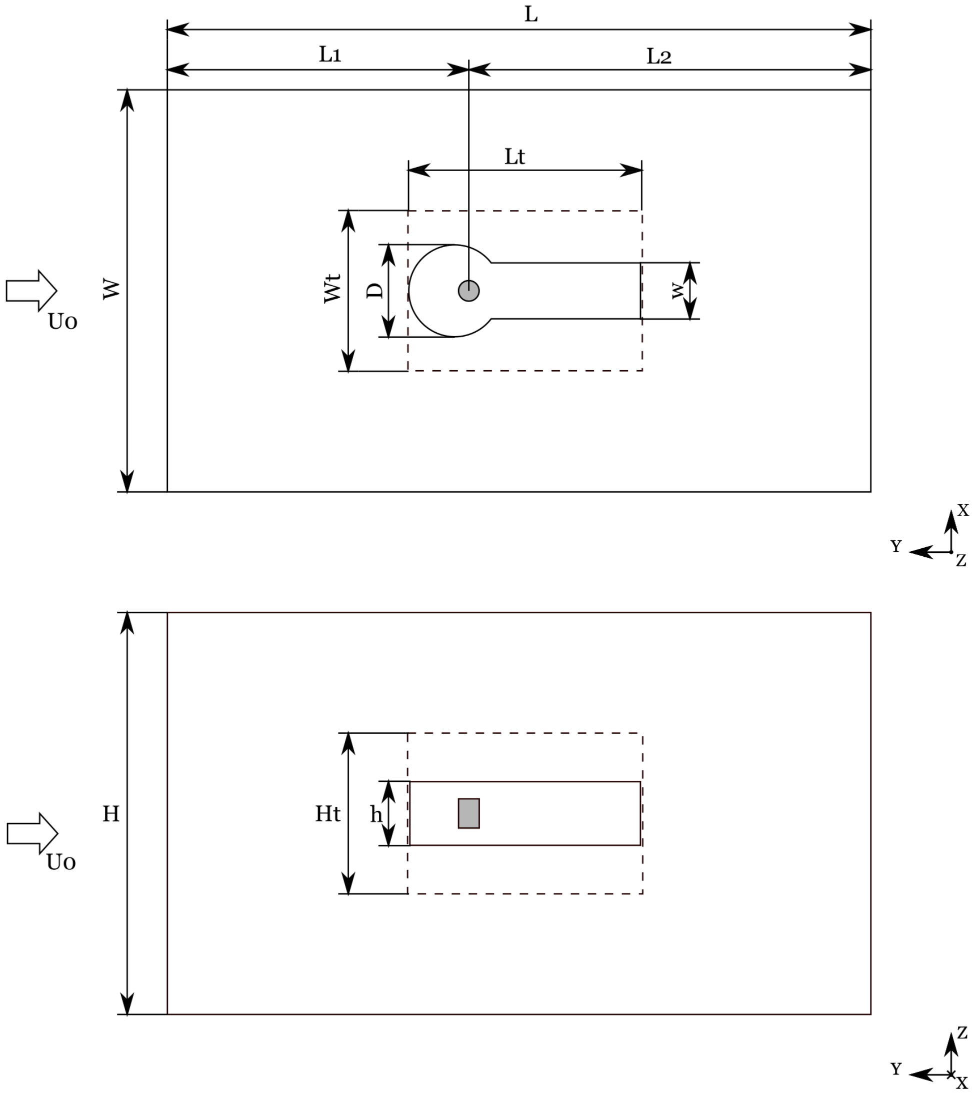

Figure 3.22: Computational domain employed for the analysis, identified by the continuous lines. The position of the turbine is represented instead by the gray shaded region. Test domain used for internal region dimensioning is associated to the dotted contour.

Table 3.2: Dimensions of the computational domain employed for the analysis.

(a) External domain dimensions

L [m]	L_1 [m]	L_2 [m]	W [m]	H [m]
35	15	20	20	20

(b) Internal domain dimensions

w [m]	h [m]	D [m]
2.8	3.2	4.6

(c) Test domain dimensions

L_t [m]	W_t [m]	H_t [m]
11.5	8	8

of fact, the presence of the machine, especially at high loading conditions, induces a strong deceleration on the upstream flow, which must be adequately resolved to avoid severe distortions of the simulation results. Same strategy was adopted for the wake shedding downstream, dimensioning the corresponding refinement box according to its three-dimensional development.

As for the external region, a structured hexahedral mesh was employed, built via the option *refinementRegions* of the OpenFOAM utility *snappyHexMesh*. Exact dimensions of both turbine and wake refinement zones, reported in table 3.2b, were evaluated via an ad hoc sensitivity analysis, aimed at minimizing on one side the disturbance associated to the interface between the external and internal domains, on the other side the global number of cells, still ensuring the correct resolution of the relevant flow features; in particular, various mesh configurations were validated against the one adopted in [22] (see figure 3.22), which was already subjected to a similar procedure, selecting those that showed no relevant deviations in the outcome of the simulation. This test campaign was carried out under high loading (TSR=3.3), where, according to [17], turbine blockage and wake enlargement reach the maximum magnitude, and its results were then extended to the other operating conditions. No sub-models were applied in this context.

3.3.3 Grid independence test

The definition of the computational grid was completed by the assessment of the optimal mesh resolution. For the purpose, a grid sensitivity analysis was carried out, adopting as convergence index the power coefficient C_P, for three benchmark operating conditions: a high (TSR=3.3), optimal (TSR=2.5) and low loading one (TSR=1.5). This way, the resulting mesh could be optimised for the whole range of flow configurations associated to VAWT operation. For the same reason, a double-check was made on the internal region dimensioning (see section 3.3.2), by comparing obtained results with those deriving from a simulation made with the test mesh of figure 3.22.

Eventually, mesh M4, whose characteristics are reported in table 3.3, was chosen for all operating conditions. Although in fact full convergence is not reached for any TSR, in all cases the percent deviation from the coarser mesh M3 is low enough to reasonably justify its adoption, as it can be inferred from figures 3.25, 3.24 and 3.23.

Table 3.3: Characteristics of the various meshes used for the grid independence test.

Mesh	N_{cells}	Cell dimension [m] (ext.region)	Cell dimension [m] (int. region)
M1	629’384	0.5	0.0625
M2	4’071’732	0.5	0.03125
M3	7’871’620	0.4	0.025
M4	13’472’396	0.33	0.020

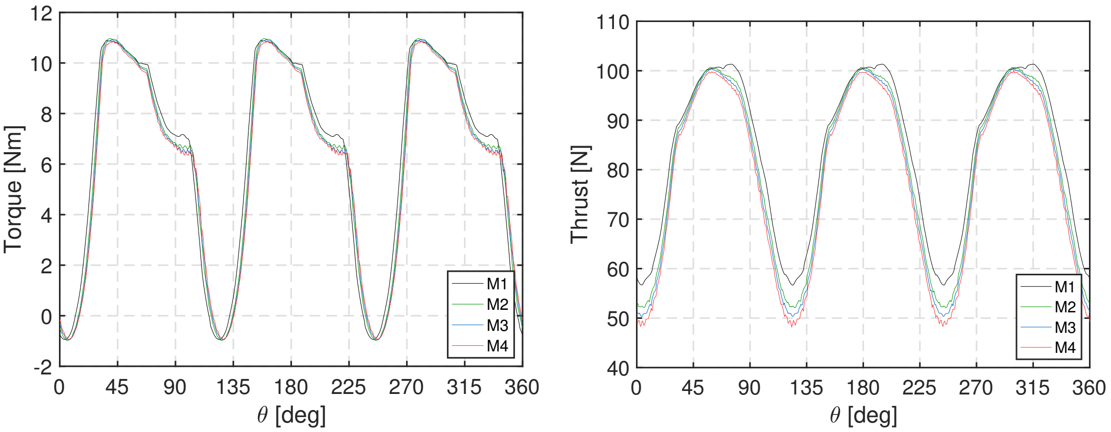

(a) Torque **(b)** Thrust

Mesh	M1	M2	M3	M4
C_P	0.0990	0.0963	0.0951	0.0942

(c) Average power coefficient

Figure 3.23: Comparison between the different meshes used for the grid independence test, in terms of global torque and streamwise thrust profiles over a revolution, and the corresponding average power coefficients (TSR=1.5).

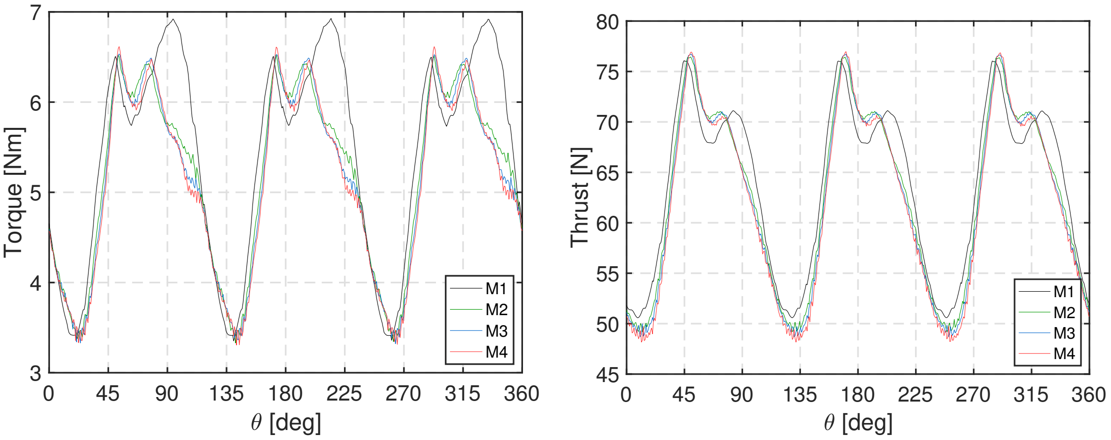

(a) Torque **(b)** Thrust

Mesh	M1	M2	M3	M4
C_P	0.3938	0.3747	0.3705	0.3683

(c) Average power coefficient

Figure 3.24: Comparison between the different meshes used for the grid independence test, in terms of global torque and streamwise thrust profiles over a revolution, and the corresponding average power coefficients (TSR=2.5).

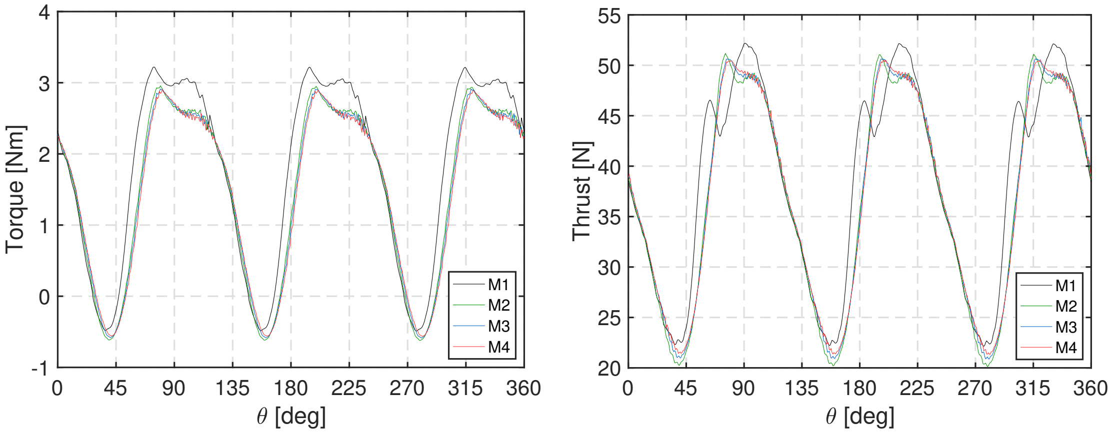

(a) Torque **(b)** Thrust

Mesh	M1	M2	M3	M4
C_P	0.2971	0.2495	0.2480	0.2457

(c) Average power coefficient

Figure 3.25: Comparison between the different meshes used for the grid independence test, in terms of global torque and streamwise thrust profiles over a revolution, and the corresponding average power coefficients (TSR=3.3).

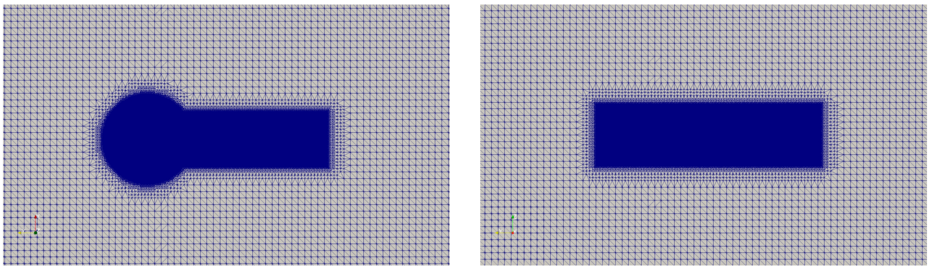

(a) Top view **(b)** Side view

Figure 3.26: Overview of the mesh M4 adopted for the simulation campaign.

3.4 Boundary and initial conditions

The initial and boundary conditions were specified consistently with the domain definition and the incompressible nature of the flow:

Inlet patch At the inlet, the freestream velocity U_0 was imposed according to the TSR under consideration, while a Neumann condition (*zeroGradient*) was adopted for pressure. The inlet value for the turbulent kinetic energy k was derived basing on a turbulence intensity I of 0.2%, measured at the inlet of the experimental test chamber, assuming isotropic turbulence condition (u=v=w):

$$k = \frac{3}{2}(U_0 \cdot I)^2 \tag{3.51}$$

The turbulent frequency ω was evaluated instead from equation 3.52, using as mixing length value l the 0.5% of the height of the wind tunnel nozzle employed in the experimental campaign (see section 2.2), as suggested by [22]:

$$\omega = \frac{\sqrt{k}}{l} \tag{3.52}$$

The kinematic eddy viscosity ν_{T} is *calculated* from the values imposed to k and ω.

Outlet patch Assuming that the outlet patch is far enough from the turbine for the flow to be considered undisturbed, the *zeroGradient* condition was imposed to all flow variables, except pressure, whose value was fixed equal to the atmospheric one. Only ν_{T} was set to *calculated*, as at the inlet.

Lateral surfaces The lateral surfaces were placed in such a way, that the lack of symmetry induced by turbine rotation on the freestream is completely smeared out, allowing the adoption of a *symmmetryPlane* boundary condition: the component of the velocity normal to the surface is set to zero and all the other components and variables have to respect the condition of *zeroGradient*.

Upper and lower patches Same strategy adopted for the lateral surfaces was used for the lower and upper patches, imposing *symmetryPlane* to all flow variables.

Initial conditions The initialisation of the flow field depended on the considered variable: for k, ω and U, the inlet value was used, while the initial pressure field was set equal to the atmospheric one. ν_{T} was put equal to 0.

3.5 Numerical set-up

As anticipated in section 1.3.3, the choice of the proper differentiation schemes is fundamental for both accuracy and stability of a CFD simulation. Due to the marked differences between the various terms of the NS equations used to model the flow behaviour, a dedicated optimisation was required for each one of them:

Time derivative for the discretisation of the unsteady terms, an implicit *Euler* differentiation scheme was employed, since it does not suffer from the stability issues characterising the higher order methods, such as Crank-Nicholson. Its lower accuracy (first order) was compensated in the present work by the elevated temporal resolution used for the simulation campaign.

Spatial gradient spatial gradient terms were handled with a second order *linear* scheme, linearly interpolating the generic cell face value φ_{f}, required for gradient evaluation, from the corresponding centroid values in the neighbouring cells.

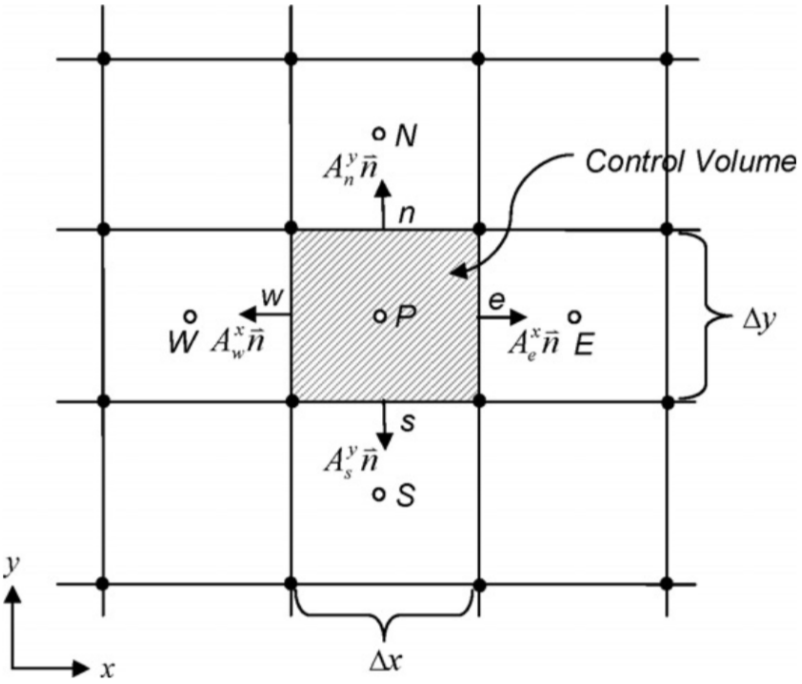

Figure 3.27: Convention and signs used for the application of differentiation schemes to the computational grid [57].

Spatial divergence the discretisation of divergence terms required particular attention, due to the instability of the corresponding convective fluxes. The divergence of velocity, associated to the bulk mass transport of momentum, was handled with a *linearUpwind grad(U)* scheme, which derives from a blend of the linear formulation with the upwind one, resulting in the following expression for the generic convective flux:

$$\boldsymbol{A}_e \cdot (\rho \boldsymbol{U})_e \varphi_e = F_e \varphi_e \quad \text{with} \quad \varphi_e = \overbrace{\varphi_P}^{\text{upwind}} + \underbrace{\frac{1}{2}(\varphi_P - \varphi_W)}_{\text{linear}} \tag{3.53}$$

where W denotes the cell upstream of the one under consideration, while e the face shared with the downstream cell, as shown in figure 3.27. The result is a second order scheme which, although it has not the same accuracy of the linear one, is less prone to oscillation and instability.

For the terms associated to the convective transport of the turbulent variables k, ω the second order *limitedLinear 1* scheme [45] was adopted, which exploits a Sweby limiter function ψ(r) [55] to bound the flux linear component in regions of rapidly changing gradient, according to the following expression:

$$\varphi_e = \varphi_P + \psi(r) \cdot \frac{\varphi_E - \varphi_P}{2} \quad \text{with} \quad r = \frac{\varphi_P - \varphi_W}{\varphi_E - \varphi_P} \tag{3.54}$$

where E denotes the cell downstream of the one under consideration. The severity of the limiting action is tuned via a proper coefficient ranging from 0 to 1; in this case, due to the tendency to divergence presented by the turbulent quantities, the maximum limiting, corresponding to a value of 1, was adopted.

Spatial laplacian The laplacian terms associated to the diffusive transport of momentum were handled with a *linear uncorrected* scheme, resulting in the following expression for the generic diffusive flux:

$$(\rho\Gamma)_e \boldsymbol{A}_e \cdot (\nabla\varphi)_e = (\rho\Gamma)_e |\boldsymbol{A}_e| \cdot \frac{\varphi_E - \varphi_P}{|\boldsymbol{d}|} \tag{3.55}$$

The diffusion coefficient at the cell face Γ_e is linearly interpolated from the corresponding values at cells centres, while the surface normal gradient term $\mathbf{A}_\mathrm{e} \cdot (\nabla\varphi)_\mathrm{e}$ is evaluated adopting a first order finite difference derivation strategy. Thanks to the uniform and orthogonal mesh allowed by the ACL method in the turbine region, no correction for the non-orthogonality between the cell surface $\mathbf{A}$ and the vector $\mathbf{d}$, connecting the centres of cells P and E, was required, raising the adopted scheme accuracy up to second order and improving the stability of the simulation.

Chapter 4

Results

In this chapter, the most relevant results of the validation campaign are presented. All simulations were run with the same rotational speed of the machine ($\Omega = 400$ rpm), shifting from one operating condition to the other by changing the freestream wind velocity (U_0=6-15 m/s).

For each one of them, a temporal resolution of 500 time steps per revolution was considered to be sufficient to resolve all relevant flow features and ensure simulation stability, while the number of revolutions required to achieve periodic convergence varied with the TSR between 10 and 25; as convergence index in particular, the percent deviation between the mean torque coefficients over two subsequent revolutions was adopted, considering a threshold of 1%.

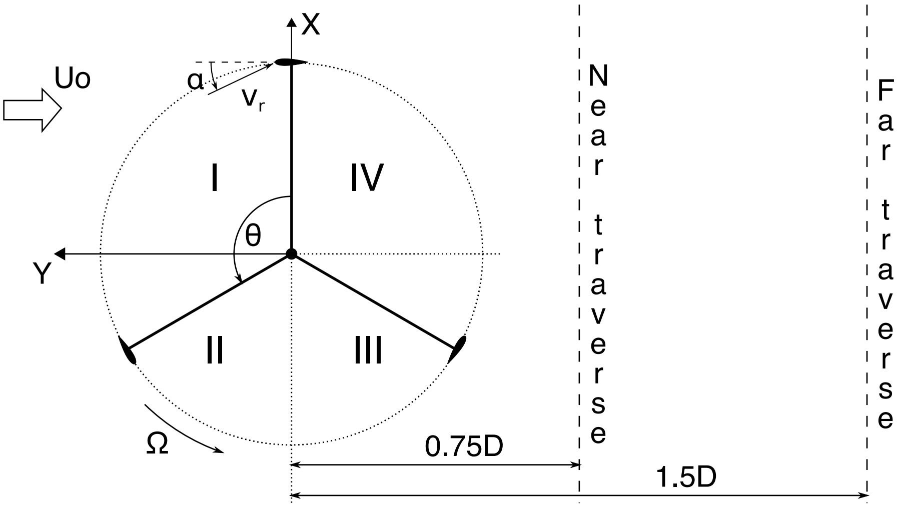

Figure 4.1: Signs and conventions used for the analysis.

4.1 Wake analysis

The time-mean profiles of the wake released by the machine, coming from ACL simulations, were validated against available experimental data (see chapter 2).

Such operation allowed to understand not only the suitability of the ACL solver to simulate the complex turbine-environment interaction associated to urban applications, but also its capability to reproduce the great variety of flow patterns experienced by the machine during its operation, which exert a strong influence on the predicted wake shape. In such perspective, the analysis focused on three benchmark operating conditions, considered to be representative of the turbine behaviour over its whole operative range: a high (TSR=3.3), optimal (TSR=2.5) and low loading one (TSR=1.5).

The comparison was carried out choosing as main reference parameter the wake *velocity defect* U/U_0, defined as the ratio between the arithmetic average of the local flow velocity U and the freestream one U_0:

$$U/U_0 = \frac{1}{U_0} \cdot \frac{1}{\tau} \int_{\tau} U(t)dt \tag{4.1}$$

where τ is the turbine revolution period. For the analysis of the high shear structures developing around the turbine instead, the same averaging procedure was applied to the *vorticity* field $\boldsymbol{\omega}$, i.e. the curl of the velocity vector:

$$\boldsymbol{\omega} = \nabla \times \boldsymbol{U} \tag{4.2}$$

Such approach was further refined for the identification of the vortexes characterising the wake flow pattern in the tip region, by projecting the vorticity vector along the mean flow direction:

$$\omega_s = \frac{\boldsymbol{\omega} \cdot \boldsymbol{U}}{|\boldsymbol{U}|} \tag{4.3}$$

This quantity, which takes the name of *streamwise vorticity* or helicity, is an useful indicator of the influence of the considered vortex-like structure over the global flow development and, by extension, of its strength and size.

4.1.1 Equatorial region

In the midspan region, where the flow field is dominated by the vorticity shed by the single blades due to elevated aerodynamic loading [3], the code is able to reproduce with a relatively high fidelity the wake temporal and spatial development; accuracy of the prediction in particular increases going towards higher TSRs, as reported in figure 4.8.

At low tip-speed ratios, the wake extension is limited to the turbine front section due to the relatively low blockage effect offered by the machine, as evident from figure 4.4. The combination of large angle of attack and low relative speed in the II quadrant results in fact in the onset of dynamic stall (see section 3.1.5), with corresponding significant drop in blade aerodynamic efficiency $\mathrm{C_L}/\mathrm{C_D}$; for this reason, the maximum velocity defect is shifted towards the I quadrant, where the flow is more stable, ending up in a substantial asymmetry of the wake, progressively reducing downstream [17]. As it can be seen from figures 4.8a and 4.8b, all these features are well captured by the ACL simulations, even though the degree of asymmetry of the wake is underestimated with respect to the experimental case; this issue has probably among the main reasons the inability of the solver to mimic the LE vortex shedding event typical of dynamic stall.

As the aerodynamic load on the blade, i.e. the tip-speed ratio, is increased, the blockage exerted by the turbine on the incoming flow becomes more and more

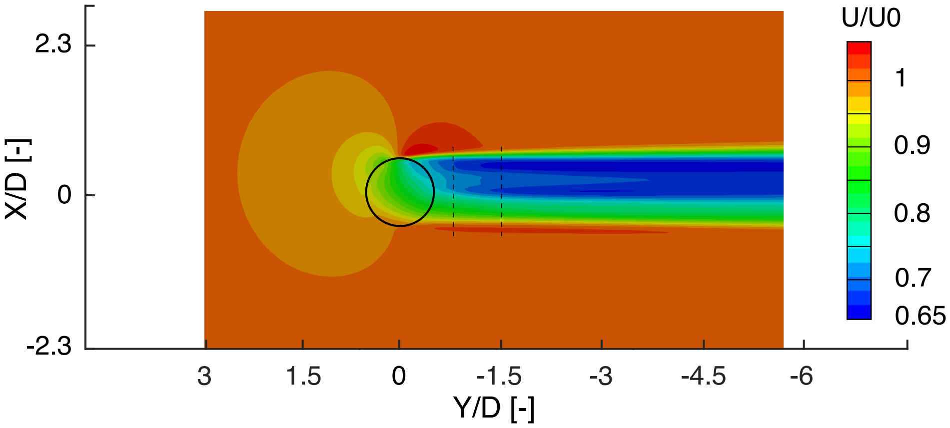

(a) TSR=1.5

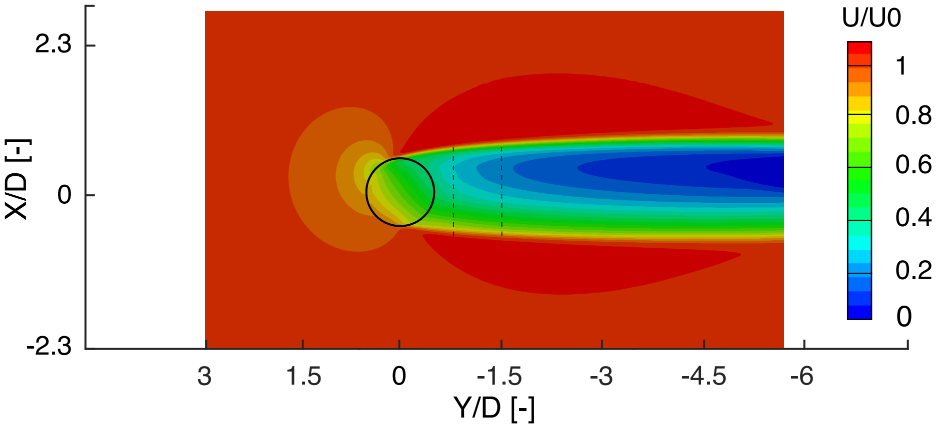

(b) TSR=2.5

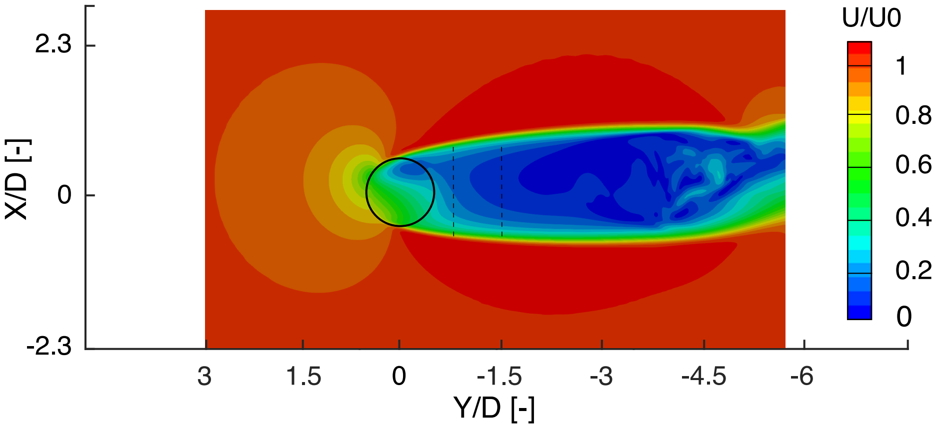

(c) TSR=3.3

Figure 4.2: Time-mean turbine wake velocity defect field on the equatorial plane (Z/H=0), obtained with the ACL solver with flow curvature correction only, for different loading conditions. Position of the measurement traverses is identified by the dotted lines.

relevant, as reported in figure 4.2. Upstream of the machine (0 <Y/D< 3), such phenomenon is highlighted by the enhancement of the flow potential deceleration, with a reduction of the freestream velocity up to 40% in proximity of the rotor for TSR=3.3 (see fig. 4.2c); the latter is sided by a considerable deflection of the flow in the transversal direction, which can be noticed from the cardioid-like shape assumed by the velocity gradient region. The advancement of the process across the rotor leads to an enlargement of the wake, now extending well beyond the machine front section, which is further amplified by its development downstream; this pattern is clearly visible in figures 4.8f and 4.2c, where it can also be seen how it is followed by an over-speed ($U/U_0 > 1$) of the streamtubes surrounding the wake.

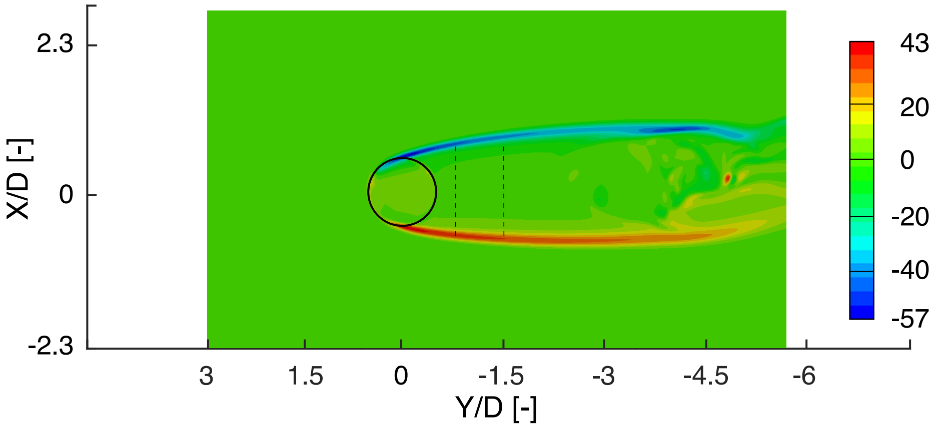

(a) Spanwise component of the vorticity vector ω_Z

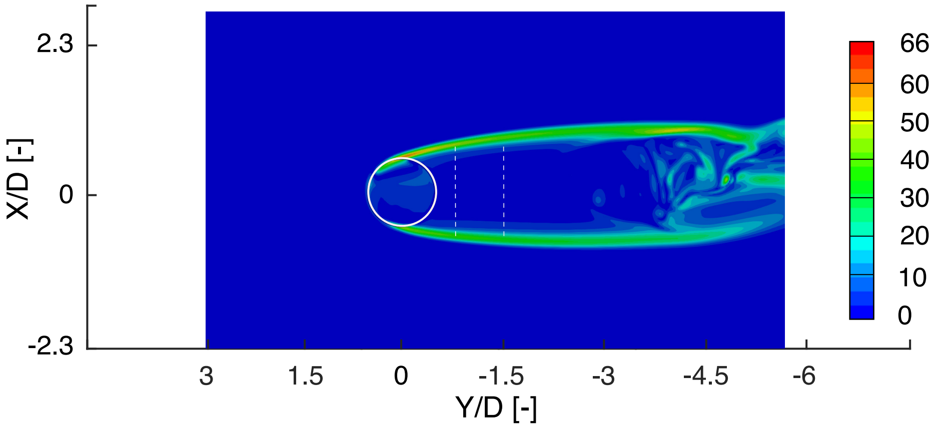

(b) Magnitude of the vorticity vector $\boldsymbol{\omega}$

Figure 4.3: Time-mean turbine wake vorticity field $\boldsymbol{\omega}$ [1/s] on the equatorial plane (Z/H=0), obtained with the ACL solver with flow curvature correction only, for TSR=3.3. Position of the measurement traverses is identified by the dotted lines.

The reduction in oscillation amplitude of both blade angle of attack and relative speed with respect to the lower TSRs minimizes in fact the influence of dynamic stall, allowing the establishment of a high lift condition in both I and II quadrants [17]; the maximum velocity defect zone is thus shifted towards the turbine axis and enhanced in both intensity and extension, leading to a nearly symmetrical wake configuration, with a wide region of stagnant flow. In such context, it is worth noticing the capability of the method to describe the development of the shear layers at the interface between the wake and the freestream, highlighted in figure 4.3a by the two peaks in the spanwise component of the vorticity vector ω_Z, and their successive evolution into the large recirculation zone found in the far wake. Beyond a certain blade loading in fact, the velocity gradient at the wake border becomes excessively severe, leading eventually to the unstable break-up and flow entrainment clearly visible in figure 4.3b from the three-dimensional configuration assumed by the vorticity field.

4.1.2 Tip region

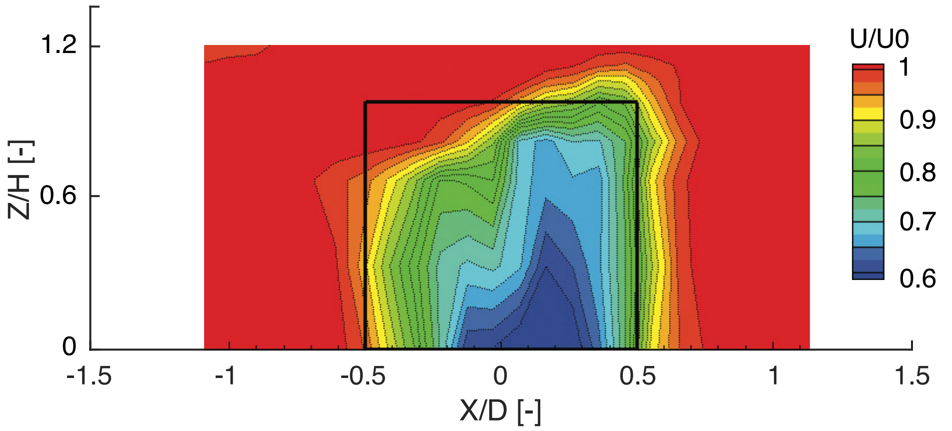

(a) Experimental velocity defect field

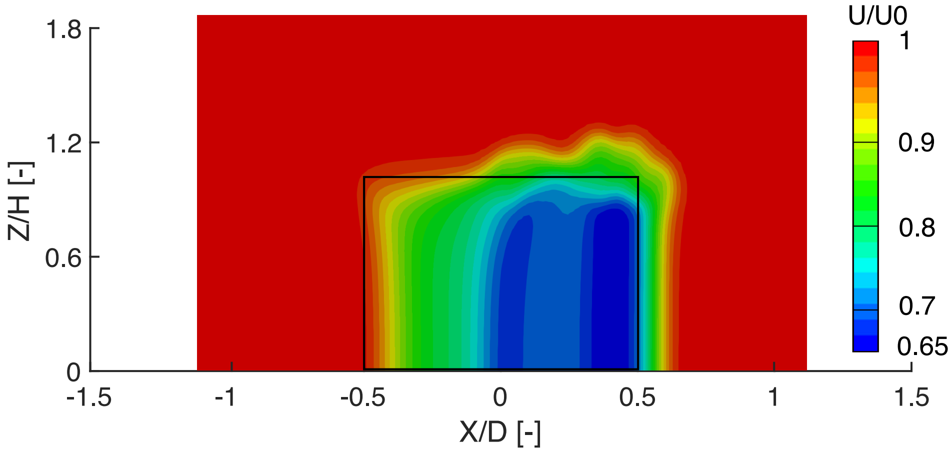

(b) Numerical velocity defect field

Figure 4.4: Comparison between the experimental and numerical time-mean velocity defect fields, obtained with the ACL solver with flow curvature correction only, for TSR=1.5. Reference plane is the far wake measurement traverse (Y/D=1.5).

Approaching the tip region, where the flow becomes fully three-dimensional and is dominated instead by the trailing vorticity released by the blade extremities

[3], the reliability of the code drops significantly; more in detail, the deviation between CFD simulations and experimental data increases going towards higher TSRs, where the establishment of a high load condition on most part of the turbine revolution amplifies the effects of the tip vortex-like structures described in section 3.1.6. As reported in figures 4.10 and 4.11, the ACL method is able on one hand to capture at least qualitatively the shape assumed by the wake, which is deformed by the presence of persistent tip vortexes generated in the upwind region (I and II quadrants), where the blade loading is much higher than in the downwind one (III and IV quadrants).

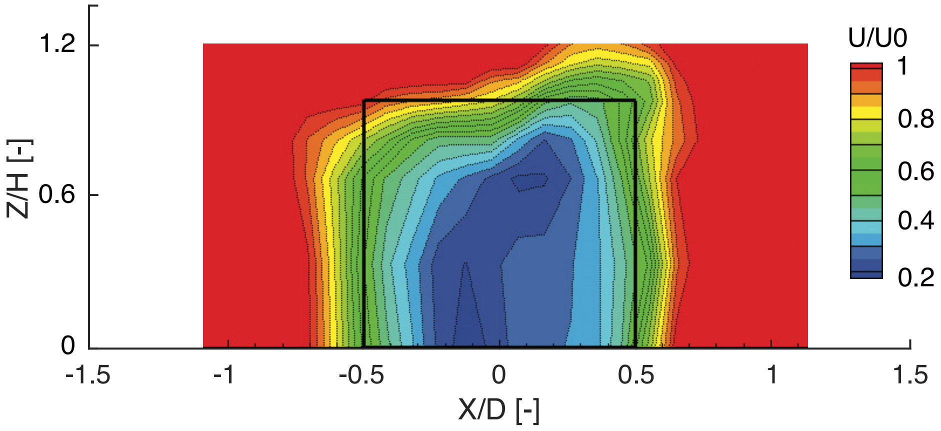

(a) Experimental velocity defect field

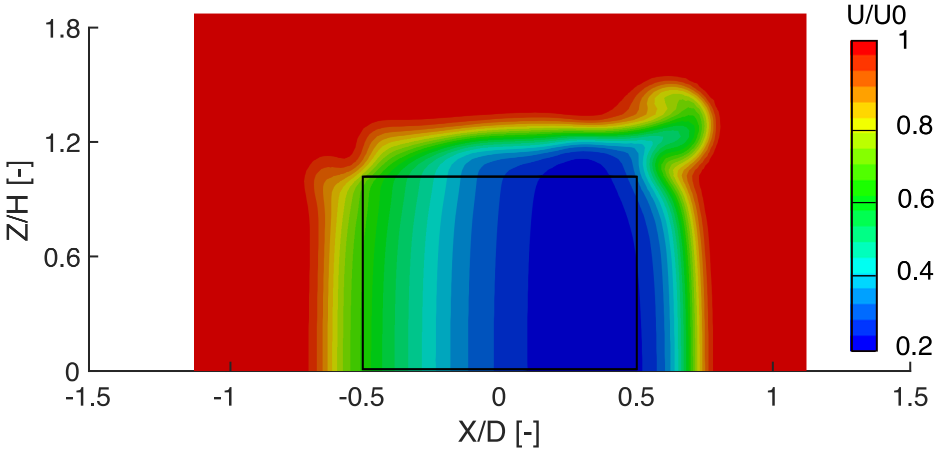

(b) Numerical velocity defect field

Figure 4.5: Comparison between the experimental and numerical time-mean velocity defect fields, obtained with the ACL solver with flow curvature correction only, for TSR=2.5. Reference plane is the far wake measurement traverse (Y/D=1.5).

On the other hand, the enhancement of wake deformation during its development downstream is completely ignored by the CFD simulations, which show a completely opposite trend.

At the highest tip-speed ratio, wake deformation is almost anti-symmetric with respect to the turbine axis, as reported in figures 4.11e and 4.11f; a strong vortex is shed from the blade tip in the I quadrant, inducing a strong deceleration of the downstream flow. The same phenomenon occurs in the II quadrant, although with lower magnitude and in the opposite direction, leading to a lower deceleration of the corresponding streamtube.

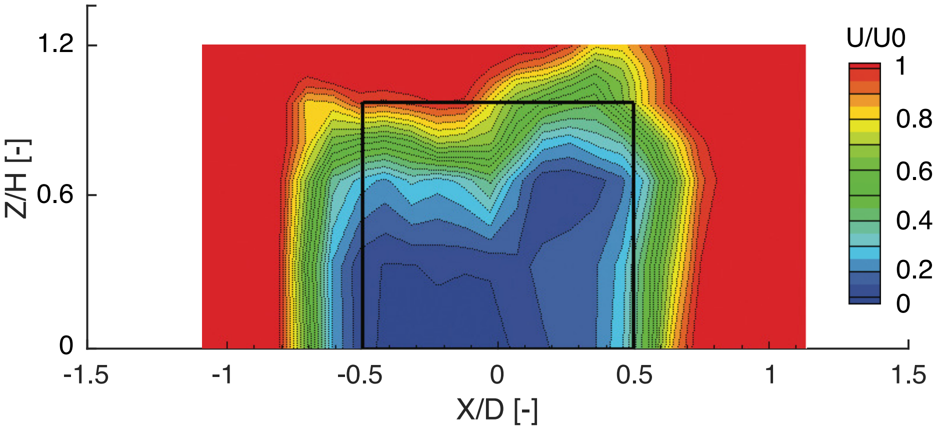

(a) Experimental velocity defect field

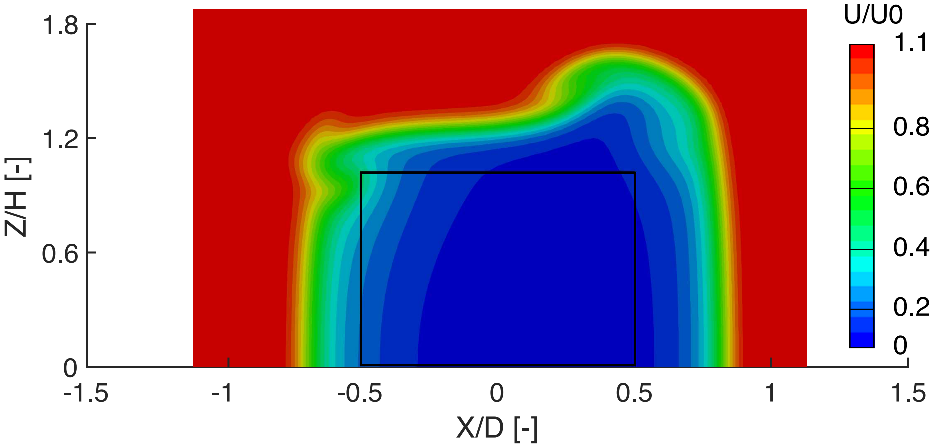

(b) Numerical velocity defect field

Figure 4.6: Comparison between the experimental and numerical time-mean velocity defect fields, obtained with the ACL solver with flow curvature correction only, for TSR=3.3. Reference plane is the far wake measurement traverse (Y/D=1.5).

Such configuration can also be found in figure 4.6, where the two counter-rotating tip vortexes are identified by the corresponding "crests" in the upper part of the wake. From the same picture it is also evident how the predicted velocity defect region extends in the spanwise direction much more than the experimental one, highlighting once again the inability of the code to correctly predict the tip vortexes strength and their interaction with the freestream; according to [3] in fact, the tip structures are responsible not only for the aforementioned wake deformation in the streamwise direction, but also for the entrainment of air into the rotor and the wake from their top and bottom sides, with consequent enhanced mixing with the undisturbed flow region.

Going towards lower TSRs, the strength of these flow structures, together with the corresponding wake deformation and flow entrainment, is damped out by the decreasing blade loading; such effect is particularly pronounced on the II quadrant tip vortex due to dynamic stall, leading to a substantial shift of the wake velocity defect towards the I quadrant and to an overall inclination of the upper wake border (see fig. 4.4). This trend is clearly visible in figure 4.7, where it can be observed how the high streamwise vorticity region tends to concentrate on the right-hand side of the turbine as the TSR shifts from 3.3 to 1.5.

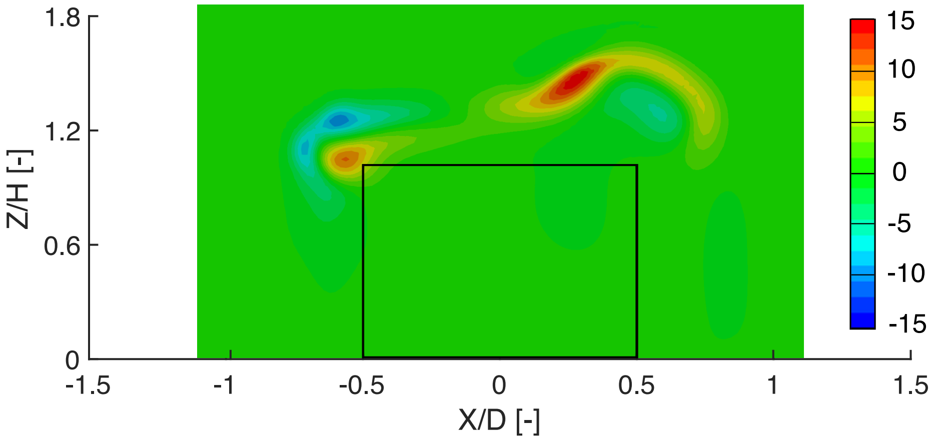

(a) TSR=3.3

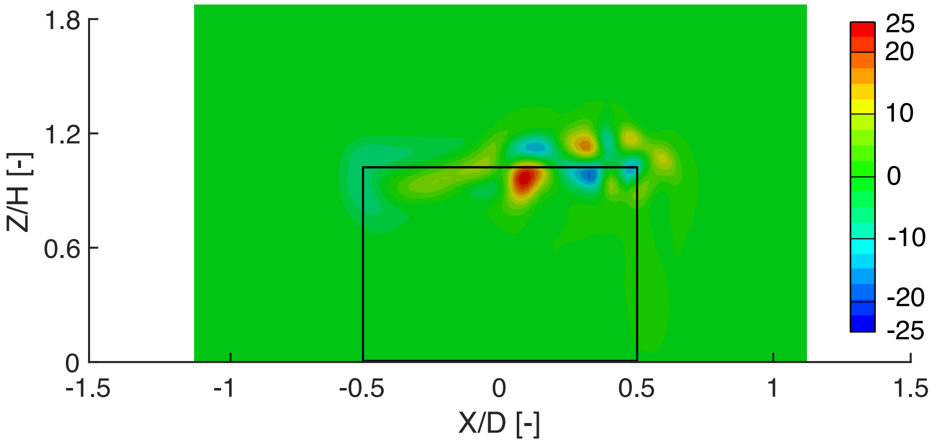

(b) TSR=1.5

Figure 4.7: Time-mean turbine wake streamwise vorticity fields ω_s [1/s], obtained with the ACL solver with flow curvature correction only, for different loading conditions. Reference plane is the far wake measurement traverse (Y/D=1.5).

To sum up, the code, although capable to capture the qualitative features of the tip region flow pattern, fails in the quantitative estimation of the tip vortex strength. Apparently, the flow pattern developing around VAWT blades and responsible for tip vortex generation, described in detail in section 3.1.6, cannot be accurately reproduced by the ACL approach, since it depends on the blade geometry details.

4.1.3 Effects of applied sub-models on turbine wake prediction

As anticipated in section 3.1.2, various sub-models were integrated in the ACL solver, in order to provide a more accurate description of the wind-turbine interaction; their effect on the computed wake velocity defect profiles turned out however to be in most cases marginal, as evident from figures 4.8, 4.9, 4.10 and 4.11.

The strongest variation in terms of predicted wake shape with respect to the base model, i.e. the ACL with the polars of the symmetrical NACA0021 airfoil (see fig. 3.18a and 3.18c), is given by the flow curvature correction, whose implementation is reported in section 3.1.4; while negligible at the lower tip-speed ratios, its weight increases going towards higher loading cases, where the curvature of the streamlines encountered by the rotating blades is more marked (see fig. 4.8). In such context, it can be seen how its effects on the quality of the results are contrasting. In the equatorial region, the prediction of the maximum velocity defect in the wake is improved, leading to a nearly perfect correspondence between ACL and experimental data in the leeward region ($X/D < 0$), as reported in figures 4.8e and 4.8f; in the windward one ($X/D > 0$) however, a significant error is introduced in the localisation of the wake border, which is shifted towards the right with respect to the experimental one. The same asymmetrical pattern can be also observed in the tip region, where it leads to a better approximation of the shape of the wake in proximity of the turbine (fig. 4.11e); this improvement however is not observed in the far traverse (see fig. 4.8f), further demonstrating the inability of the adopted simulation tool to capture the tip vortex structures.

The Berg dynamic stall model shows instead limited effect on the predicted time-mean wake configuration, both with $\mathrm{A_M}$=6 and $\mathrm{A_M}$=20; more in detail, the corresponding wake profile presents characteristics which are intermediate between the ones related the ACL base configuration and to flow curvature correction.

Even smaller, up to the point to be negligible, is the impact of the Glauert correction for end effects. This fact is quite surprising, considering how severely such sub-model alters the aerodynamic force distribution along the blade span, and confirms the need of more detailed studies about its implementation.

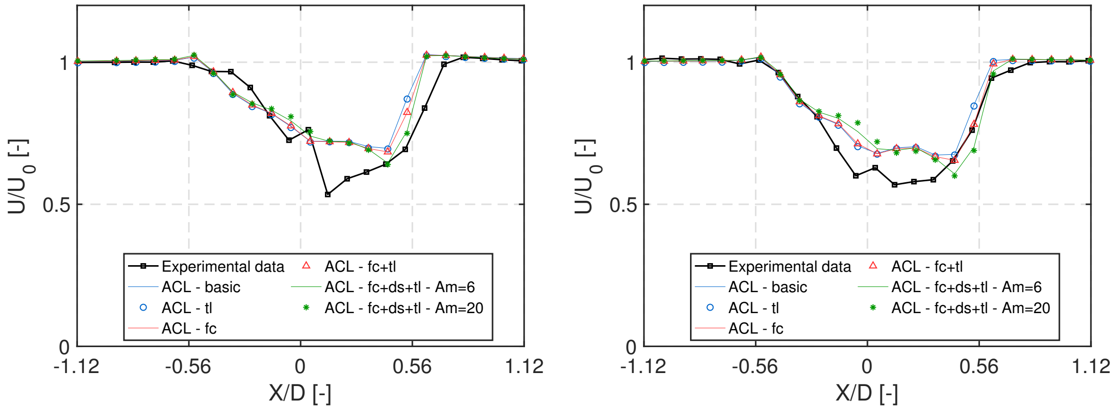

(a) TSR=1.5, near traverse **(b)** TSR=1.5, far traverse

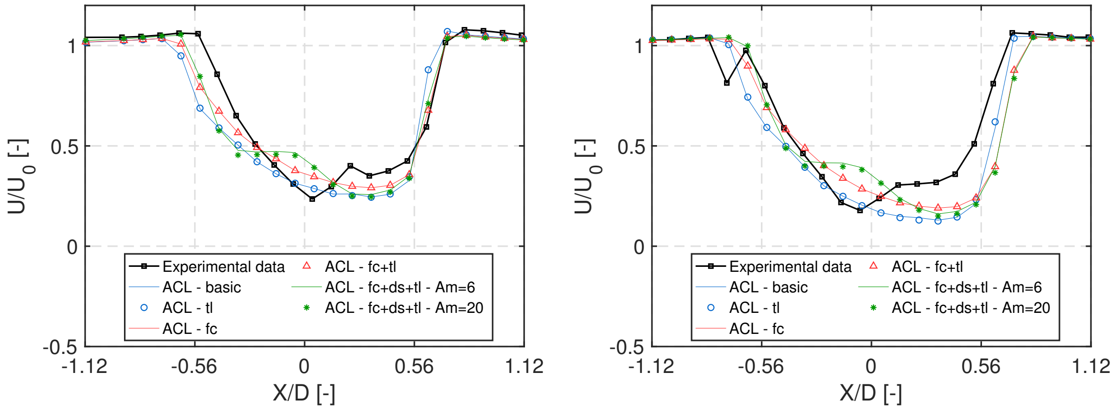

(c) TSR=2.5, near traverse **(d)** TSR=2.5, far traverse

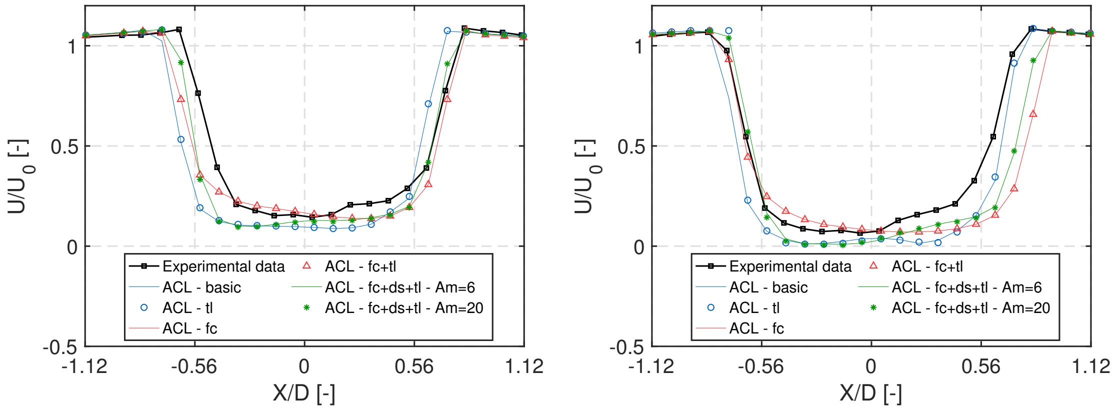

(e) TSR=3.3, near traverse **(f)** TSR=3.3, far traverse

Figure 4.8: Time-mean turbine wake velocity defect profile on the equatorial plane (Z/H=0) for different loading conditions and combinations of the following sub-models: fc=Migliore flow curvature correction, ds= Berg dynamic stall model, tl=Glauert tip loss correction.

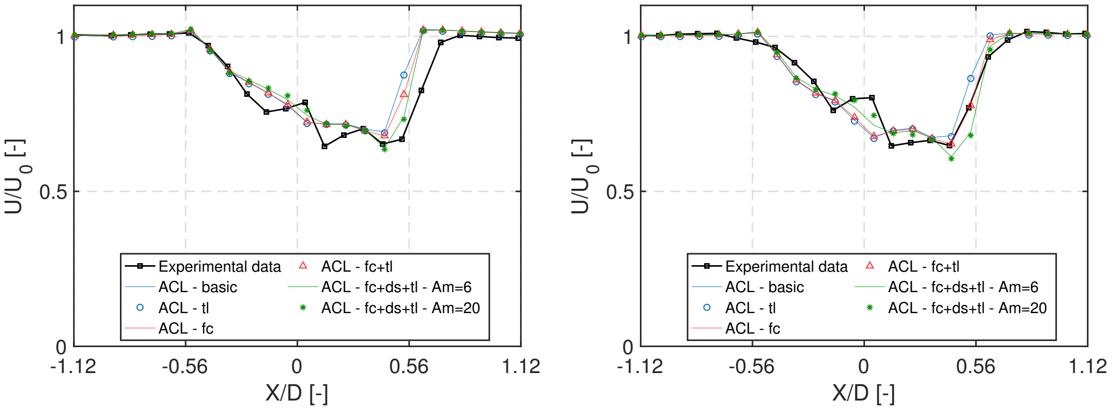

(a) TSR=1.5, near traverse **(b)** TSR=1.5, far traverse

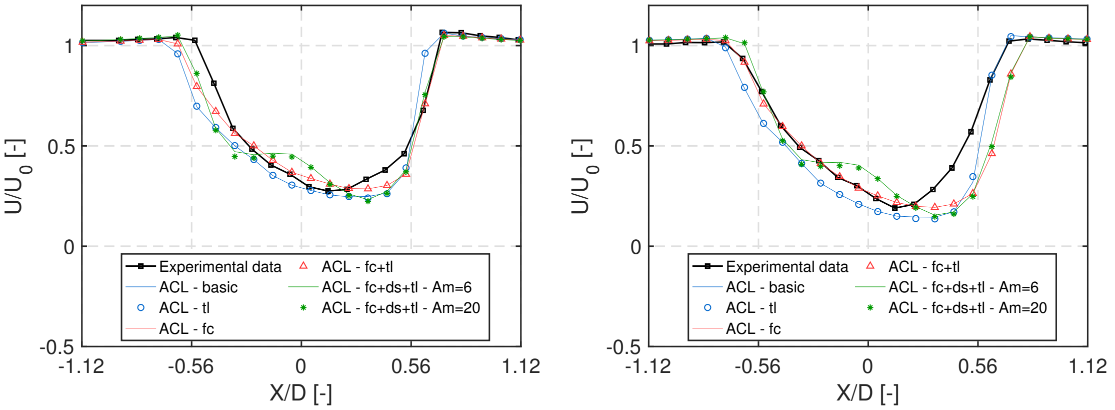

(c) TSR=2.5, near traverse **(d)** TSR=2.5, far traverse

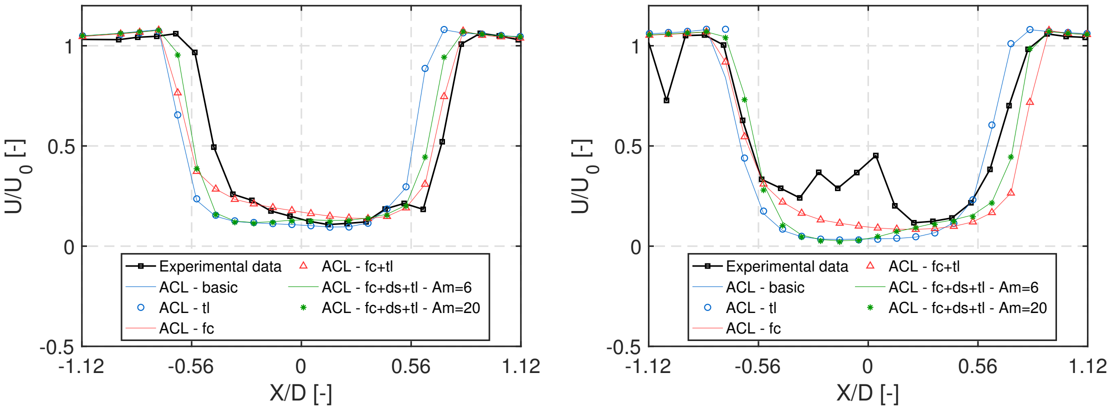

(e) TSR=3.3, near traverse **(f)** TSR=3.3, far traverse

Figure 4.9: Time-mean turbine wake velocity defect profile in the upper blade region (Z/H=0.6) for different loading conditions and combinations of the following sub-models: fc=Migliore flow curvature correction, ds= Berg dynamic stall model, tl=Glauert tip loss correction.

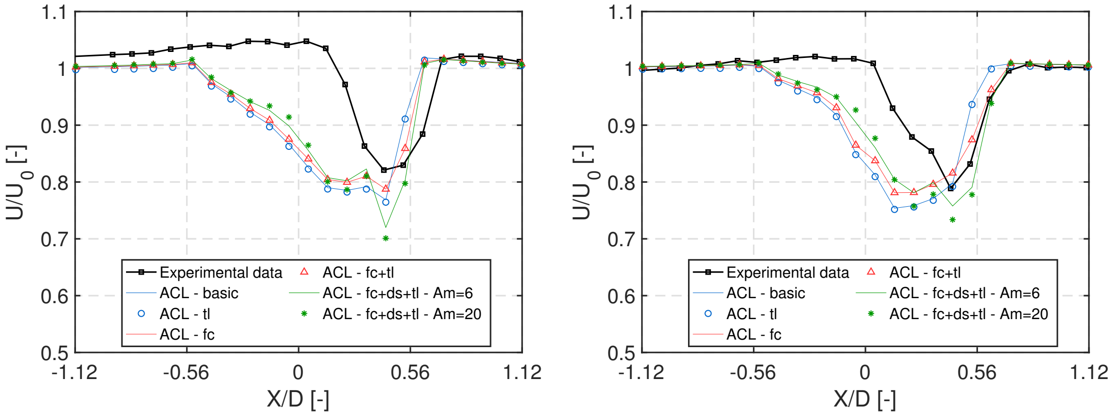

(a) TSR=1.5, near traverse **(b)** TSR=1.5, far traverse

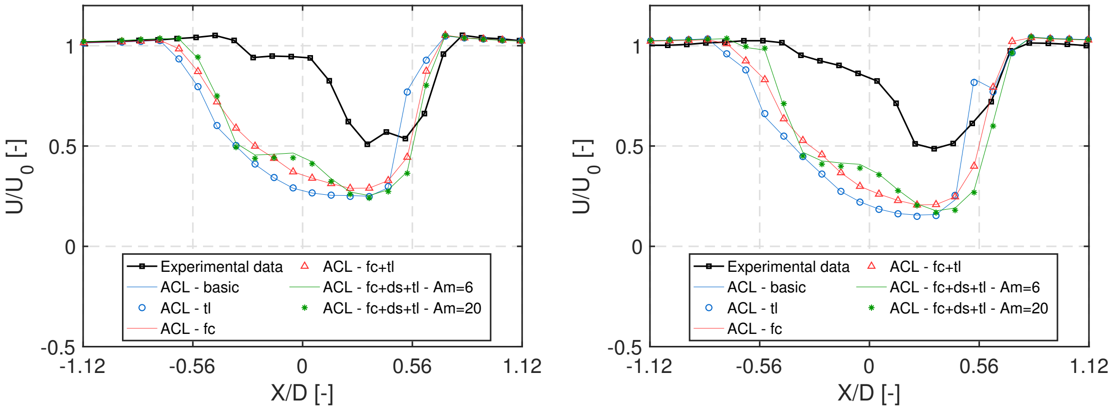

(c) TSR=2.5, near traverse **(d)** TSR=2.5, far traverse

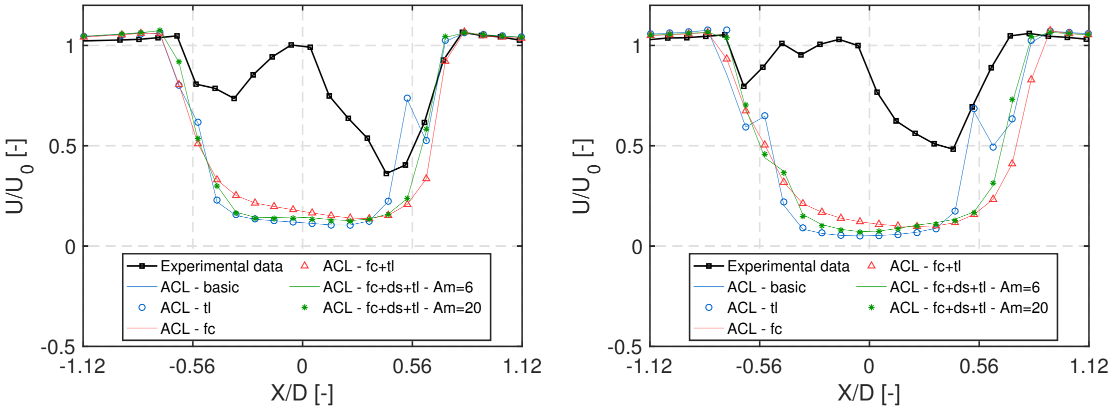

(e) TSR=3.3, near traverse **(f)** TSR=3.3, far traverse

Figure 4.10: Time-mean turbine wake velocity defect profile on the tip plane (Z/H=1) for different loading conditions and combinations of the following sub-models: fc=Migliore flow curvature correction, ds= Berg dynamic stall model, tl=Glauert tip loss correction.

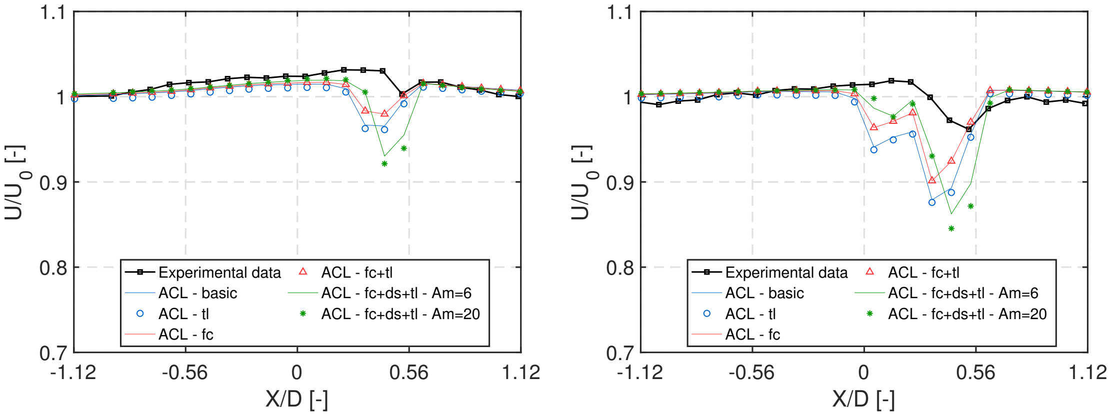

(a) TSR=1.5, near traverse **(b)** TSR=1.5, far traverse

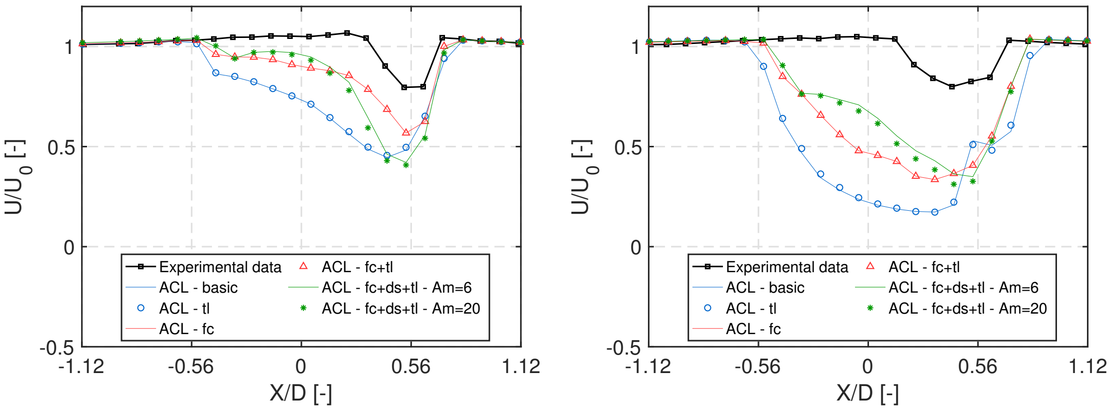

(c) TSR=2.5, near traverse **(d)** TSR=2.5, far traverse

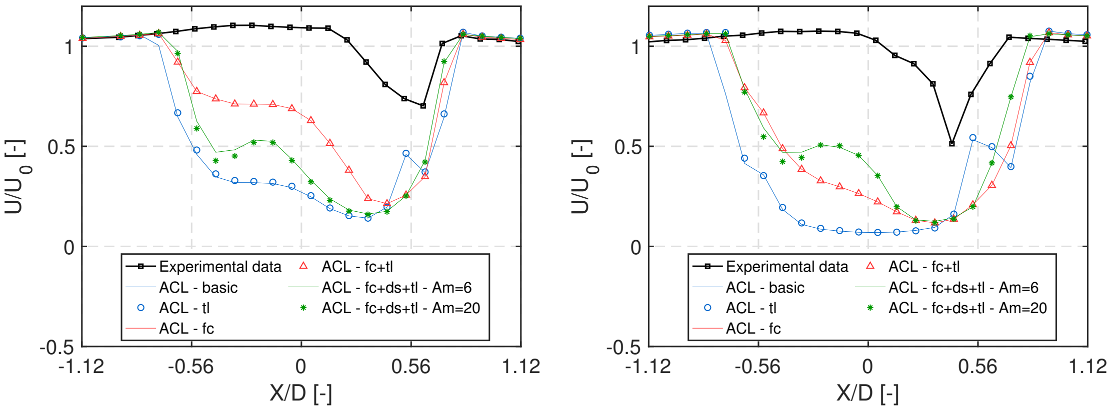

(e) TSR=3.3, near traverse **(f)** TSR=3.3, far traverse

Figure 4.11: Time-mean turbine wake velocity defect profile on the far tip plane (Z/H=1.15) for different loading conditions and combinations of the following sub-models: fc=Migliore flow curvature correction, ds= Berg dynamic stall model, tl=Glauert tip loss correction.

4.2 Performance analysis

The turbine performance data coming from ACL simulations, expressed in terms of average power and thrust coefficients characteristic curves, were validated against their experimental counterparts. The C_P curve in particular was brought to the comparison after the application of a proper correction for the drag losses associated to the presence of the support arms connecting the blades to the central shaft [12]; as a matter of fact, these structures are not included in the ACL model of the turbine. The validation process allowed to understand the capability of the code to accurately describe the wind-turbine interaction and, as a consequence, its suitability for the aerodynamic design of these machines.

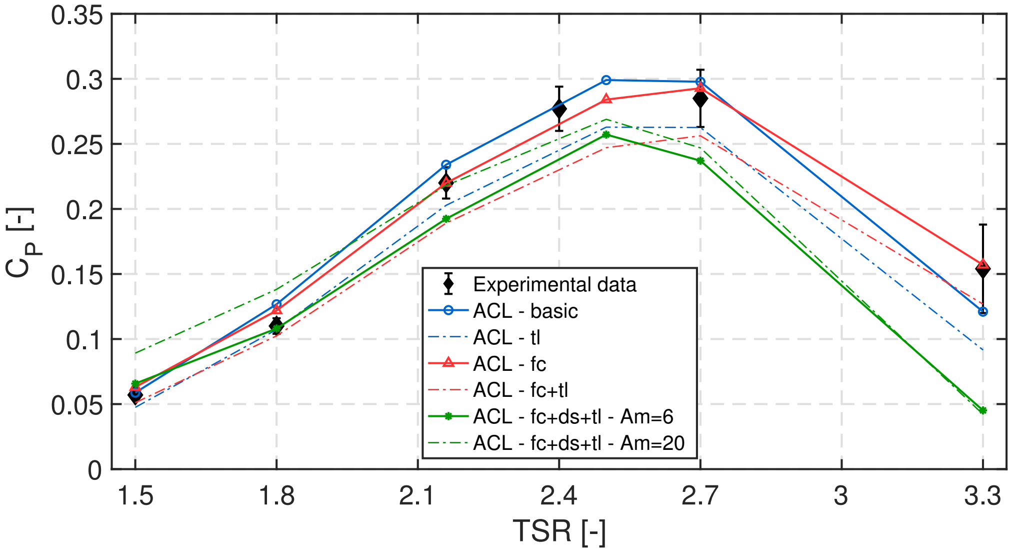

Figure 4.12: Comparison between experimental and predicted average turbine power coefficient for different tip-speed ratios and combinations of the following sub-models: fc=Migliore flow curvature correction, ds= Berg dynamic stall model, tl=Glauert tip loss correction.

As reported in figure 4.12, the adopted simulation tool reproduces with high fidelity the experimental C_P-TSR curve, except for a small discrepancy around TSR=1.8. The highest degree of correspondence is achieved in particular with the application of the only flow curvature correction, confirming its importance in the modelling of small VAWTs, while a substantial degradation of the solver accuracy is observed when the dynamic stall and tip loss models are added, especially at the higher TSRs.

On the contrary, a relatively large deviation between simulations and experimental data is observed for the C_X curve, particularly evident at the lower TSRs (see fig. 4.13); such discrepancy is probably related to the absence in the ACL model of the turbine shaft and support arms, which represent a relevant source of drag for the machine [2].

In order to gain a deeper understanding of the shape assumed by the performance curves and so of the global turbine behaviour, various aerodynamic quantities of interest are reported in figures 4.14, 4.15 and 4.16, for the three TSRs chosen as benchmarks for the current analysis.

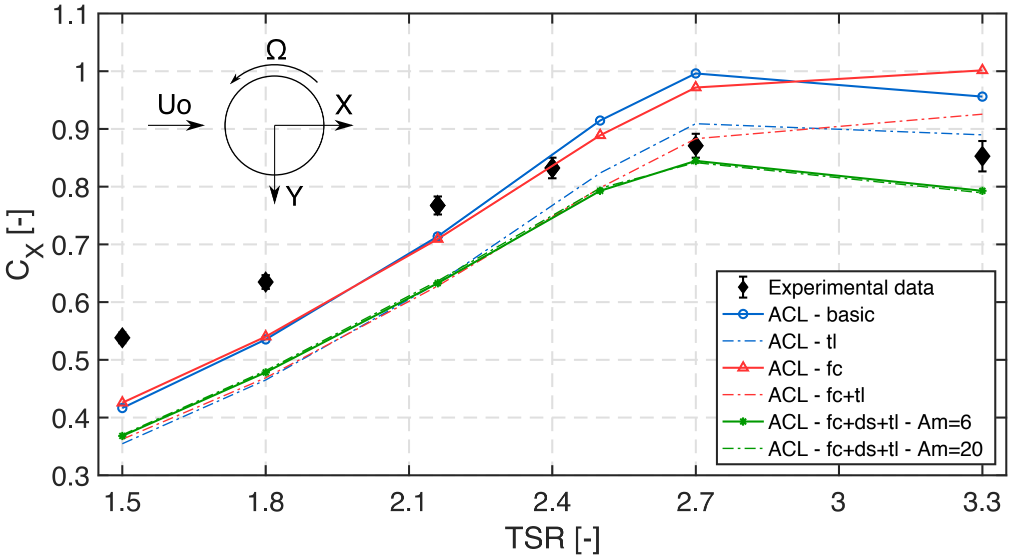

Figure 4.13: Comparison between experimental and predicted average turbine thrust coefficient for different tip-speed ratios and combinations of the following sub-models: fc=Migliore flow curvature correction, ds= Berg dynamic stall model, tl=Glauert tip loss correction.

At the lower tip-speed ratios, power extraction is severely penalised by the dynamic stall event occurring for most part of the revolution due to the large oscillation in the AOA, with a steep reduction in the blade efficiency C_L/C_D (see fig. 4.14). Thanks to the corresponding low blockage effect, the behaviour of the machine is nearly symmetric between the upwind (I+II quadrant) and downwind regions (III+IV), apart from the hysteresis in the force exchange associated to flow unsteadiness and highlighted in figures 4.14c and 4.14d.

As the tip-speed ratio is increased, turbine operation is progressively stabilised, with reduced oscillation of all flow quantities (see fig. 4.15 and 4.16). In fact, due to the global mitigation of dynamic stall effects and the consequent improvement of the blades aerodynamic efficiency, a high lift condition is established on a growing portion of the turbine revolution; such trend is particularly evident in the upwind region, where the peak torque production zone tends to assume a nearly symmetric configuration, centred in $\vartheta = 90°$ and covering the whole range between $\vartheta = 45°$ and $\vartheta = 135°$ (see fig. 4.16b). If on one side this phenomenon enhances power extraction, raising the average power coefficient, on the other side nonetheless amplifies the blockage induced by the turbine on the incoming flow (see fig. 4.13), penalising the machine global performance; as a matter of fact, flow deceleration in the upwind region determines a decrease in the relative velocity magnitude and angle of attack seen by the blades in the downwind one, causing a strong asymmetry of the global torque profile over a revolution, as reported in figure 4.16b. The latter effect is partially mitigated by the deflection of the incoming flow in the cross-wise direction, which results in a positive offset of the AOA profile, particularly evident for $\vartheta = 0°$ (see fig. 4.16a).

The final result of the combination of these two opposite trends is the C_P-TSR curve shown in figure 4.12; the power coefficient reaches its peak at TSR=2.5, where the proper balancing of all these aspects is reached, for then decreasing due to the excessive weight of flow blockage over the global turbine behaviour.

4.2.1 Effects of applied sub-models on turbine performance prediction

In contrast with the development of the wake (see section 4.1), predicted turbine performances are quite sensitive to the applied sub-models, which exert a strong influence on the exchange of forces between the wind and the blades and so on the global blade torque profile.

In such perspective, a relevant contribution comes from the adoption of the flow curvature correction, whose weight, while negligible at the lower tip-speed ratios, increases going towards the higher loading cases, where the curvature of the streamlines encountered by the rotating blades is more marked.

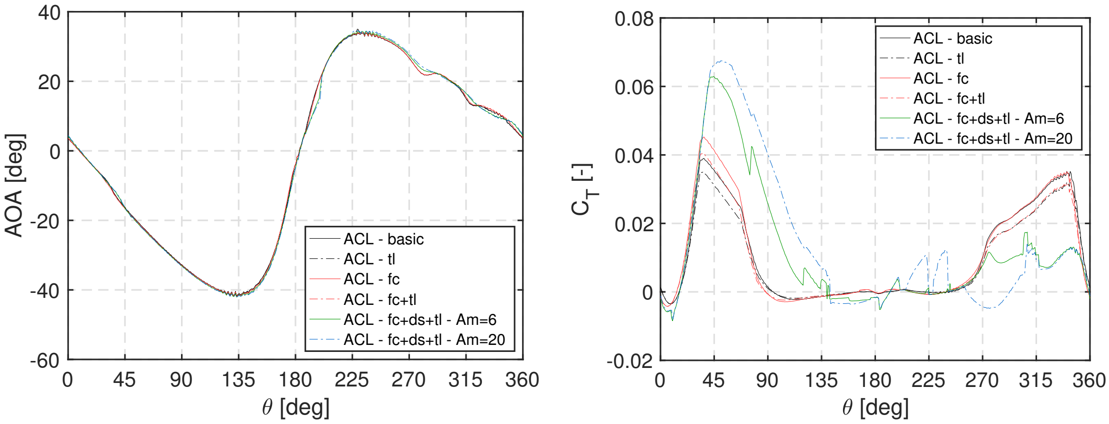

(a) Angle of attack **(b)** Torque coefficient

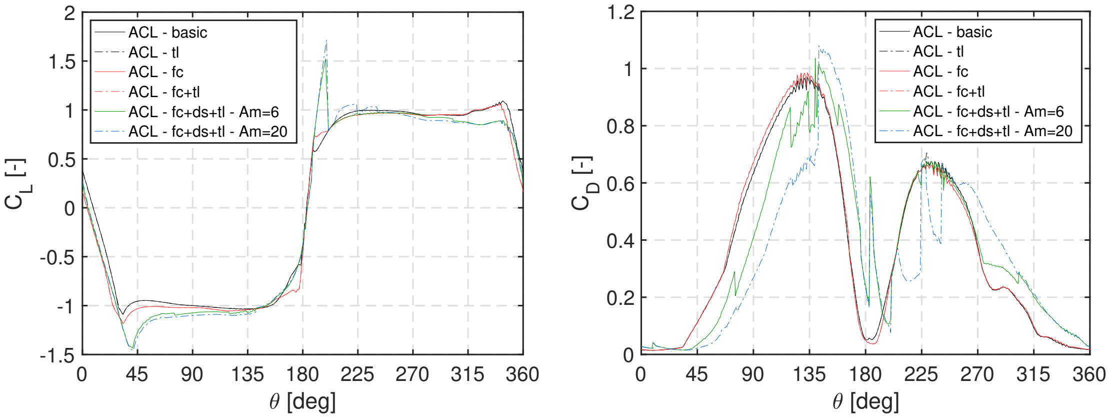

(c) Lift coefficient **(d)** Drag coefficient

Figure 4.14: Profiles over a single blade revolution of various aerodynamic quantities of interest, for TSR=1.5 and different combinations of the following sub-models: fc=Migliore flow curvature correction, ds= Berg dynamic stall model, tl=Glauert tip loss correction.

As it can be seen from figures 4.15c and 4.16c, its main effect is the amplification of the asymmetry in the performance between the front and rear parts of the turbine;

as a matter of fact, blade loading is enhanced in the upwind region, while penalised in the downwind one. The consequences of this phenomenon on the turbine efficiency are somewhat contrasting and depends on the considered operating conditions; in the optimal loading case, i.e. around TSR=2.5, the downwind performance penalty dominates over their upwind enhancement, leading to a global power coefficient reduction (see fig. 4.12). The opposite trend is encountered in the high loading branch of the C_P curve, with a corresponding increase in efficiency with respect to the base model. In this context, the enhanced blade loading in the upwind region strengthens the blockage exerted by the turbine on the crossing flow, promoting an increment in the global thrust coefficient (see fig. 4.13) and in the oscillation of all flow quantities, in particular of the angle of attack (see fig. 4.16a).

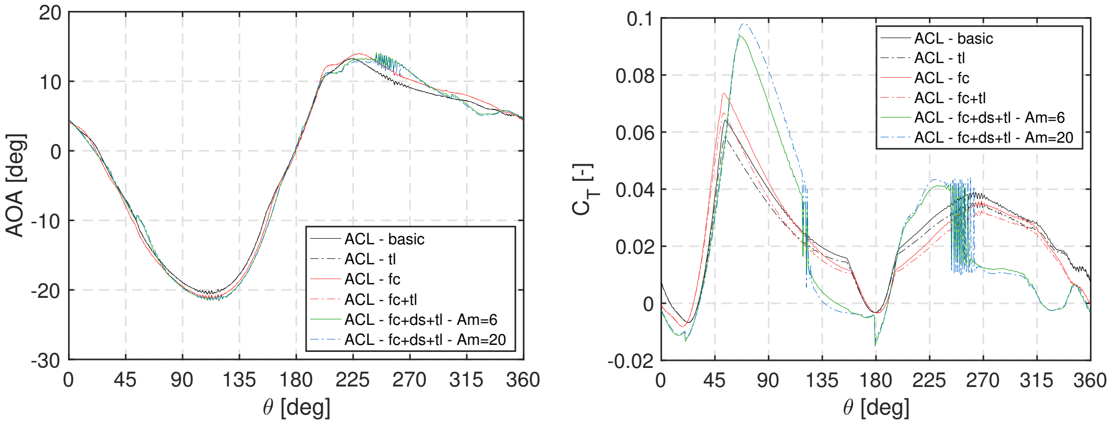

(a) Angle of attack **(b)** Torque coefficient

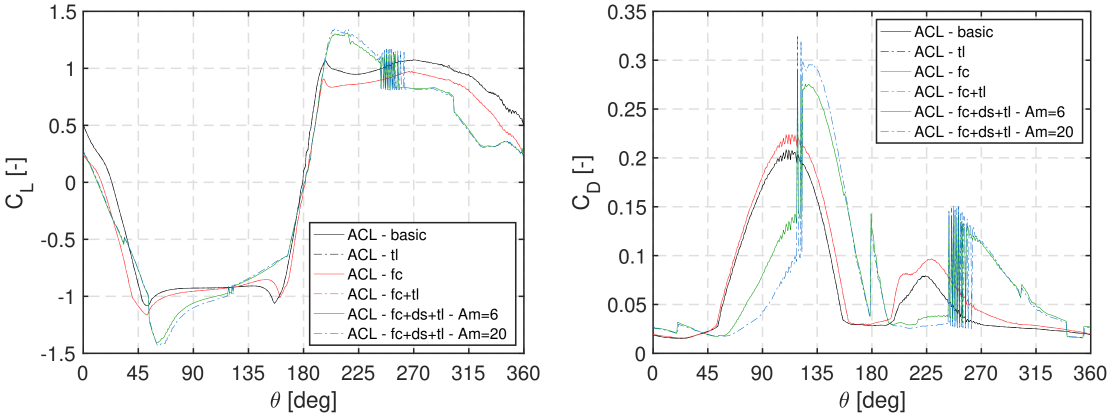

(c) Lift coefficient **(d)** Drag coefficient

Figure 4.15: Profiles over a single blade revolution of various aerodynamic quantities of interest, for TSR=2.5 and different combinations of the following sub-models: fc=Migliore flow curvature correction, ds= Berg dynamic stall model, tl=Glauert tip loss correction.

The addition of the Berg dynamic stall model further modifies the predicted blade torque profile, replacing the aerodynamic coefficients C_L, C_D with their dynamic counterparts; the latter show a marked hysteretic behaviour, which becomes more and more relevant going towards the low TSRs. At the lower tip-speed ratios, the aforementioned hysteresis is reflected on a strong asymmetry in the torque production between the upwind and the downwind regions, with a peak in the torque coefficient C_T much higher than in the static case (see fig. 4.14b). Such phenomenon results in an overestimation of the C_P, particularly pronounced for A_M=20, when combined with the absence of losses related to LE vortexes shedding and transport along the flow domain; this fact is evident from figure 4.14a, where it can be seen how the adopted model has small or negligible effect on the predicted AOA profile. The same behaviour can be found approaching the optimal operating condition, while for higher TSRs, the dynamic stall correction tends to distort the predicted torque profile, as shown in figure 4.16b; as a matter of fact, the large hysteresis cycle in the upwind region, whose amplitude is probably overestimated with respect to the real case, induces a wide valley in the angle of attack in the downwind one, between $\vartheta = 180°$ and $\vartheta = 315°$, leading to a local performance drop. The global effect is a significant underestimation of the average power and thrust coefficients with respect to the experimental ones.

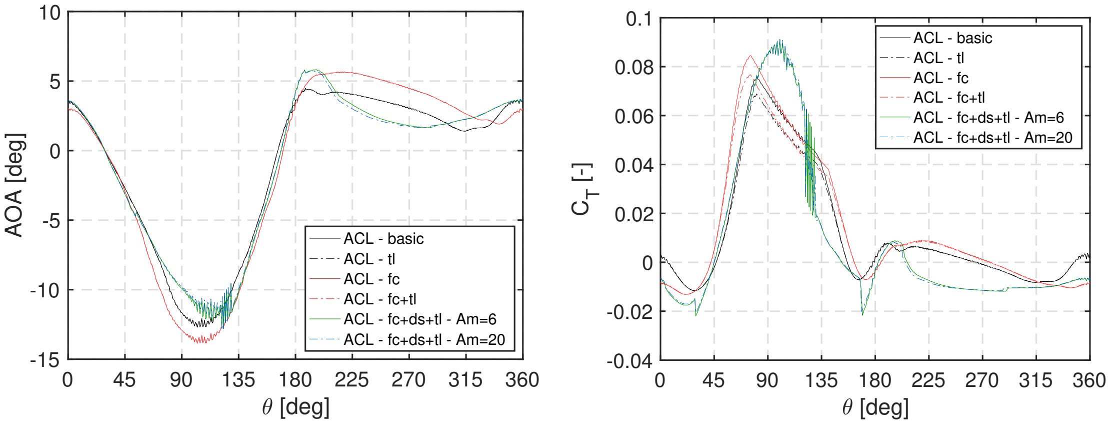

(a) Angle of attack **(b)** Torque coefficient

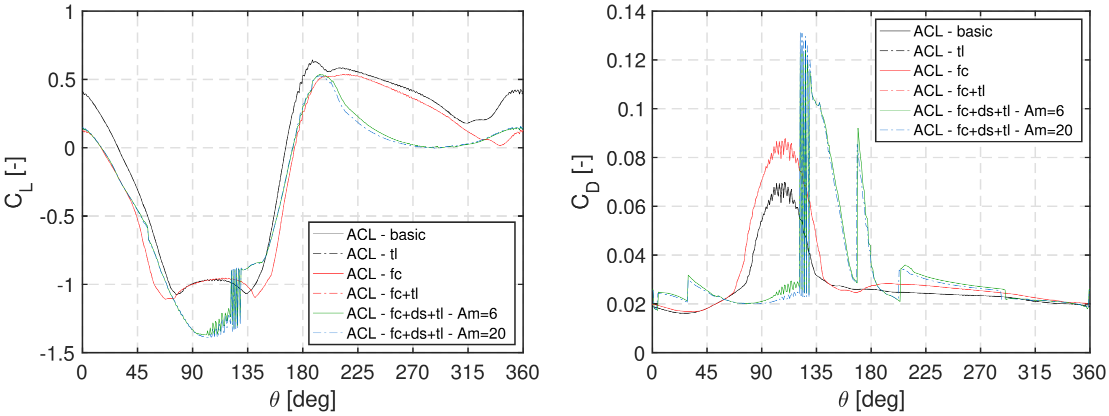

(c) Lift coefficient **(d)** Drag coefficient

Figure 4.16: Profiles over a single blade revolution of various aerodynamic quantities of interest, for TSR=3.3 and different combinations of the following sub-models: fc=Migliore flow curvature correction, ds= Berg dynamic stall model, tl=Glauert tip loss correction.

The final sub-model employed in the frame of the current work is the Glauert correction for end effects, which results essentially in an offset of the blade torque profile in maximum lift condition, i.e. in the upwind region. As evident from figures 4.12 and 4.13, this model tends to overestimate the weight of tip losses over whole range of operation of the turbine, introducing a significant discrepancy between the ACL and the experimental curves.

Conclusions and Future Works

This thesis has shown that the Actuator Line Method has the potential to become a reliable tool for the design and study of VAWTs, when supported by an accurate aerodynamic database and a proper set of corrective sub-models.

The agreement between predicted and experimental wake shape is globally very good, even though the quality of the results decreases approaching the blade tip, where the flow field is fully dominated by 3D effects; in that region nonetheless, the model is still able to reproduce qualitatively the most relevant features.

Turbine performance on the other hand, in particular the variation of the power coefficient with the tip-speed ratio, are reproduced with high accuracy by the code, although it requires an additional correction in the post-processing phase to account for struts-related drag losses; this issue however can be easily solved by integrating the support structures in the ACL model of the turbine. Their implementation, together with the one of the central shaft, may also compensate the relatively large deviation between simulations and experimental data observed for the $\mathrm{C_X}$ curve.

A relevant role in determining the code prediction capabilities, especially in the frame of turbine performances, is played by the applied sub-models. A major improvement in the reliability of the model was given by the flow curvature correction, both in terms of $\mathrm{C_P}$ and wake shape evaluation, confirming its importance for the modelling of small VAWTs. The opposite effect derived instead from the employment of the Glauert one for tip losses; such correction has proved in fact to be redundant, since the ACL own formulation is able to account, at least in terms of average power extraction, for the three-dimensional features of the flow developing around the turbine blades. In such perspective, also the Berg dynamic stall model has demonstrated to be detrimental for the code accuracy, especially for high values of the constant $\mathrm{A_M}$, both in terms of predicted performances and wake shape; dynamic stall models are, therefore, a clear area of future development for the ACL model.

Future developments Apart from the various possible improvements described so far (integration of the shaft and support structures in the ACL model of the turbine, in-depth study of the implemented tip loss and dynamic stall submodels), the natural prosecution of the current work is represented by a comprehensive analysis of the capability of the solver to capture the unsteadiness characterising the turbine operation, especially in the wake. As a matter of fact, only time-mean quantities have been taken into consideration in this thesis. The first step would be to evaluate the intensity of periodic unsteadiness $\mathrm{I_{PER}}$, i.e. related to the motion of the blades, in the wake and compare it to the available experimental data; for the purpose, the simulations should be run for a sufficiently long time for the phase-resolved arithmetic and RMS averages of the velocity data to be performed in a statistically meaningful way, as described in section 2.3. The direct assessment of the streamwise turbulence intensity I_{TU} is instead made difficult by the URANS formulation of the solver, which does not allow to clearly distinguish the unresolved/turbulent velocity fluctuations from the periodic ones. In such perspective, a major improvement would be achieved by switching to a LES turbulence model, whose numerical implementation is strongly eased by the ACL formulation, thanks to the absence of the boundary layer and the high regularity of the computational grid; as a matter of fact, this method suffers from issues in the treatment of near-wall regions and is hard to apply to non-orthogonal, not uniform meshes [58]. LES is able to resolve most of the fluctuations occurring at the larger scales; as a consequence, it would provide a deeper insight into the vortical structures either released by the blades or generated from the disruption of large velocity gradient regions such as shear layers, enriching the description of the wake shed by the turbine.

The study carried out in this thesis, together with the analyses proposed in the previous paragraph, could be then extended to other VAWT architectures, in particular the Troposkien rotor, for which reliable experimental data is available in [4]. Thanks to its three-dimensional formulation, the ACL has the potential to provide a more accurate description of the flow field characterising these machines, for which a two-dimensional modelling is notoriously inadequate, when compared to low-order methods such as DMST; the presence of tip regions however, where the turbine suffers from a very low tip-speed ratio operation [17], represents a considerable obstacle to the implementation of this approach, that for this reason is still in the embryonic stages.

Another characteristic of the ACL tool which has not been investigated in the present work is its capability to handle arbitrarily complex inflow conditions; all simulations were in fact performed considering a uniform, steady flow at the inlet, as the one generated in the low-turbulence test facility used for the experimental campaign (see section 2.2). This aspect is nonetheless of paramount importance, considering the potential advantages of ACL in the simulation of VAWTs in harsh environments such as the urban one, characterised by highly turbulent and in most cases skewed flows, and requires therefore dedicated studies in the near future.

Appendix A

XFoil

A.1 Inviscid formulation

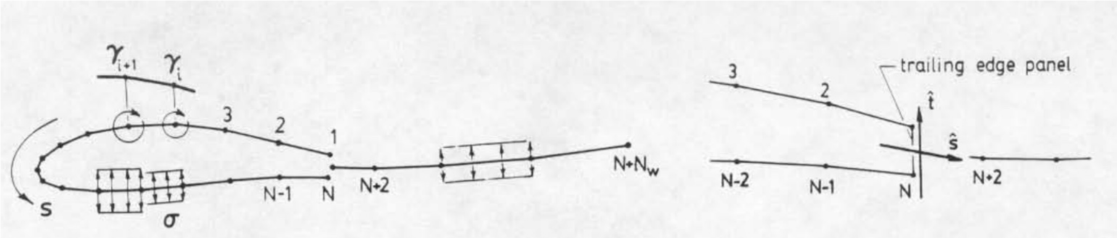

Figure A.1: Schematic of the airfoil and wake panel discretisation. On the right, a detailed view of the trailing edge paneling [20].

In the XFoil code, the freestream region is modelled via a linear vorticity stream function panel method, which relies on the discretisation of the Laplace equation under the hypothesis of irrotational, inviscid and incompressible flow:

$$\nabla^2\psi = 0 \tag{A.1}$$

where ψ(x,y) is a stream function related to the velocity field (u,v) and the velocity potential φ by the following relations:

$$u = \frac{\partial\varphi}{\partial x} = \frac{\partial\psi}{\partial y} \tag{A.2}$$

$$v = \frac{\partial\varphi}{\partial y} = -\frac{\partial\psi}{\partial x} \tag{A.3}$$

Exploiting the linearity of potential formulation, it is possible to express ψ(x,y) as the superposition of elemental flow fields, whose solution is known a priori:

$$\psi(x,y) = (u_\infty y - v_\infty x) + \frac{1}{2\pi}\int \gamma(s)\ln r(s,x,y)ds + \frac{1}{2\pi}\int \sigma(s)\vartheta(s,x,y)ds \tag{A.4}$$

where s is the coordinate along the airfoil profile, r is the magnitude of the vector between point s on the surface and the field one (x,y), ϑ is the vector's angle, and $u_\infty = V_\infty \cos\alpha$ and $v_\infty = V_\infty \sin\alpha$ are the freestream velocity components. From equation A.4, three main components may be distinguished:

- a uniform freestream field, representing the undisturbed flow at given velocity V_∞ and angle of attack α.
- a vortex sheet of strength γ(s) on the airfoil surface, accounting for the bound vorticity generated by lifting interaction.
- a source sheet of strength σ(s) on the airfoil surface and wake, accounting for the interaction between the inviscid and the viscid flow regions. As it will be seen later, this term is exploited for application of proper boundary conditions at the interface of the freestream with the boundary layer.

This operation serves as basis for successive discretisation of the airfoil surface and wake respectively in N and $\mathrm{N_w}$ panels, each one characterized by a linear variation of vortex strength γ between its delimiting nodes [i, i+1]. The result is the following linear system:

$$\sum_{j=1}^{N} a_{ij}\gamma_j - \psi_0 = -u_\infty y_i + v_\infty x_i - \sum_{j=1}^{N+N_w-1} b_{ij}\sigma_j \quad \text{for} \quad 1 \leq \mathrm{i} \leq \mathrm{N} \tag{A.5}$$

Closure of system A.5 derives from the application of the Kutta condition, which imposes no vorticity discontinuity at the airfoil trailing edge, $\gamma_1 + \gamma_\mathrm{N} = 0$. This way, N+1 equations are made available for N+1 unknowns ($\gamma_\mathrm{i}, \psi_0$ for $1 \leq \mathrm{i} \leq \mathrm{N}$). The σ_i coefficients derive instead from the boundary layer equation resolution.

A.2 Viscous formulation

For the viscous region, i.e. the boundary layer and the wake, the standard compressible integral momentum and kinetic energy shape parameters equations are adopted, parametrised on the streamwise coordinate ξ :

$$\frac{d\vartheta}{d\xi} + (2 + H - M_e^2)\frac{\vartheta}{u_e}\frac{du_e}{d\xi} = \frac{C_f}{2} \tag{A.6}$$

$$\vartheta\frac{dH^*}{d\xi} + (2H^{**} + H^*(1-H))\frac{\vartheta}{u_e}\frac{du_e}{d\xi} = 2C_D - H^*\frac{C_f}{2} \tag{A.7}$$

where H= δ^*/ϑ, $\mathrm{H}^* = \vartheta^*/\vartheta$ and $\mathrm{H}^{**} = \delta^{**}/\vartheta$ are respectively the base, kinetic energy and density shape parameters. Governing variables are the integral boundary layer parameters, i.e. the displacement thickness δ^* and the momentum thickness ϑ, together with the boundary layer edge velocity $\mathrm{u_e}$, necessary for the coupling with the outer flow. In order to account for the deviation of the main flow dissipation coefficient $\mathrm{C_D}(\mathrm{C_f}, \mathrm{C}_\tau, \mathrm{H}, \mathrm{H}^*, \mathrm{H_k})$ from the local equilibrium value, a dedicated equation for the maximum shear stress coefficient C_τ is employed:

$$\frac{\delta}{C_\tau}\frac{dC_\tau}{d\xi} = 5.6(C_{\tau_{EQ}}^{0.5} - C_\tau^{0.5}) + 2\delta\left\{\frac{4}{3\delta^*}\left[\frac{C_f}{2} - \left(\frac{H_k - 1}{6.7H_k}\right)^2\right] - \frac{1}{u_e}\frac{du_e}{d\xi}\right\} \tag{A.8}$$

with $\mathrm{H_k}$ kinematic shape parameter. These four variables are discretised with the same strategy adopted for inviscid ones. In laminar regions, equation A.8 is replaced by a one equation model for the growth of amplitude ñ of the most amplified Tollmien-Schichtling wave, so that laminar-to-turbulent transition phenomenon can be embedded in the resolution scheme:

$$\frac{d\tilde{n}}{d\xi} = \frac{d\tilde{n}}{dRe_{\vartheta}}(H_k) \cdot \frac{dRe_{\vartheta}}{d\xi}(H_k, \vartheta) \tag{A.9}$$

where Re_{ϑ} is the momentum thickness Reynolds number. The transition point is identified as the location in which ñ exceeds an user-defined critical value $\tilde{\mathrm{n}}_{\mathrm{crit}}$, that depends on the surface roughness and turbulence intensity levels of the problem.

A.3 Inviscid-viscous coupling

Finally, the two flow domains are coupled via a transpiration model, which enforces flow continuity across the interface through kinematic congruence and the conservation of mass. On one hand, $\mathrm{u_e}$ is related to local vorticity on the airfoil surface and to global vorticity in the wake:

$$u_{e_i} = \pm\gamma_i \quad (1 \leq \mathrm{i} \leq \mathrm{N}) \tag{A.10}$$

$$u_{e_i} = u_{\infty}\hat{n}_y - v_{\infty}\hat{n}_x + \sum_{j=1}^{N} c_{ij}^{\gamma}\gamma_j + \sum_{j=1}^{N+N_w-1} c_{ij}^{\sigma}\sigma_j \quad (\mathrm{N}+1 \leq \mathrm{i} \leq \mathrm{N}+\mathrm{N_w}) \tag{A.11}$$

with $\hat{\mathbf{n}}$ being an unit vector locally normal to the wake. On the other hand, the mass defect m= $\delta^{*}\mathrm{u_e}$ associated to boundary layer is embedded in the outer flow source terms σ_{i}:

$$\sigma_i = \frac{dm}{d\xi} = \pm\frac{m_{i+1} - m_i}{s_{i+1} - s_i} \quad (1 \leq \mathrm{i} \leq \mathrm{N}+\mathrm{N_w}) \tag{A.12}$$

The global system is then resolved simultaneously with a global Newton method. Once ψ(x,y) field is known, velocity and pressure fields can be easily evaluated, leading to the computation of aerodynamic forces. A detailed documentation of the method, including the full derivation of the presented equations, is reported in [19, 20].

Appendix B

Migliore Conformal Mapping

Migliore's conformal mapping method consists in the transformation of a symmetrical airfoil in curved flow to an equivalent cambered airfoil in straight flow, by preserving the local velocities and incidence angles. This procedure allows to successfully embed flow curvature effects in common BEM-based aerodynamic models.

B.1 Blade kinematic analysis

Starting point of the algorithm is the evaluation of the blade kinematic behaviour, i.e the relationship between the blade relative velocity $\mathbf{V}_{\mathrm{R'}}$ chordwise distribution and the turbine geometric and operative characteristics. Following derivation is carried out assuming that the blade chord is orthogonal to the support arm. First step is the computation of the relative velocity module and direction, according to figure B.1:

$$V_{R'} = [(\omega R')^2 + V_\infty^2 - 2V_\infty \omega R' \sin(\vartheta')]^{\frac{1}{2}} \tag{B.1}$$

$$\varphi = \arcsin\left(\frac{V_\infty}{V_{R'}}\cos(\vartheta')\right) \tag{B.2}$$

where ω is the turbine rotational speed and V_∞ is the freestream flow velocity. Accented variables account for local values of the considered quantities:

$$\Delta\vartheta = \arctan\left(\frac{x}{c}\cdot\frac{c}{R}\right) \tag{B.3}$$

$$R' = \frac{R}{\cos(\Delta\vartheta)} \tag{B.4}$$

$$\vartheta' = \vartheta - \Delta\vartheta \tag{B.5}$$

where R is the turbine radius, c the blade chord and ϑ the blade angular position. Introducing the local inverse tip-speed ratio $\varepsilon = V_\infty/(\omega R')$, the final expressions for local relative speed and angle of attack are derived from equations B.1 and B.2:

$$V_{R'}(x/c) = \omega R'[1 + \varepsilon'^2 - 2\varepsilon' \sin(\vartheta')]^{\frac{1}{2}} \tag{B.6}$$

$$\alpha(x/c) = \varphi + \Delta\vartheta = \arctan\left(\frac{\varepsilon' \cos(\vartheta')}{1 - \varepsilon' \sin(\vartheta')}\right) + \Delta\vartheta \tag{B.7}$$

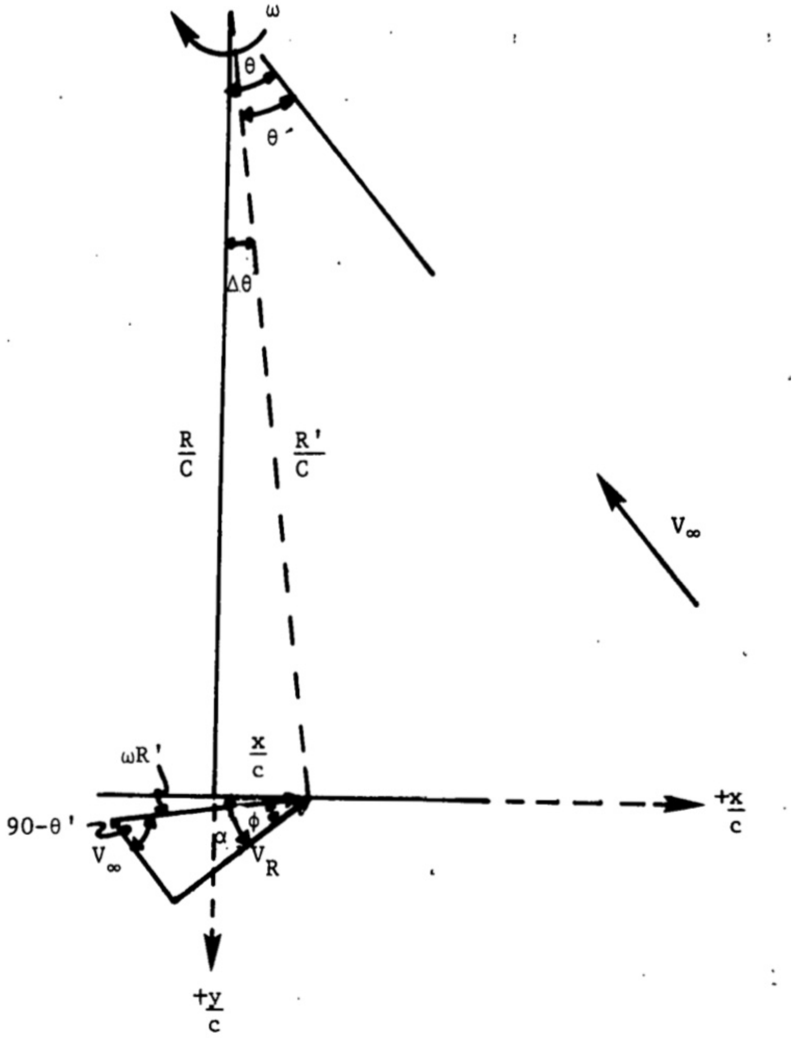

Figure B.1: VAWT geometry for determination of local angle of attack [44].

B.2 Streamline kinematic analysis

The same analysis of section B.1 has to be performed on the flow, so that a mathematical expression for the streamlines interacting with the turbine blades is achieved. Considering a non-inertial (p,q) coordinate system, centred on the blade-support arm attachment point and rotating with the blade itself, the relative inflow velocity can be derived from the vectorial composition of the blade peripheral speed with the freestream velocity:

$$\boldsymbol{V}_{R'} = [\omega(R+q) - V_\infty \sin(\vartheta)] \cdot \hat{\boldsymbol{p}} - [\omega p + V_\infty \cos(\vartheta)] \cdot \hat{\boldsymbol{q}} \tag{B.8}$$

Assuming as initial condition $\psi(0,0)=0$, the corresponding stream function ψ is:

$$\psi = \frac{\omega}{2}p^2 + (V_\infty \cos(\vartheta))p + \frac{\omega}{2}q^2 + [\omega R - V_\infty \sin(\vartheta)]q \tag{B.9}$$

which expressed in terms of $\varepsilon = V_\infty/\omega R$, becomes:

$$\left[\frac{p}{R} + \varepsilon\cos(\vartheta)\right]^2 + \left[\frac{q}{R} + 1 - \varepsilon\sin(\vartheta)\right]^2 = 1 + \varepsilon^2 - 2\varepsilon\sin(\vartheta) + \frac{2\psi}{\omega R^2} \tag{B.10}$$

Equation B.10 represent the mathematical expression for the instantaneous streamlines interacting with the airfoil, which take the form of concentric circles, whose origin and radius are functions of ϑ ad the TSR.

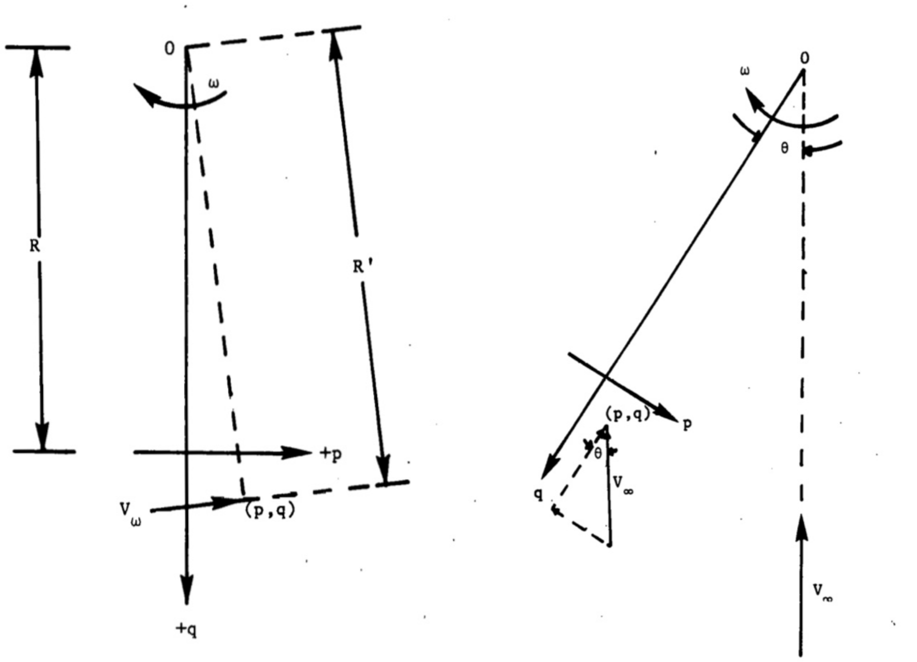

(a) Velocity due to VAWT rotation **(b)** Velocity due to wind

Figure B.2: Wind-blade interaction kinematic analysis [44].

B.3 Virtual airfoil transformation equations

Combining the various equations developed in sections B.1 and B.2, it becomes possible to develop a standard procedure for the conformal mapping of an arbitrary airfoil to its virtual counterpart. Due to the multiple normalisation parameters and frames of reference employed, a specific set of subscripts and superscripts must be defined. More in detail, superscripts g and v identify quantities which are referred to the geometric and virtual coordinate systems, respectively. Subscripts g, v, and R indicate instead quantities which have been made non-dimensional over the geometric chord $\mathrm{c_g}$, the virtual chord $\mathrm{c_v}$, and the turbine radius R.

First step consists in the mapping of the profile coordinates from the standard NACA frame of reference (x,y), centred on the leading edge, to the non-inertial one (p,q) defined in section B.2, centred instead on the blade-support arm attachment point, as shown in figure B.3:

$$p_g^g = (x_g^g - k_g^g)\cos(\alpha_B) + (y_g^g - h_g^g)\sin(\alpha_B) \tag{B.11}$$

$$q_g^g = (x_g^g - k_g^g)\sin(\alpha_B) - (y_g^g - h_g^g)\cos(\alpha_B) \tag{B.12}$$

where $(\mathrm{k_g^g}, \mathrm{h_g^g})$ are the blade-support arm attachment point coordinates, α_B the pitch angle in the NACA frame of reference. Virtual airfoil coordinates in the

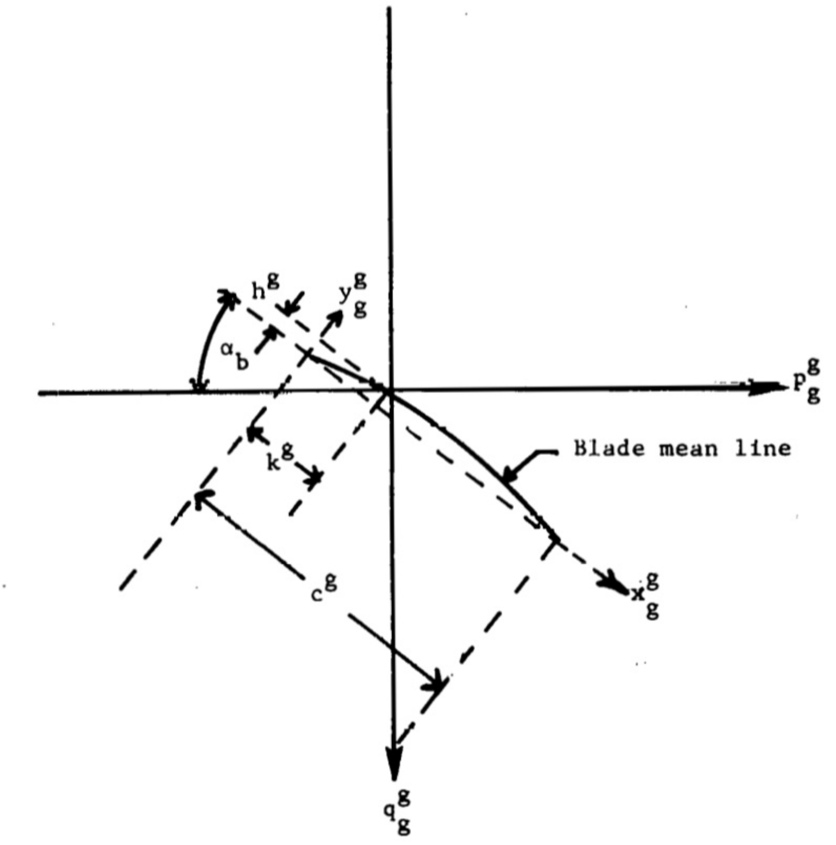

Figure B.3: NACA airfoil coordinate system in relation to blade coordinate system [44].

non-inertial frame of reference (p_v^g, q_g^v) are then evaluated exploiting equation B.10:

$$q_R^v = [(p_R^g + \varepsilon\cos(\vartheta))^2 + (q_R^g + 1 - \varepsilon\sin(\vartheta))^2]^{\frac{1}{2}} \tag{B.13}$$

$$p_R^v = [(p_R^g + \varepsilon\cos(\vartheta))^2 + (q_R^g + 1 - \varepsilon\sin(\vartheta))^2]^{\frac{1}{2}} \cdot \arctan\left[\frac{p_R^g + \varepsilon\cos(\vartheta)}{q_R^g + 1 - \sin(\vartheta)}\right] \tag{B.14}$$

Introducing the following non-dimensional quantities:

$$\gamma = \varepsilon\cos(\vartheta) \tag{B.15}$$

$$\lambda = 1 - \varepsilon\sin(\vartheta) \tag{B.16}$$

$$\Gamma = \frac{p_g^g}{R_g} + \gamma \tag{B.17}$$

$$\Lambda = \frac{q_g^g}{R_g} + \lambda \tag{B.18}$$

equations B.13 and B.14 can be expressed in the form below:

$$\frac{q_g^v}{R_g} = [\Gamma^2 + \Lambda^2]^{\frac{1}{2}} - [\gamma^2 + \lambda^2]^{\frac{1}{2}} \tag{B.19}$$

$$\frac{p_g^v}{R_g} = [\Gamma^2 + \Lambda^2]^{\frac{1}{2}} \cdot \left[\arctan\left(\frac{\Gamma}{\Lambda}\right) - \arctan\left(\frac{\gamma}{\lambda}\right)\right] \tag{B.20}$$

Eventually, virtual airfoil non-inertial coordinates are mapped back to the NACA frame of reference, obtaining the final transformed geometry to be used for aerodynamic analysis. Such process is shown in figure B.4. For the purpose, the virtual angle of attack α_v and virtual chord-to-geometric chord ratio c^v/c^g has to be evaluated from the virtual leading edge (p^v_{g1}, q^v_{g1}) and trailing edge (p^v_{g2}, q^v_{g2}) coordinates:

$$\alpha_v = \arctan\left(\frac{q^v_{g2} - q^v_{g1}}{p^v_{g2} - p^v_{g1}}\right) \tag{B.21}$$

$$\frac{c^v}{c^g} = [(p^v_{g2} - p^v_{g1})^2 + (q^v_{g2} - q^v_{g1})^2]^{\frac{1}{2}} \tag{B.22}$$

and plugged into the transformation equations:

$$x^v_v = [(p^v_g - p^v_{g1})\cos(\alpha_v) + (q^v_g - q^v_{g1})\sin(\alpha_v)] \cdot \frac{c^g}{c^v} \tag{B.23}$$

$$y^v_v = [(p^v_g - p^v_{g1})\sin(\alpha_v) - (q^v_g - q^v_{g1})\cos(\alpha_v)] \cdot \frac{c^g}{c^v} \tag{B.24}$$

A more detailed documentation of the method, including the full derivation of the presented equations, is reported in [44].

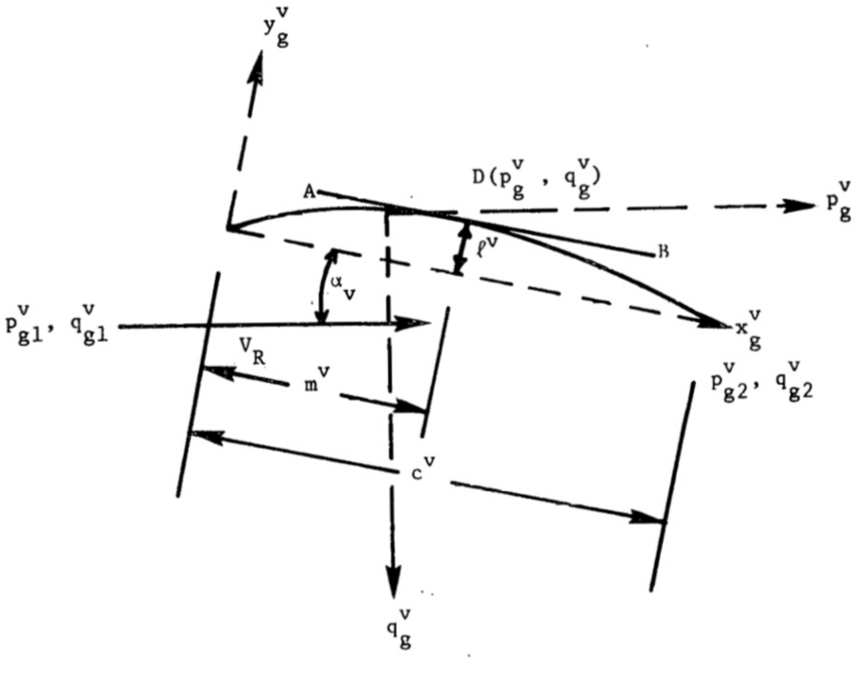

Figure B.4: Transformed mean line [44].

Appendix C

Berg Model

Berg dynamic stall model represents an adaptation to VAWTs of the Gormont formulation, which, being originally developed for helicopters, tends to overestimate unsteady effects in the deep stall region; in such application in fact, the maximum angle of attack is much lower than the one experienced by VAWT blades [37].

C.1 Gormont model

In the model proposed by Gormont, dynamic effects are embedded in the solution by entering the available polar data with a modified angle of attack α_{ref}:

$$\alpha_{ref} = \alpha - K_1 \Delta\alpha \tag{C.1}$$

where α is the static angle of attack, while $\mathrm{K}_1\Delta\alpha$ is a dynamic correction, which depends on various geometric, kinematic and dynamic parameters of the flow:

Hysteresis effects The different behaviour of the airfoil in the detachment and reattachment phases is taken into account by introducing an empirical constant K_1, modifying the dynamic correction term basing on the sign assumed by the angle of attack time derivative $\dot{\alpha}$:

$$K_1 = \begin{cases} 1 & \text{for} \quad \dot{\alpha} \geq 0 \\ -0.5 & \text{for} \quad \dot{\alpha} < 0 \end{cases} \tag{C.2}$$

For $\dot{\alpha} \geq 0$, the dynamic correction reduces the effective angle of attack, delaying separation with respect to the static case. For $\dot{\alpha} < 0$ instead, the effective angle of attack is increased, mimicking the loss in performances experienced by VAWT blades during reattachment; according to empirical evidence, the influence of dynamic stall is lower in this phase than in the detachment one, so that a coefficient of -0.5 is used.

Airfoil geometry Airfoil geometry, in particular its maximum thickness t/c, determines the effects on the dynamic correction of flow unsteadiness, related to the reduced frequency, and compressibility, associated to the Mach number. Sensitivity to the former is quantified by the parameter $\gamma_{\max}$, to the latter by the set of values

M_1, M_2, which, as it will be shown in the next paragraph, are used to build the γ-M characteristic curve. These quantities assume different values basing on the considered aerodynamic coefficient. For lift, they take the form:

$$\gamma^L_{max} = 1.4 + 6(0.06 - t/c) \tag{C.3}$$

$$M^L_1 = 0.4 + 5(0.06 - t/c) \tag{C.4}$$

$$M^L_2 = 0.9 + 2.5(0.06 - t/c) \tag{C.5}$$

while for the drag characteristic curve:

$$\gamma^D_{max} = 1 + 2.5(0.06 - t/c) \tag{C.6}$$

$$M^D_1 = 0.2 \tag{C.7}$$

$$M^D_2 = 0.7 + 2.5(0.06 - t/c) \tag{C.8}$$

As it can be seen from equations C.3 and C.6, sensitivity of the dynamic correction to reduced frequency lowers with increasing t/c, confirming what stated in section 3.1.5. Opposite trend is encountered for compressibility effects, that are amplified going towards the thicker airfoils; given in fact a certain freestream velocity, the maximum local Mach number on the profile increases with the severity of flow acceleration on its leading edge.

Compressibility Compressibility effects are accounted by applying a proper damping function to γ_{max}, that depends on the blade relative Mach number M:

$$\gamma_2 = \gamma_{max} \cdot \max\left\{0, \min\left[1, \frac{M - M_2}{M_1 - M_2}\right]\right\} \tag{C.9}$$

$$\gamma_1 = \begin{cases} \gamma_2/2 & \text{for lift} \\ 0 & \text{for drag} \end{cases} \tag{C.10}$$

According to equation C.9, influence of compressibility on the dynamic stall process is regulated by the parameters M_1, M_2, which depend on t/c. For $M < M_1$, its effect is negligible, so that no damping occurs, while, for $M > M_2$, the damping is so high, that dynamic effects are fully inhibited; for intermediate cases, γ_2 is evaluated as linear interpolation between the two.

Reduced frequency The relationship between $\Delta\alpha$ and the degree of unsteadiness of the flow is treated in a linear way, via the coefficients γ_i(t/c, M):

$$\Delta\alpha = \begin{cases} \gamma_1 S & \text{for} \quad S \leq S_C \\ \gamma_1 S_C + \gamma_2(S - S_C) & \text{for} \quad S > S_C \end{cases} \tag{C.11}$$

where S is an index of unsteady forcing, strictly related to the reduced frequency:

$$S = \sqrt{\left|\frac{c\dot{\alpha}}{2v_r}\right|} \tag{C.12}$$

In order to distinguish the behaviour of thin airfoils from that of thicker ones, the threshold parameter $\mathrm{S_C}$ is defined:

$$S_C = 0.06 + 1.5(0.06 - t/c) \tag{C.13}$$

Eventually, dynamic lift and drag coefficients are evaluated by plugging α_{ref} in the available static tabulated polars. Due to the marked difference in the shape assumed by the lift curve in the attached and separated flow regions, an ad hoc extrapolation procedure is adopted for $\mathrm{C_L^{dyn}}$:

$$\begin{cases} C_L^{dyn} = C_L(\alpha_0) + m(\alpha - \alpha_0) \\ C_D^{dyn} = C_D(\alpha_{ref}) \end{cases} \tag{C.14}$$

where the slope m is determined from the following equation:

$$\mathrm{m} = \min\left[\frac{C_L(\alpha_{ref}) - C_L(\alpha_0)}{\alpha_{ref} - \alpha_0}, \frac{C_L(\alpha_{SS}) - C_L(\alpha_0)}{\alpha_{SS} - \alpha_0}\right] \tag{C.15}$$

where α_{SS} is the static stall angle, while α_0 the zero-lift one. According to this strategy, the original curve slope is preserved in the attached flow region, introducing no relevant deviations from the airfoil static behaviour, while in the separated flow one, pointwise slope evaluation allows to successfully embed the stall delay phenomenon into the computation of the lift coefficient; as suggested by Berg [6], the performance of such extrapolation method can be improved by redefining α_{SS} as the point in which the lift curve starts departing from linear behaviour.

C.2 Berg modification

Massé [37] and Berg [6] proposed to modify the Gormont model by computing the dynamic lift and drag coefficients as linear interpolation between the static and the Gormont ones:

$$C_L^{mod} = \begin{cases} C_L + \left[\frac{A_M\alpha_{SS} - \alpha}{A_M\alpha_{SS} - \alpha_{SS}}\right](C_L^{dyn} - C_L) & \text{for} \quad \alpha \leq A_M\alpha_{SS} \\ C_L & \text{for} \quad \alpha > A_M\alpha_{SS} \end{cases} \tag{C.16}$$

$$C_D^{mod} = \begin{cases} C_D + \left[\frac{A_M\alpha_{SS} - \alpha}{A_M\alpha_{SS} - \alpha_{SS}}\right](C_D^{dyn} - C_D) & \text{for} \quad \alpha \leq A_M\alpha_{SS} \\ C_D & \text{for} \quad \alpha > A_M\alpha_{SS} \end{cases} \tag{C.17}$$

where $\mathrm{A_M}$ is a semi-empirical constant, to be tuned for the specific case under analysis. Further details can be found in [46].

Nomenclature

Acronyms

ACL	Actuator Line Method
AOA	Angle of Attack
ASSM	Actuator Swept-Surface Method
BAWT	Building-Augmented Wind Turbine
BEM	Blade Element Method
BPP	Blade Passing Period
CFD	Computational Fluid Dynamics
DMST	Double Multiple Stream Tube
DNS	Direct Numerical Simulation
EVM	Effective Velocity Method
FV	Finite Volume
HAWT	Horizontal Axis Wind Turbine
LE	Leading Edge
LES	Large Eddy Simulation
LLT	Lifting Line Theory
NS	Navier-Stokes
OpenFOAM	Open Field Operation And Manipulation
PM	Panel Method
RMS	Root Mean Square
SST	Shear Stress Transport
SWT	Small Wind Turbine

TE	Trailing Edge
TSR	Tip Speed Ratio
URANS	Unsteady Reynolds-Averaged Navier-Stokes
VAWT	Vertical Axis Wind Turbine

Subscripts

f	quantity evaluated at the centroid of considered face
0	freestream flow quantity
N	quantity evaluated at the centroid of a neighbouring cell
n	normal component (blade frame of reference)
o	quantity evaluated at the previous timestep
P	quantity evaluated at the centroid of considered cell
t	tangential component (blade frame of reference)

Symbols

α	angle of attack [deg]
α_{SS}	static stall angle of attack [deg]
β	blade pitch angle [deg]
$\boldsymbol{\omega}$	vorticity vector [1/s]
Δt	timestep [s]
Γ	circulation [m^2/s]
μ	dynamic viscosity [kg/(m·s)]
μ_{T}	eddie viscosity [kg/(m·s)]
ν	kinematic viscosity [m^2/s]
ν_{T}	kinematic eddie viscosity [m^2/s]
Ω	turbine rotational speed [rad/s]
ω	turbulent frequency [1/s]
ω_{s}	streamwise vorticity [1/s]
φ	generic flow quantity, blade relative flow angle [deg]

ρ	flow density [kg/m^3]
σ	rotor solidity [-]
τ	turbine revolution period [s]
ϑ	blade angular position [deg]
$\mathbf{D}$	drag force vector [N]
$\mathbf{L}$	lift force vector [N]
$\mathbf{n}$	unit vector normal to the blade peripheral speed [-]
$\mathbf{t}$	unit vector tangential to the blade peripheral speed [-]
$\mathbf{U}_0$	freestream flow velocity [m/s]
$\mathbf{U}$	local flow velocity [m/s]
$\mathbf{u}$	fluctuating velocity vector [m/s]
$\mathbf{v_l}$	local undisturbed flow velocity [m/s]
$\mathbf{v_r}$	blade relative flow velocity [m/s]
$\mathbf{v_{tr}}$	blade peripheral speed/translational velocity [m/s]
A	turbine front section area [m^2]
$\mathrm{A_M}$	Berg model constant [-]
c	blade chord [m]
$\mathrm{C_D}$	drag coefficient [-]
$\mathrm{C_L}$	lift coefficient [-]
$\mathrm{C_P}$	turbine average power coefficient [-]
$\mathrm{C_T}$	blade torque coefficient [-]
$\mathrm{C_X}$	turbine average streamwise thrust coefficient [-]
Co	Courant number (cell-based) [-]
D	turbine diameter [m]
$\mathrm{F_X}$	streamwise rotor thrust [N]
H	blade half height [m]
$\mathrm{h_{cell}}$	grid cell characteristic dimension [m]
I	turbulence intensity [-]

I_{PER}	periodic unsteadiness intensity [-]
I_{TU}	streamwise turbulence intensity [-]
k	turbulent kinetic energy [m^2/s^2]
M	blade relative Mach number [-]
N_b	turbine number of blades [-]
P	absolute pressure [Pa]
R	turbine radius [m]
Re	blade Reynolds number [-]
T	rotor torque [Nm]
t	time [s]
X	transversal coordinate [m]
x	profile chordwise coordinate [m]
Y	streamwise coordinate [m]
Z	spanwise coordinate [m]
z_0	roughness length [m]

Bibliography

[1] G. Baldassarra. “Multi-dimensional CFD Simulation of a H-type Darrieus Vertical-Axis Wind Turbine with OpenFOAM”. MA thesis. Politecnico di Milano, 2015 (cit. on p. 21).

[2] L. Battisti. *Gli impianti motori eolici*. Lorenzo Battisti Editore, 2012 (cit. on pp. 10–12, 14, 42, 52, 53, 78).

[3] L. Battisti et al. “Aerodynamic Measurements on a Vertical Axis Wind Turbine in a Large Scale Wind Tunnel”. In: *Journal of Energy Resources Technology* 133.3 (Sept. 2011), pp. 031201-1-9 (cit. on pp. 53, 66, 70, 71).

[4] L. Battisti et al. “Experimental benchmark data for H-shaped and troposkien VAWT architectures”. In: *Renewable Energy* 125 (2018), pp. 425–444 (cit. on pp. 24–26, 86).

[5] C. Beller. *Urban Wind Energy - State of the Art 2009*. Tech. rep. Danmarks Tekniske Universitet, RisøNationallaboratoriet for Baeredygtig Energi, 2009 (cit. on pp. 4, 5, 8).

[6] D.E. Berg. “An Improved Double-Multiple Streamtube Model for the Darrieus-Type Vertical Axis Wind Turbine”. In: *Sixth Biennal Wind Energy Conference and Workshop*. 1983, pp. 231–233 (cit. on pp. xviii, 50, 52, 99).

[7] L. Bernini and M. Caccialanza. “Development of the Effective Velocity Model for wind turbines aerodynamics numerical simulation through an Actuator Line approach”. MA thesis. Politecnico di Milano, July 2014 (cit. on pp. xvii, 33, 34, 36).

[8] A. Bianchini et al. “A critical analysis on low-order simulation models for darrieus vawts: how much do they pertain to the real flow?” In: *Proceedings of ASME Turbo Expo 2018: Turbomachinery Technical Conference and Exposition*. Oslo, Norway, June 2018 (cit. on p. 14).

[9] A. Bianchini et al. “An Experimental and Numerical Assessment of Airfoil Polars for Use in Darrieus Wind Turbines - Part I: Flow Curvature Effects”. In: *Journal of Engineering for Gas Turbines and Power* 138.3 (Mar. 2016), pp. 032602-1-10 (cit. on p. 46).

[10] A. Bianchini et al. “An Experimental and Numerical Assessment of Airfoil Polars for Use in Darrieus Wind Turbines - Part II: Post-stall Data Extrapolation Methods”. In: *Journal of Engineering for Gas Turbines and Power* 138.3 (Mar. 2016), pp. 032603-1-10 (cit. on p. 38).

[11] A. Bianchini et al. “Critical Analysis Of Dynamic Stall Models In Low-Order Simulation Models For Vertical-Axis Wind Turbines”. In: *71st Conference of the Italian Thermal Machines Engineering Association*. Turin, Italy, Sept. 2016 (cit. on pp. 50, 52).

[12] A. Bianchini et al. “Detailed analysis of the wake structure of a straight-blade H-Darrieus wind turbine by means of wind tunnel experiments and CFD simulations”. In: *Journal of Engineering for Gas Turbines and Power* 140.3 (2017), pp. 032604-032604-9 (cit. on p. 78).

[13] A. Bianchini et al. “Virtual incidence effect on rotating airfoils in Darrieus wind turbines”. In: *Energy conversion and management* 111 (2016), pp. 329–338 (cit. on p. 46).

[14] M. Caglioni. “Actuator Line method based on the Effective Velocity Model for CFD simulations of Vertical-Axis Wind Turbines”. MA thesis. Politecnico di Milano, Apr. 2015 (cit. on pp. xvii, 31, 32, 34, 35).

[15] T. Cebeci, G.J. Mosinskis, and A.M.O. Smith. “Calculation of Separation Points in Incompressible Turbulent Flows”. In: *Journal of Aircraft* 9.9 (1972), pp. 618–624 (cit. on p. 41).

[16] A. G. Davenport et al. “Estimating the roughness of cities and sheltered country”. In: *12th Conference on Applied Climatology*. Asheville, NC, 2000, pp. 96–99 (cit. on p. 6).

[17] V. Dossena et al. “An Experimental Study of the Aerodynamics and Performance of a Vertical Axis Wind Turbine in a Confined and Unconfined Environment”. In: *Journal of Energy Resources Technology* 137.5 (2015), pp. 051207-1-12 (cit. on pp. xvii, 24–26, 57, 59, 66, 68, 86).

[18] M. Douak and Z. Aouachria. “Starting Torque Study of Darrieus Wind Turbine”. In: *International Journal of Physical and Mathematical Sciences* 9.8 (2015), pp. 476–481 (cit. on p. 9).

[19] M. Drela. “Viscous-Inviscid Analysis of Transonic and Low Reynolds Number Airfoils”. In: *AIAA Journal* 25.10 (Oct. 1987), pp. 1347–1355 (cit. on pp. 39, 89).

[20] M. Drela. “XFOIL: An Analysis and Design System for Low Reynolds Number Airfoils”. In: *Conference on Low Reynolds Number Airfoil Aerodynamics*. University of Notre Dame, June 1989 (cit. on pp. 39, 87, 89).

[21] E. Dyachuk and A. Goude. “Simulating Dynamic Stall Effects for Vertical Axis Wind Turbines Applying a Double Multiple Streamtube Model”. In: *Energies* 8 (2015), pp. 1353–1372 (cit. on p. 51).

[22] M. Ferlini. “CFD model of a vertical-axis wind turbine in open-jet wind-tunnel”. MA thesis. Politecnico di Milano, Apr. 2017 (cit. on pp. xviii, 53, 57, 59, 62).

[23] R. E. Gormont. *A mathematical model of unsteady aerodynamics and radial flow for application to helicopter rotors*. Tech. rep. USAAMRDL 72-67. Fort Eustis, Virginia: U.S. Army Air Mobility Research and Development Laboratory, 1973 (cit. on p. 51).

[24] C.S.B. Grimmond and T.R. Oke. “Aerodynamic properties of urban areas derived from analysis of surface form”. In: *Journal of Applied Meteorology* 38 (1999), pp. 1262–1292 (cit. on p. 4).

[25] P. Igot and C.S. d’Attenhoven. “Design and test of a 3D-printed horizontal axis wind turbine”. MA thesis. École polytechnique de Louvain, 2016 (cit. on p. 8).

[26] R.I. Issa. “Solution of the implicitly discretised fluid flow equations by operator-splitting”. In: *Journal of Computational Physics* 62.1 (1986), pp. 40–65 (cit. on pp. xvii, 37).

[27] P.A. James et al. “Implications of the UK field trial of building mounted horizontal axis micro-wind turbines”. In: *Energy Policy* 38 (2010), pp. 6130–6144 (cit. on p. 2).

[28] H. Jasak. “Error Analysis and Estimation for the Finite Volume Method with Applications to Fluid Flows”. PhD thesis. Imperial College, June 1996 (cit. on pp. 18, 20, 37).

[29] A.N Kolmogorov. “The local structure of turbulence in incompressible viscous fluid for very large Reynolds numbers”. In: *Dokl. Akad. Nauk.* 30 (1941), pp. 301–305 (cit. on p. 55).

[30] P.K. Kundu, I.M. Cohen, and D.D. Dowling. *Fluid Mechanics*. Fifth Edition. Elsevier, 2012 (cit. on p. 53).

[31] B.E. Launder and B.I. Sharma. “Application of the Energy Dissipation Model of Turbulence to the Calculation of Flow Near a Spinning Disc”. In: *Letters in Heat and Mass Transfer* 1.2 (1974), pp. 131–138 (cit. on p. 56).

[32] J.G. Leishman. “Challenges in Modeling the Unsteady Aerodynamics of Wind Turbines”. In: *21st ASME Wind Energy Symposium and the 40th AIAA Aerospace Sciences Meeting*. Reno, NV, Jan. 2002 (cit. on pp. 48, 49).

[33] C. Lindeburg. *Investigation into rotor blade aerodynamics. analysis of the stationary measurements on the uae phase-vi rotor in the nasa-ames wind tunnel 3*. Tech. rep. ECN-C-03-025. Energy Research Center of the Netherlands, 2003 (cit. on p. 42).

[34] D. Marten et al. “Effects of Airfoil’s Polar Data in the Stall Region on the Estimation of Darrieus Wind Turbine Performance”. In: *Journal of Engineering for Gas Turbines and Power* 139.2 (Feb. 2017), pp. 022606-1-9 (cit. on p. 40).

[35] D. Marten et al. “Nonlinear Lifting Line Theory Applied To Vertical Axis Wind Turbines: Development of a Practical Design Tool”. In: *ISROMAC 2016*. Honolulu. Hawaii, Apr. 2016 (cit. on p. 15).

[36] J. Martin. *Distributed vs. centralized electricity generation: are we witnessing a change of paradigm? An introduction to distributed generation*. URL: `http://www.vernimmen.net/ftp/An_introduction_to_distributed_generation.pdf` (cit. on pp. 1, 2).

[37] B. Massé. *Description de deux programmes d'ordinateur pour le calcul des performances et des charges aérodynamiques pour les éoliennes à axe vertical.* Tech. rep. IREQ-2379. Institut de Recherche de l'Hydro-Québec, 1981 (cit. on pp. xviii, 50, 52, 97, 99).

[38] C. Masson, C. Leclerc, and I. Paraschivoiu. "Appropriate Dynamic-Stall Models for Performance Predictions of VAWTs with NLF Blades". In: *International Journal of Rotating Machinery* 4.2 (1998), pp. 129–139 (cit. on p. 50).

[39] W.J. McCroskey. *The Phenomenon of Dynamic Stall.* Tech. rep. 81264. Ames Research Center, Moffett Field, California: NASA, Mar. 1981 (cit. on pp. 48, 49).

[40] F.R. Menter. "Two-Equation Eddy-Viscosity Turbulence Models for Engineering Applications". In: *AIAA Journal* 32.8 (1994), pp. 1598–1605 (cit. on p. 56).

[41] E. Mercker and J. Wiedemann. *On the Correction of Interference Effects in Open Jet Wind Tunnels.* Tech. rep. 960671. SAE, 1996 (cit. on p. 26).

[42] S. Mertens. *Wind Energy in the Built Environment: Concentrator Effects of Buildings.* 2006 (cit. on pp. 7, 10, 11).

[43] S. Mertens, G. van Kuik, and G. van Bussel. "Performance of an H-Darrieus in the Skewed Flow on a Roof". In: *Journal of Solar Energy Engineering* 125 (2003), pp. 433–440 (cit. on pp. 4, 5, 10).

[44] P.G. Migliore and W.P. Wolfe. *The effects of flow curvature on the aerodynamics of Darrieus wind turbines.* Tech. rep. ORO-5135-77/7. U.S. Department of Energy, July 1980 (cit. on pp. xviii, 43–45, 92–95).

[45] *OpenFOAM v5 User Guide: Numerical schemes.* URL: `https://cfd.direct/openfoam/user-guide/fvschemes/` (cit. on p. 63).

[46] I. Paraschivoiu. *Wind Turbine Design: With Emphasis on Darrieus Concept.* Polytechnic International Press, 2002 (cit. on p. 99).

[47] I. Paraschivoiu and F. Delclaux. "Double Multiple Streamtube Model with Recent Improvements". In: *Journal of Energy* 7.3 (1983), pp. 250–255 (cit. on p. 13).

[48] G. Persico et al. "Time-Resolved Experimental Characterization of the Wakes Shed by H-Shaped and Troposkien Vertical Axis Wind Turbines". In: *Journal of Energy Resources Technology* 139 (2017), pp. 031203-1-11 (cit. on pp. 12, 26, 28).

[49] P. Schito. "Large eddy simulation of wind turbines: interaction with turbulent flow". PhD thesis. Politecnico di Milano, Mar. 2012 (cit. on pp. xvii, 34).

[50] P. Schito and A. Zasso. "Actuator forces in CFD: RANS and LES modeling in OpenFOAM". In: *The Science of Making Torque from Wind 2014 (TORQUE 2014).* 2014 (cit. on p. xvii).

[51] S. Shamsoddin and F. Porté Agel. "Large Eddy Simulation of Vertical Axis Wind Turbine Wakes". In: *Energies* 7.2 (2014), pp. 890–912 (cit. on pp. xvii, 20, 21, 29, 30).

[52] R.E. Sheldahl and P.C. Klimas. *Aerodynamics characteristics of seven symmetrical airfoil sections through 180-degree angle of attack for use in aerodynamic analysis of vertical axis wind turbines*. Tech. rep. SAND80 2114. Albuquerque, New Mexico: Sandia National Laboratories, Mar. 1981 (cit. on pp. 38, 43).

[53] J.N. Sørensen and W.Z. Shen. “Numerical modelling of wind turbine wakes”. In: *Journal of Fluids Engineering* 124.2 (2002), pp. 393–399 (cit. on pp. 29, 36).

[54] K. Sunderland. “Micro (Wind) Generation: ’Urban Resource Potential & Impact on Distribution Network Power Quality’”. PhD thesis. Dublin Institute of Technology, 2014 (cit. on pp. 2, 3, 5, 6).

[55] P. Sweby. “High resolution schemes using flux limiters for hyperbolic conservation laws”. In: *SIAM Journal on Numerical Analysis* (1984) (cit. on p. 63).

[56] W.A. Timmer. “Aerodynamic characteristics of wind turbine blade airfoils at high angles-of-attack”. In: *TORQUE 2010 - The Science of Making Torque from Wind*. Crete, Greece, June 2010, p. 71 (cit. on p. 42).

[57] J. Tu, G. Yeoh, and C. Liu. *Computational Fluid Dynamics: a Practical Approach*. Butterworth-Heinemann, 2012 (cit. on p. 63).

[58] E. de Villiers. “The Potential of Large Eddy Simulation for the Modeling of Wall Bounded Flows”. PhD thesis. Imperial College, 2006 (cit. on pp. 29, 55, 57, 86).

[59] L.A. Viterna and R.D. Corrigan. *Fixed Pitch Rotor Performance of Large Horizontal Axis Wind Turbines*. Tech. rep. CP-2230. USA: NASA, 1981 (cit. on p. 40).

[60] D.C. Wilcox. “Re-assessment of the scale-determining equation for advanced turbulence models”. In: *AIAA Journal* 26.11 (1988), pp. 1299–1310 (cit. on p. 56).

[61] WWEA. *Small wind world report*. 2017 (cit. on pp. 2, 3, 7).